Optimisation of a Spherical Helical Antenna

John Leonard Winkle

Thesis submitted to the University of Sheffield for the degree of Doctor of Philosophy in the Faculty of Engineering

Department of Electronic and Electrical Engineering
University of Sheffield
Mappin Street, Sheffield S1 3JD, UK

October 2007

Summary

Cylindrical helix and planar spiral antennas produce circularly polarised (CP) radiation over a wide bandwidth. Unfortunately this circular polarisation is not maintained in off-axis directions. This research investigates the Spherical Helical Antenna (SHA) which is essentially a helix which has been tapered to give it a spherical envelope. The SHA is shown to produce good quality CP over both a wide bandwidth and a wide beamwidth.

Custom FORTRAN code has been written which implements the Method of Moments (MoM) technique in order to model the antenna. Curved segments are used and these are shown to substantially reduce the number of segments required to accurately represent the current distribution and shape of the antenna. The code is carefully validated against both published results and control software.

Modifications are proposed to the SHA including a novel scheme to define the spacing between turns, the consideration of non-integer number of turns, truncation, and a novel balanced feed configuration. Each of these modifications is shown to improve the performance of the antenna, particularly its polarisation properties.

A multi-objective non-dominated genetic algorithm (GA) is applied to optimise the performance of the antenna in terms of its axial ratio (AR) in the boresight direction and its half-power and AR beamwidths.

With the aid of a purpose-milled mould which allowed wires to be shaped to exact curvatures, a prototype twin-arm SHA has been constructed. Radiation patterns and axial ratio measurements for this antenna are presented.

Acknowledgements

I wish to express my gratitude to the numerous individuals who have helped me in various ways throughout this research. In particular I would like to thank **Dr Rob Edwards** for helping formulate the project and for introducing me to the Method of Moments. Thanks also to **Professor Barry Chambers** for his advice and constructive criticism which has helped me to write this thesis.

I am also grateful to **Ian Lyne** for his help with the construction of the mould, **Dianne Webster** for her expert soldering, and to **Dr Jon Rigelsford** and **Patrick McEvoy** for their assistance with measurements.

Finally I would like to thank my **family and friends** for their support and encouragement during this work. Without their support this thesis would not have been possible. Last but not least I would like sincerely to thank **Katy** for her patience.

Publications

J. Winkle, R. M. Edwards, B. Chambers, B. McConnell, and E. Bryant, "Design, Fabrication and Measurement of an Encapsulated Inverted-F Dual Band Antenna for the Gathering of Data on Seals at Sea using SMS over a GSM System.", Twelfth International Conference on Antennas and Propagation, 2003. ICAP 2003. (Conf. Publ. No. 491), vol. 2, pp. 739-742

Contents

1 Introduction 1-1
1.1 Purpose of research 1-1
1.2 Review of relevant research 1-2
1.2.1 The cylindrical helix antenna 1-2
1.2.2 Modifications to the helix antenna 1-3
1.2.3 The spiral antenna 1-4
1.2.4 The Spherical Helical Antenna (SHA) 1-4
1.2.5 Antenna optimisation 1-8
1.3 Computer modelling 1-10
1.4 SHA geometry 1-12
1.4.1 Mathematical description 1-15
1.5 Novel contributions 1-16
1.6 Overview of thesis 1-18

2 Method of Moments 2-1
2.1 Introduction 2-1
2.2 Applying the Method of Moments 2-1
2.3 Source models 2-2
2.4 Curved segments 2-3
2.5 Derivation of impedance matrix equation 2-4
2.6 Discussion 2-10

3 Software and Validation 3-1
3.1 Introduction 3-1
3.2 SHA-MoM code 3-2
3.2.1 Program operation 3-2
3.2.2 Input parameters 3-3
3.3 Validation with published results 3-6
3.4 Validation with NEC 3-11
3.5 Convergence 3-14
3.6 Discussion 3-19

4 Modelling 4-1
4.1 Introduction 4-1
4.2 Spacing between turns 4-2
4.3 Non-integer number of turns 4-12
4.4 Twin-arm geometry with CCS 4-14
4.5 Cylindrical helix 4-21
4.6 Discussion 4-25

5 Optimisation 5-1
5.1 Introduction 5-1
5.2 Mean axial ratio beamwidth 5-3
5.3 Dual-objective optimisation (integer N) 5-6
5.4 Dual-objective optimisation (non-integer N) 5-10
5.5 Quad-objective optimisation 5-13
5.6 Combined-objective optimisation 5-19
5.7 Review of mean axial ratio beamwidth methodology 5-25
5.8 Discussion 5-28

6 Measurements 6-1
6.1 Introduction 6-1
6.2 Construction 6-1
6.3 Non-optimal prototype 6-2
6.4 Addition of ground plane 6-3
6.5 Optimal prototype (Antenna No. 197) 6-7
6.6 Discussion 6-10

7 Conclusions 7-1
7.1 Introduction 7-1
7.2 Summary of research 7-1
7.3 Further work 7-6

Appendices

Expressions defining the SHA geometries .... Appendix A

Expressions for far-field patterns .... Appendix B

The NSGA-II genetic algorithm .... Appendix C

List of figures

Figure 1.1 – Centre-fed hemispherical helical antenna reproduced from Chan et al. [12] 1-7

Figure 1.2 – SHA viewed from the side 1-13

Figure 1.3 – SHA viewed from above (for clarity, only the upper hemisphere is shown) 1-13

Figure 1.4 – Centre-fed Spherical Helical Antenna 1-14

Figure 2.1 – Geometry and variables used in impedance matrix equation 2-4

Figure 3.1 – Example of a parameters.csv file 3-4

Figure 3.2 – Geometry of a simple Spherical Helical Antenna 3-6

Figure 3.3 – Comparison of current magnitude and phase progression with published results 3-7

Figure 3.4 – Current magnitude and phase progression and overlay plotted against ϕ instead of ℓ 3-8

Figure 3.5 – Current magnitude along wire of 7-turn SHA, modelled with NEC and SHA-MoM 3-9

Figure 3.6 – Comparison of impedance characteristics 3-10

Figure 3.7 – Centre-fed Spherical Helical Antenna 3-11

Figure 3.8 – Input resistance for a 7-turn centre-fed SHA of radius 1.95cm in free-space 3-12

Figure 3.9 – Input reactance for a 7-turn centre-fed SHA of radius 1.95cm in free-space 3-12

Figure 3.10 – Input resistance against frequency for a 7-turn centre-fed SHA of radius 1.95cm situated 0.4cm above an infinite ground-plane 3-13

Figure 3.11 – Input reactance against frequency for a 7-turn centre-fed SHA of radius 1.95cm situated 0.4cm above an infinite ground-plane 3-13

Figure 3.12 – Convergence of NEC (linear segments) 3-14

Figure 3.13 – Convergence of SHA-MoM code (curved segments) 3-15

Figure 3.14 – Shape of current pulses as determined by the segment length 3-17

Figure 3.15 – Three overlapping current pulses shown for two different segment lengths 3-18

Figure 4.1 – 10-turn SHAs viewed from the side 4-2

Figure 4.2 – 10-turn SHAs viewed from above (for clarity, only the upper hemisphere is shown) 4-2

Figure 4.3 – Axial ratio on boresight for 3-turn CVS and CCS geometries 4-3

Figure 4.4 – Axial ratio beamwidth for 3-turn CVS and CCS geometries 4-4

Figure 4.5 – Axial ratio on boresight for 7-turn CVS and CCS geometries 4-5

Figure 4.6 – Axial ratio in the $\phi = 0°$ elevation plane for 7-turn CVS and CCS geometries 4-6

Figure 4.7 – Radiation pattern for a 7-turn CVS SHA with C=1.31λ, $\phi = 0°$, -180° $< \theta <$ 180° 4-8

Figure 4.8 – Phase difference between E_θ and E_ϕ for a 7-turn CVS SHA with C=1.31λ, $\phi = 0°$ 4-8

Figure 4.9 – Radiation pattern for a 7-turn CCS SHA with C=1.43λ, $\phi = 0°$, -180° $< \theta <$ 180° 4-9

Figure 4.10 – Phase difference between E_θ and E_ϕ for a 7-turn CCS SHA with C=1.43λ, $\phi = 0°$ 4-9

Figure 4.11 – Impedance characteristics of 3-turn CVS and CCS geometries 4-10

Figure 4.12 – Impedance characteristics of 7-turn CVS and CCS geometries 4-10

Figure 4.13 – SHA geometries with varying, non-integer, numbers of turns 4-12

Figure 4.14 – Axial ratio in boresight direction for CVS SHA with C=1.125λ 4-13

Figure 4.15 – Centre-fed Spherical Helical Antenna 4-14

Figure 4.16 – Axial ratio on boresight for 3-turn twin-arm and conventional SHA geometries 4-16

Figure 4.17 – Gain on boresight for 3-turn twin-arm and conventional SHA geometries 4-17

Figure 4.18 – Half-power beamwidth for 3-turn twin-arm and conventional SHA geometries 4-18

Figure 4.19 – Radiation pattern for 3-turn twin-arm SHA, $\phi = 0°$, C/λ=1.6 4-19

Figure 4.20 – Axial ratio for 3-turn twin-arm SHA with C=1.6λ, $\phi = 0°$ 4-20

Figure 4.21 – Axial ratio on boresight of 6-turn cylindrical helix with 14° pitch angle, λ/10 above an infinite ground plane 4-21

Figure 4.22 – Gain on boresight of 6-turn cylindrical helix with 14° pitch angle, λ/10 above an infinite ground plane 4-22

Figure 4.23 – HPBW and 3dB AR BW of 6-turn cylindrical helix with 14° pitch angle, λ/10 above an infinite ground plane 4-23

Figure 4.24 – Impedance characteristics of 6-turn cylindrical helix with 14° pitch angle, λ/10 above an infinite ground plane 4-24

Figure 5.1 – Radiation hemisphere of a 3-turn CCS type SHA above a ground plane, C=1.1λ 5-4

Figure 5.2 – Radiation hemisphere of a 3-turn CCS type SHA above a ground plane, C=1.2λ 5-4

Figure 5.3 – Solution space of initial population 5-7

Figure 5.4 – Solution space of final generation 5-8

Figure 5.5 – Half-power beamwidth vs. mean AR beamwidth for best antennas 5-16

Figure 5.6 – Radiation hemisphere for antenna No. 800 5-17
Figure 5.7 – Radiation hemisphere for antenna No. 197 5-18
Figure 5.8 – Radiation hemisphere for antenna No. 2656 5-22
Figure 5.9 – Radiation hemisphere for antenna No. 3507, C=1.38λ 5-24
Figure 5.10 – Beamwidth variation with frequency for antenna No. 3507 5-24
Figure 5.11 – Comparison between 16-cuts and 8-cut mean AR beamwith values 5-26
Figure 5.12 – Comparison between 16-cuts and 4-cut mean AR beamwidth values ... 5-26
Figure 5.13 – Comparison between 16-cuts and 2-cut mean AR beamwidth values ... 5-27
Figure 5.14 – Comparison between 16-cut mean AR beamwidth and AR beamwidth in one plane 5-27
Figure 6.1 – Photograph of one of the two moulds 6-2
Figure 6.2 – Photograph of prototype SHA in anechoic chamber 6-2
Figure 6.3 – Layout of printed balun 6-4
Figure 6.4 – Photograph of prototype SHA mounted 5mm above a ground plane 6-4
Figure 6.5 – Axial ratio on boresight over a range of frequencies 6-6
Figure 6.6 – 3dB Axial ratio Beamwidth over a range of frequencies 6-6
Figure 6.7 – Prototype of Antenna No. 197 in anechoic chamber 6-7
Figure 6.8 – Radiation pattern of Antenna No. 197 modelled with SHA-MoM (1.8GHz, $\phi = 0°$) 6-8
Figure 6.9 – Measured radiation pattern of Antenna No. 197 prototype (1.8GHz, $\phi = 0°$) 6-8
Figure 6.10 – Comparison of measured and modelled axial ratio characteristics of Antenna No. 197 (1.8GHz, $\phi = 0°$) 6-9

List of tables

Table 3.1 – List of parameters for setting the geometry of the antenna to be modelled 3-4

Table 3.2 – Additional parameter to allow multiple models to be analysed 3-4

Table 3.3 – List of parameters for controlling the output data produced by the program 3-5

Table 5.1 – Parameter ranges for dual-objective optimisation 5-6

Table 5.2 – Objectives for dual-objective optimisation 5-6

Table 5.3 – Best solutions for dual-objective optimisation 5-9

Table 5.4 – Parameter ranges for dual-objective optimisation 5-10

Table 5.5 – Objectives for dual-objective optimisation 5-10

Table 5.6 – Best 25 solutions for dual-objective optimisation 5-11

Table 5.7 – Beamwidths of solutions 2 through 10 of Table 5.6 5-12

Table 5.8 – Objectives for quad-objective optimisation 5-13

Table 5.9 – Parameter ranges for quad-objective optimisation 5-13

Table 5.10 – Solutions from quad-objective GA with less than 3dB axial ratio on boresight 5-15

Table 5.11 – Parameters for antenna No. 800 5-17

Table 5.12 – Parameters for antenna No. 197 5-18

Table 5.13 – Objectives for combined-objective optimisation 5-19

Table 5.14 – Parameter ranges for combined-objective optimisation 5-19

Table 5.15 – Best 25 solutions in terms of combined beamwidth from combined-objective GA 5-20

Table 5.16 – Parameters for antenna No. 2656 5-21

Table 5.17 – Parameters for antenna No. 3507 5-23

List of symbols

$\mathbf{E}$	electric field
$\mathbf{H}$	magnetic field
$\mathbf{A}$	magnetic vector potential
Φ	electric scalar potential
$\mathbf{J}$	current density
ω	angular frequency
β	wave number
λ	wavelength
ε_0	permittivity of free-space
μ_0	permeability of free-space
ε_r	relative permittivity
μ_r	relative permeability
ε	$= \varepsilon_0 \varepsilon_r$
μ	$= \mu_0 \mu_r$
$G(R)$	Green's function
$R(\ell', \ell)$	distance between source and observation points
$\hat{\ell}'$	unit vector tangential to the wire at the source point
$\hat{\ell}$	unit vector tangential to the wire at the observation point
$I(\ell')$	current at the source point
$U_n(\ell')$	basis function
$W_m(\ell)$	weighting function
$\mathbf{Z}_{mn}$	(m,n)th element of the impedance matrix
$\mathbf{V}_m$	mth element of the voltage matrix
$\mathbf{I}_n$	nth element of the current matrix
N	number of turns
C	circumference of SHA
(r, ϕ, θ)	spherical coordinates comprising radial, azimuth, and zenith components

List of acronyms

AR	Axial Ratio
BW	Beamwidth
CCS	Constant Circumferential Separation
CNC	Computer Numerical Control
CP	Circular Polarisation
CVS	Constant Vertical Separation
EFIE	Electric Field Integral Equation
EM	Electromagnetic
FDTD	Finite-Difference Time-Domain
GA	Genetic Algorithm
GPS	Global Positioning System
HPBW	Half-Power Beamwidth
INMARSAT	International Maritime Satellite Organization
MFIE	Magnetic Field Integral Equation
MoM	Method of Moments
PEC	Perfect Electric Conductor
SHA	Spherical Helical Antenna
SMA	Sub Miniature version A
SWG	Standard Wire Gauge
VNA	Vector Network Analyser
VSWR	Voltage Standing Wave Ratio

SHA-MoM	Author's own FORTRAN code for modelling SHA geometries using the Method of Moments
NEC	Numerical Electromagnetics Code
NSGA-II	Non-dominated Sorting Genetic Algorithm

1 Introduction

1.1 Purpose of research

The cylindrical helix antenna, first proposed by Kraus [1], and the planar spiral antenna [2-4] are both well known for producing circularly polarised (CP) radiation over a wide bandwidth. Such properties are useful for a range of applications, particularly satellite and other Earth-space communications where radio signals undergo Faraday rotation as they pass through the ionosphere. One of the limitations to both of these types of antenna, however, is their inability to produce good CP off-axis [5] which results in relatively low usable beamwidths.

This research seeks to provide a solution to this problem by finding an antenna which radiates good quality CP over both a wide bandwidth and a wide beamwidth. The antenna presented in this thesis, as a solution to this problem, is the Spherical Helical Antenna. This is essentially a helix which has been tapered to give it a spherical envelope. The Spherical Helical Antenna (SHA), first proposed by Cardoso and Safaai-Jazi [6], has received only limited coverage in publications [7-15] so has not been fully researched. It is the purpose of this thesis to expand on this work. In particular this research will investigate various modifications to the SHA including a novel scheme to define the spacing between turns, the consideration of a non-integer number of turns, truncation, and a novel balanced feed configuration. In addition, a search algorithm will be applied to optimise the antenna for minimum axial ratio (AR) on boresight, and maximum AR beamwidth.

1.2 Review of relevant research

It is important to consider research that has been published on helical and spiral antennas, and in particular the modifications made to these in the pursuit of improved performance. Indeed it is also important to look at the limited number of papers on the SHA. In Chapter 4 a genetic algorithm will be used to optimise the performance of the antenna. It is necessary therefore to consider optimisation techniques. A review of papers relevant to these areas follows.

1.2.1 The cylindrical helix antenna

The cylindrical helix, first proposed by Kraus [1], is a broadband antenna capable of providing a high gain and producing circular polarisation. It has two principle modes of operation – normal mode and axial mode. In normal mode, the radiation pattern is at a maximum in the plane which is normal to the axis of the helix. This mode occurs when the dimensions of the helix are small compared with the wavelength. In axial mode, the maximum radiation intensity is along the axis of the helix. CP is obtained in the axial mode when the circumference of the helix is close to a wavelength and the spacing between turns is around $\lambda/4$.

The current distribution on the helix is defined by three regions: near the feed end the current magnitude decays, in the middle region the current takes the form of a travelling wave, and towards the open end of the helix a standing wave pattern is formed. For first-order approximations, the current can be considered to follow a travelling wave pattern over the entire of the helix. Furthermore Krauss found [1] that the phase velocity on the helix varies according to the frequency of the wave in such a way that the increased-directivity condition is satisfied over a wide bandwidth. This condition requires that successive turns of the helix have a current distribution which is phase retarded by the same amount as the electrical separation between the turns. Thus the directivity in the axial direction is maximised.

1.2.2 Modifications to the helix antenna

Several authors have proposed modifications to the standard cylindrical helix in order to improve its performance. Wong and King [16] proposed a quasi-taper helix; a helix formed by connecting together a number of uniform cylindrical helices of different diameters. Through experimental results they showed that by using this approach it is not only possible to increase the bandwidth of the antenna but also to synthesize an antenna to attain a specified gain-frequency response. To demonstrate the increase in performance they compared the quasi-taper helix to both a uniform helix and a continuously tapered helix and obtained a 25% improvement in bandwidth. In addition to the bandwidth improvements they also showed that tapering the helix can improve its axial ratio.

Donn [17] investigated connecting a fully tapered conical section to the open end of the cylindrical helix in the search for better on- and off-boresight axial ratio performance. Significant improvements were shown through experimental results.

Kraft and Mönich [18] used MoM to investigate how tapering the ends of a cylindrical helix affected the axial ratio of the radiated wave. They pointed out that the polarisation due to the helix is significantly dependent on both θ and ϕ, therefore the consideration of axial ratio in only certain elevation planes is insufficient. As a consequence they considered the polarisation properties of the antenna over the entire radiation hemisphere and utilised a novel contour diagram to show this information diagrammatically.

1.2.3 The spiral antenna

Spiral antennas are well known for their wide bandwidth and CP properties, and have frequently been modelled using the Method of Moments [19-21]. It is usual to approximate the curved arms as a series of linear segments in order to simplify the analysis. It has been shown however [22] that many more segments are needed to approximate the curvature, than are required to approximate the current distribution. This has led some authors including Champagne [22] and Khamas and Cook [23,24] to develop curved segment analyses which they have shown to be significantly faster and less memory intensive.

Recently Saghi, Khamas, and Cook [25] have expanded their curved segment analysis to model a twin-arm Archimedean spiral conformal to the surface of a cylinder. They found that this antenna gave a wider beamwidth compared to a planar spiral.

1.2.4 The Spherical Helical Antenna (SHA)

Taking the idea of tapering the cylindrical helix one step further leads to the concept of a Spherical Helical Antenna (SHA). As the name suggests, this is a helical antenna with a spherical envelope instead of the usual cylinder. The SHA was first proposed by Cardoso and Safaai-Jazi [6] in 1993 although some earlier work by Mei and Meyer [26] in

1964 touched on a similar idea. Mei and Meyer published analytical solutions for the radiation patterns due to a spherical antenna with an anisotropic surface. The surface described conducts only in a spherically-spiral direction, so can be likened to a spherical helix with an infinite number of turns. Riblet [27] also proposed an antenna similar to the SHA. He showed a spherical antenna with an equiangular spiral slot which had been plotted onto a plane then projected onto the surface of the sphere.

Cardoso and Safaai-Jazi [6] suggested that unlike the cylindrical helix which provides circular polarisation (CP) only in the direction near to its axis, the SHA should produce good CP over a much wider beamwidth. This would be of huge benefit in many situations requiring CP where the receiving or transmitting antennas were not at fixed locations. Satellite communications is one such application where a fixed earth-based antenna may need to receive signals from satellites anywhere in the sky. A circularly polarised receiving antenna is beneficial in this case as it allows the reception of signals which have undergone Faraday rotation from passing through the ionosphere.

In their first paper Cardoso and Safaai-Jazi [6] used the wire antenna code ESP (Electromagnetic Surface Patch code) which is based on the Method of Moments, to model a coaxially-fed 10-turn SHA above a ground plane. Their results showed that reasonable CP was obtained over a 90° beamwidth – a significant improvement over the cylindrical helix. The limitation to this was that this CP over a wide beamwidth was maintained over a relatively narrow bandwidth (about 1.5 %.)

In a second paper Safaai-Jazi and Cardoso [7] considered the effect of altering the number of turns on the spherical helical antenna. They tested antennas with between 3 and 10 turns and showed that the number of turns is unimportant with regard to the radiation pattern and directivity. They stated that typical 3dB and 10dB beamwidths are 60° and 110° respectively, but that the polarisation over the beam varied greatly and was affected by frequency. In general the polarisation is elliptical, but under certain conditions, CP can be obtained over a wide beamwidth.

Hui et al. [8] also investigated the SHA using ESP, paying particular attention to its input impedance characteristics and gain, and how these vary with the number of turns. They noted that the size of an SHA is determined purely by its radius, and is independent of the number of turns. Conversely, for a cylindrical helix with a fixed separation between turns, increasing the number of turns increases its axial length. As a result the effect of adding turns is very different, and in fact detrimental to the performance of the SHA. They showed that both the gain and input impedance vary more rapidly the more turns there are, which results in lower bandwidths of operation being possible.

Hui et al. then proposed a hemispherical helical antenna [9,10]. The antenna was positioned above a ground plane and fed from its edge via a coaxial cable. Their motivation for effectively removing the lower half of a full SHA was mechanical stability. Through both theoretical and experimental results, and the consideration of 3-, 4-, and 5-turn geometries, they showed that the hemispherical antenna has similar radiation performance to that of a full spherical helical antenna. They obtained a 3dB axial ratio bandwidth of 14.6% from a 5-turn antenna, and a 3dB axial ratio beamwidth of 90° from a 3-turn antenna, although data was only given for a single elevation plane. It has been shown previously [18] that the polarisation of radiation from a cylindrical helix can vary dramatically with both θ and ϕ. This is also true of the SHA and will be considered in section 5.2 of this thesis. In a subsequent paper [11] Hui et al. constructed a 2×2 array from hemispherical helical antennas for INMARSAT-M satellite reception. They showed that due to the wide beamwidth over which the array elements produce good CP, their array outperformed others designed for the same application.

Chan et al. [12] proposed a modification to the feed of the hemispherical helical antenna. They added a linear segment between the edge and centre of the sphere as shown in Figure 1.1. Chan et al. showed that this improved the axial ratio.

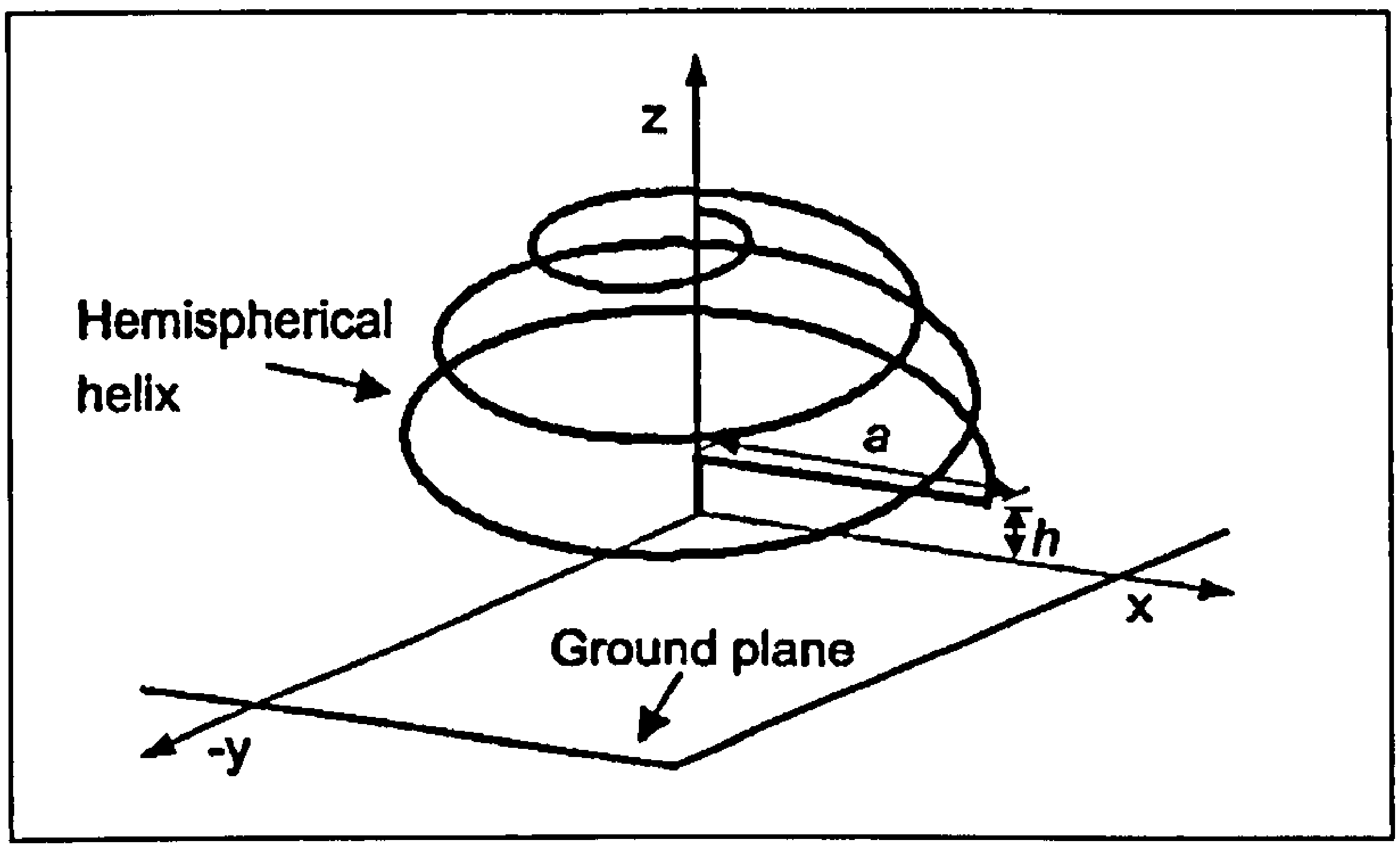

Figure 1.1 – Centre-fed hemispherical helical antenna reproduced from Chan et al. [12]

Zhang et al. [13] presented a hemispherical helical antenna with an additional matching section, tuned for global positioning system (GPS) reception. They addressed the issue of mechanical instability by proposing that the helix be printed onto the surface of a hemisphere. For their experimental measurements, they affixed copper tape to a polystyrene hemisphere.

Weeratumanoon and Safaai-Jazi [14] considered the effect of truncating a full SHA by terminating the wire before it reached the upper pole of the sphere. They showed that whilst the gain and radiation patterns remained fairly constant, the axial ratio on-axis could be significantly reduced, resulting in acceptable CP over a wider beamwidth. To demonstrate the effect this could have on the usable bandwidth of the antenna, they showed that a 4-turn SHA truncated after 2.75 turns produced an axial ratio of less than 3dB over an 80° beamwidth and over a 10% bandwidth. Ding et al. [15] also considered the effect of truncation. They presented computed results for a 7-turn SHA truncated to 3.5 turns, thus forming a hemispherical antenna which rests with its southern pole just above the ground plane. Note that this is an inverted form of the hemispherical helix previously proposed by Hui [9].

1.2.5 Antenna optimisation

There are many optimisation techniques which can be used to search a parameter-space for a set of parameters which produce either the best possible antenna characteristics or those which meet given criteria. Such methods include the Genetic Algorithm [28-30], Particle Swarm Optimisation [31], Simulated Annealing [32], Monte Carlo techniques, hill climbing, and random or exhaustive searches. Electromagnetic problems often have solution domains which contain non-differentiable and/or discontinuous regions [30] which can prevent some of the techniques from finding a solution. The GA however is robust [33] and is able to locate a globally optimum solution irrespective of the complexity of the solution space. Genetic Algorithms can also handle multi-objective problems [34] without the need for a predefined cost function.

Successful application of the GA to electromagnetic problems has been reported by various authors [21, 35-41]. In particular, Edwards et al [21] optimised a planar printed spiral with a GA, using curved segments and the Method of Moments. Their chosen GA [42] used Pareto ranking and was dual-objective – looking to minimise both the axial ratio on boresight and the angle of the main beam from the boresight direction.

Altshuler and Linden [35] used a GA to create a new design for an antenna rather than optimising a pre-existing design. The GA's goal was to produce an antenna which radiated uniform power over the entire radiation hemisphere. The only constraint was that the antenna should consist of a number of linear wires connected together in series. The GA was able to choose the position, orientation, and length of each of the wires, and used the NEC2 engine to perform simulations. A seven segment "crooked-wire" genetic antenna which met the design criteria was found using the GA.

1.3 Computer modelling

Antennas with simple geometries can be modelled analytically by making various assumptions about their current distributions. The dipole is one such example. Here the current is assumed to be sinusoidal with nulls at the end points. This has been found to be a good approximation through experimental measurements. From the current distribution, further expressions can then be derived to calculate its input impedance and radiation patterns. The complex geometry of the SHA makes the development of analytic expressions unfeasible. The current distribution along the wire will take on a complex form. Thus analytical techniques are not possible.

A traditional method of antenna design is through construction. Up until the mid-1980s it was common for antenna engineers to construct large numbers of test antennas of varying shapes and sizes, then to characterise them through time-consuming measurements. Over the last two decades available computing power has increased dramatically and has led to the realisation of a third method of antenna design – numerical methods. Although measurements remain an important part of antenna design, it is significantly more efficient to conduct the majority of the design work using computer simulations and use measurements to validate this work.

There are several numerical techniques for modelling antennas computationally including Finite Difference Time Domain (FDTD), Finite Element, and the Method of Moments (MoM). The latter of these is well suited for modelling wire antennas and has been selected for this research. It will be discussed in further detail in Chapter 2.

Method of Moments software is available both commercially (e.g. ESP [43]) and in the public domain (e.g. NEC [44]). Although NEC will be used to provide some validation, given in Chapter 3, the author has written custom FORTRAN code to model the SHA for this research. Custom software has the advantage that it allows full control over the model and its analysis. It also gives a better insight into the operation of the model which in turn allows for better interpretation of the results. In particular it has allowed the use of curved segments instead of the more usual choice of linear segments. This reduces the number of segments needed to accurately represent the curve, thus saving memory whilst increasing computational accuracy. Throughout this thesis the code will be referred to as SHA-MoM (Spherical Helical Antenna – Method of Moments.)

1.4 SHA geometry

Within the family of SHA antennas, there is scope for various different shapes of antenna, created by altering some of the various parameters available. These parameters will be discussed below.

Number of turns: Perhaps the most fundamental of all the parameters, the number of turns will play a critical part in defining the characteristics of the antenna. Suitable values might range from a single turn to many tens or hundreds of turns, and are not restricted to integers.

Radius of sphere: This sets the size of the imaginary sphere, around which the wire is wound. This dimension will be crucial in determining the frequency of operation of the antenna.

Spacing between turns: When considering a cylindrical helix, it is usual although not essential to maintain a constant separation between adjacent turns. Because of the additional dimension incorporated by the SHA there are various ways in which a constant separation can be defined. Two such methods will be used in this thesis and will be referred to as Constant Vertical Separation (CVS) and Constant Circumferential Separation (CCS). These are shown in Figures 1.2 and 1.3. The CVS geometry has been used in all the papers on the SHA to date [6-15], and is defined such that each turn is of the same height. A CVS-type SHA projected onto a cylinder would form a typical cylindrical helix with constant spacing. On a sphere, however, this definition leads to an uneven distribution of turns over the surface, which is clearly evident when viewing the antenna from the top or bottom (Figure 1.3a). The CCS method, proposed in this thesis, ensures a constant circumferential separation between adjacent turns. This means that the distance from one turn to the next, measured along the surface of the sphere remains constant and leads to more even spacing over the surface of the sphere. Figures 1.2 – 1.3 show the two methods of spacing being applied to a 10-turn SHA. The diagrams show views from the side and top of the antenna.

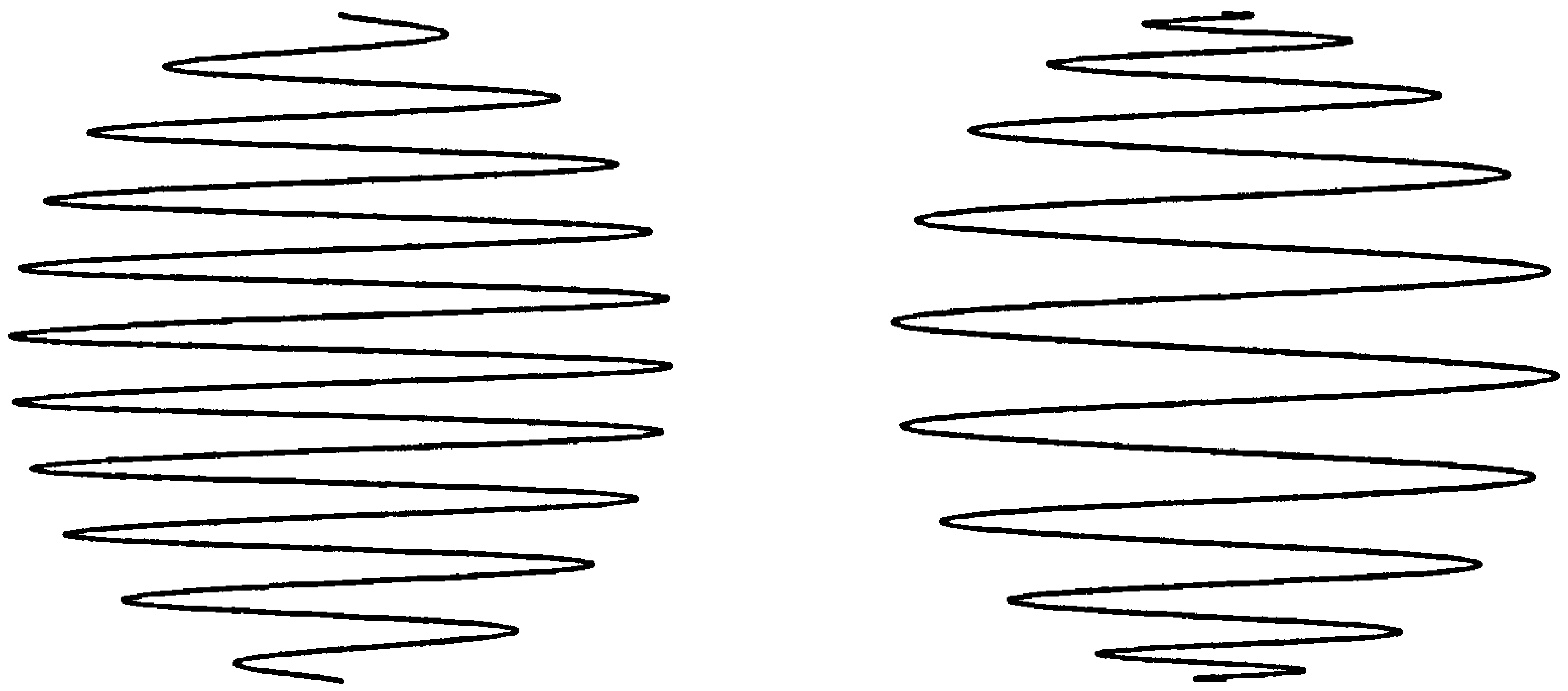

(a) Constant Vertical Separation (CVS) **(b) Constant Circumferential Separation (CCS)**

Figure 1.2 – SHA viewed from the side

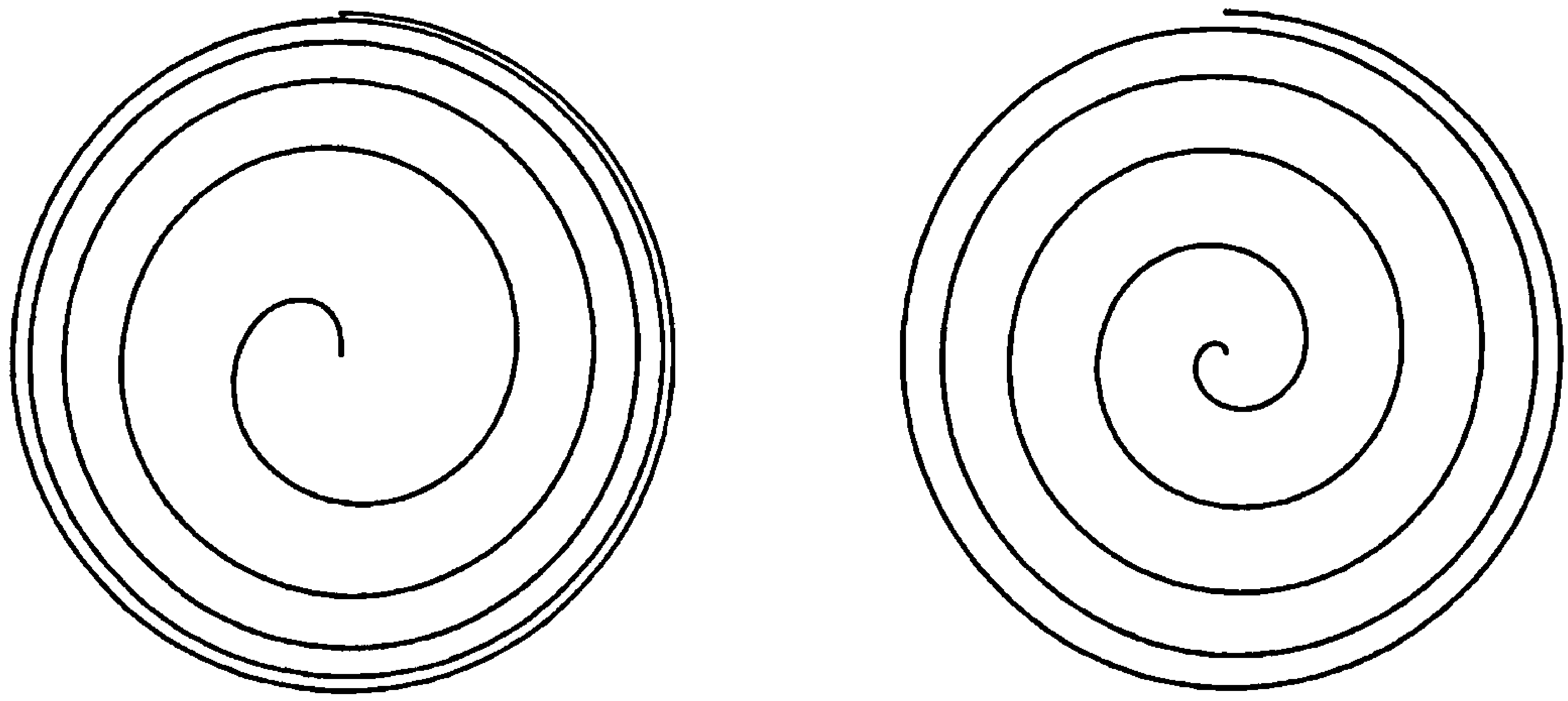

(a) Constant Vertical Separation (CVS) **(b) Constant Circumferential Separation (CCS)**

Figure 1.3 – SHA viewed from above (for clarity, only the upper hemisphere is shown)

Truncation: Instead of requiring the wire to start at the southern pole of the sphere, and extend up to the northern pole, the wire could be truncated. In this way a hemispherical SHA could be formed.

The Twin-arm balanced feed: A further variation to the antenna is to feed it from its centre via a dipole which extends to two spherical helical arms, one for the upper hemisphere, and one for the lower, as seen in Figure 1.4.

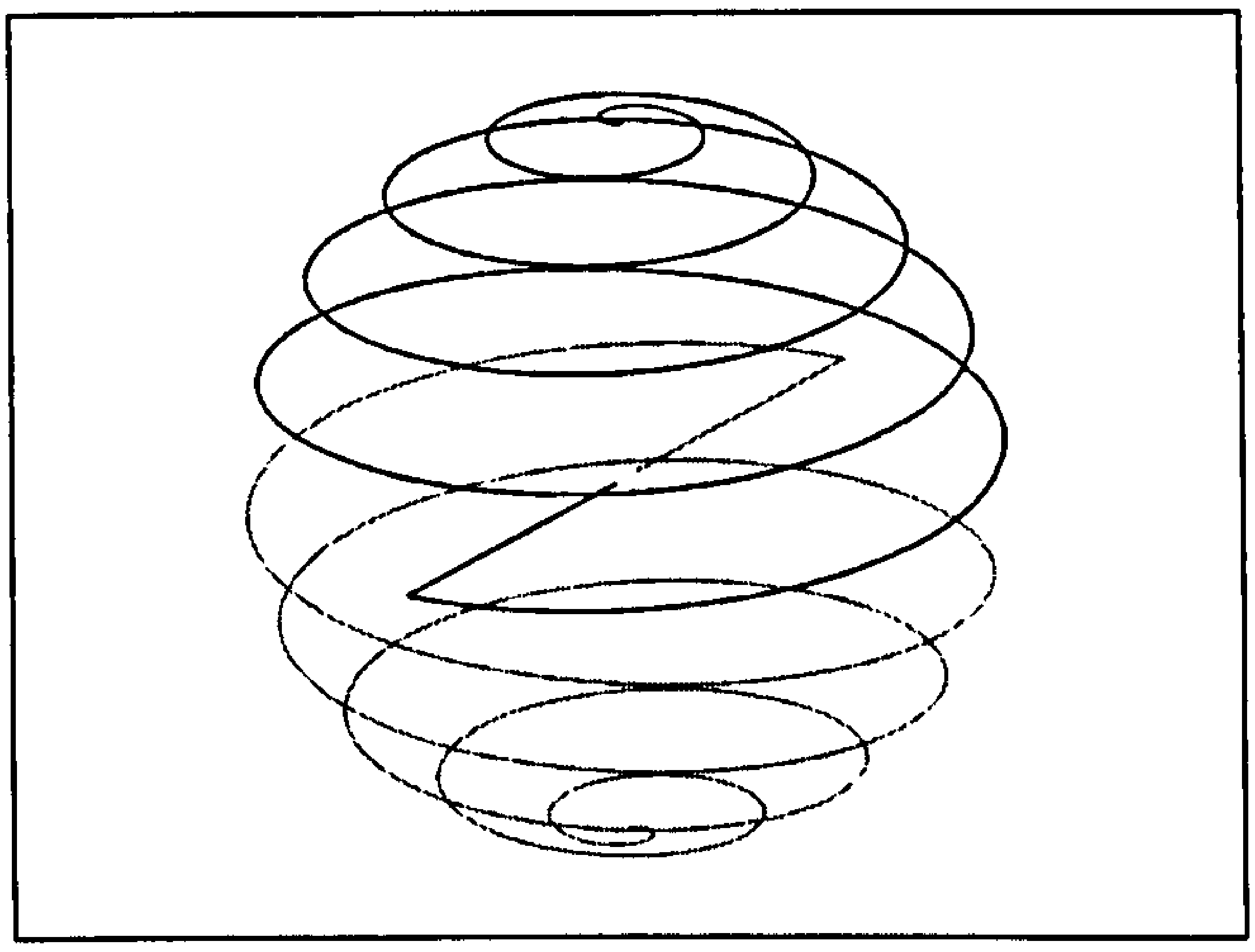

Figure 1.4 – Centre-fed Spherical Helical Antenna

1.4.1 Mathematical description

A mathematical description of both CVS and CCS geometries will be essential to model the antenna. These are given below in terms of spherical coordinates.

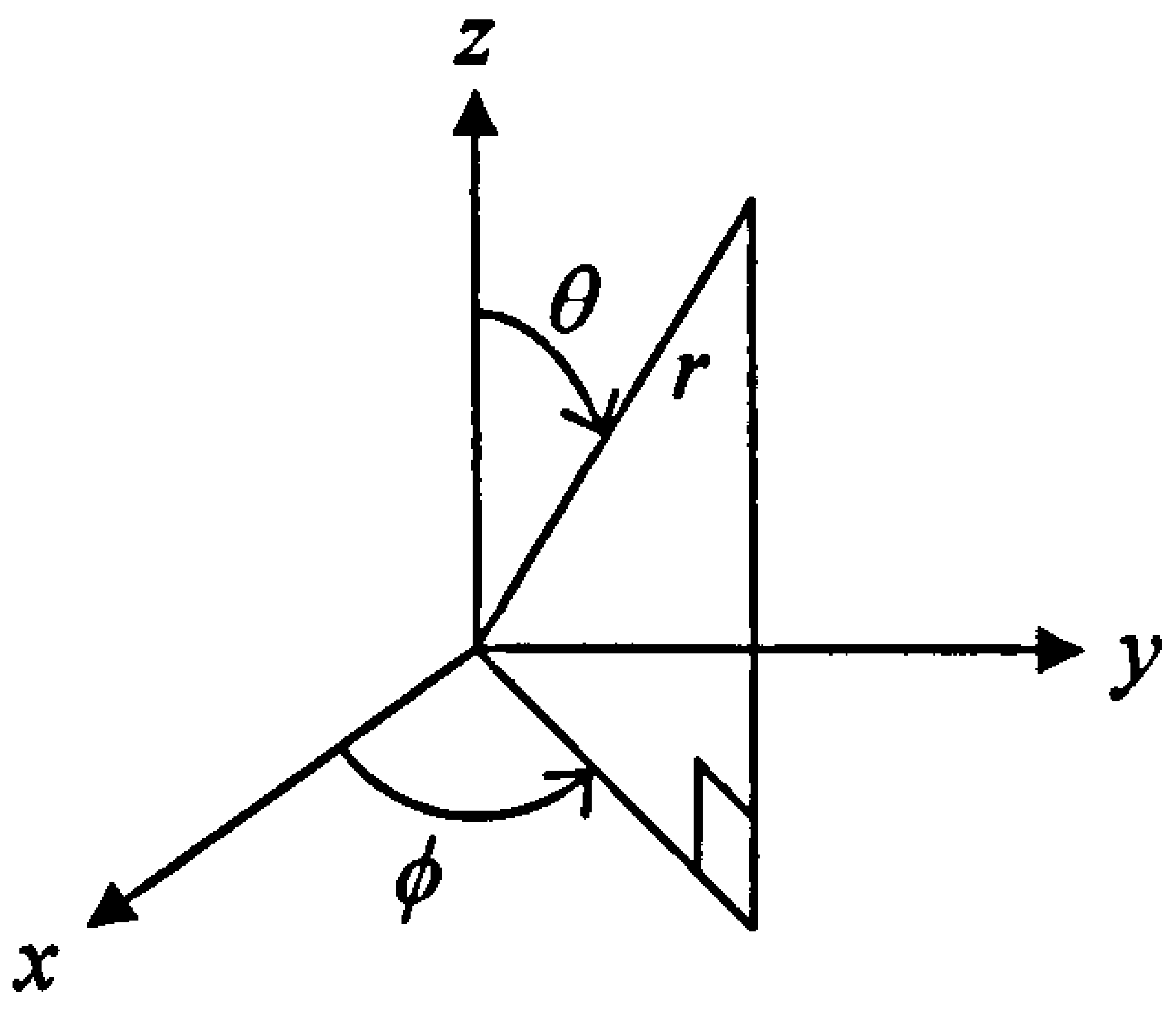

$$-\pi N \le \phi \le \pi N$$

$$\theta = \cos^{-1}\left(\frac{\phi}{\pi N}\right)$$

$$r = a$$

Constant Vertical Separation (CVS)

$$-\pi N \le \phi \le \pi N$$

$$\theta = \frac{\pi}{2} - \frac{\phi}{2N}$$

$$r = a$$

Constant Circumferential Separation (CCS)

Here N is the number of turns, and a is the radius of the sphere. Appendix A gives a complete mathematical description of both types of antennas, and develops the various expressions required to model the geometries with the Method of Moments.

1.5 Novel contributions

The Spherical Helical Antenna has received only limited coverage in publications, thus many of the results presented in this thesis have not been seen before. It is the first time that non-integer numbers of turns have been considered. It is also the first time the antenna has been optimised using a search algorithm.

In each of the limited number of papers published on the SHA the shape of the helix has been defined such that it has constant spacing when projected onto the vertical axis. This thesis will present a novel alternative to this shape which instead provides a constant circumferential spacing (CCS).

In order to apply the Method of Moments efficiently to the SHA antenna, an equation has been derived for calculating the impedance matrix elements between arbitrarily curved segments. Such an equation, which is rigorous for both half- and full- pulses, has not been seen in the literature. The use of curved segments to exactly represent the path of the wire, as opposed to approximating the curve with a number of linear segments, is also unusual. At the time the code was written, no other author had applied a curved segmentation technique to a non-planar geometry.

A major novelty of this research is the modelling of a Spherical Helical Antenna, fed from its mid-point via twin arms and a balanced feed. Such a geometry has not appeared in the literature.

To construct a prototype antenna, a method was sought that would allow an exact curvature to be obtained. Previous authors have reported using ping-pong balls [7], polystyrene [8,10], and foam [11] to help construct SHA geometries but have not discussed methods of ensuring the curvature produced matched that of the models. In this thesis, such a method is described. It involves cutting a groove in a spherical-shaped "mould" using a CNC milling machine. The wire is then wrapped around the mould to obtain the exact curvature required. The mould is then removed before the antenna is tested.

1.6 Overview of thesis

The next chapter presents the Method of Moments and other theory on which this research has been based. An Electric Field Integral Equation (EFIE) is developed which allows the modelling of arbitrarily curved segments without the need to approximate the helix with linear segments.

Chapter 3 gives details of the author's MoM code, SHA-MoM, which has been used to model the Spherical Helical Antenna. It then goes on to validate the code against both published results and data obtained using NEC. Good agreement is shown. The number of segments required for accurate representation of the current distribution along the wire is also considered, and curved segments are shown to be substantially more efficient than linear segments.

Chapter 4 presents results from the SHA-MoM code, and discusses the characteristics of the SHA, in particular its polarisation properties. Several modifications to the geometry are proposed including a novel scheme to define the spacing between turns, the consideration of a non-integer number of turns, truncation, and a novel balanced feed configuration.

Chapter 5 presents details of the GA which has been used to optimise the antenna, and describes why this GA was chosen. Results from several runs of the GA are shown. Also included is a discussion of how the objectives of the optimisation were chosen.

Chapter 6 describes how a prototype SHA was constructed with the aid of a purpose-milled mould which allowed wires to be shaped to exact curvatures. The design of a printed balun suitable for feeding the antenna is also covered. Radiation patterns and axial ratio measurements taken in an anechoic chamber are then presented.

Finally, chapter 7 summarises the research and provides some general conclusions. Recommendations for further work are also given.

References

1 J. D. Kraus, "Antennas", McGraw-Hill, New York, 2nd Ed., 1988.

2 J. Dyson, "The equiangular spiral antenna", IEEE Trans. Antennas Propagat., vol. 7 (2), pp. 181-187, Apr. 1959.

3 W. Curtis, "Spiral Antennas", IEEE Trans. Antennas Propagat., vol. 8 (3), pp. 298-306, May 1960.

4 J. Kaiser, "The Archimedean two-wire spiral antenna", IEEE Trans. Antennas Propagat., vol. 8 (3), pp. 312 - 323, May 1960.

5 H. King, and J. Wong, "Characteristics of 1 to 8 wavelength uniform helical antennas", IEEE Trans. Antennas Propagat., vol. 28 (2), pp. 291-296, Mar. 1980.

6 J. C. Cardoso and A. Safaai-Jazi, "Spherical helical antenna with circular polarisation over a broad beam", IEE Electronics Letters, vol. 29 (4), pp. 325-326, Feb. 1993.

7 A. Safaai-Jazi and J. C. Cardoso, "Radiation characteristics of a spherical helical antenna", IEE Proc-Microw. Antennas Propag, vol. 143 (1), pp. 7-12, Feb. 1996.

8 H. T. Hui, K. Y. Chan, and E. K. N. Yung, "The input impedance and the antenna gain of the spherical helical antenna", IEEE Trans. Antennas Propagat., vol. 49 (8), pp. 1235-1237, Aug. 2001.

9 H. T. Hui, K. Y. Chan, E. K. N. Yung, and X. Q. Shing, "Coaxial-feed axial mode hemispherical helical antenna", IEE Electronics Letters, vol. 35 (23), pp. 1982-1983, Nov. 1999.

10 H. T. Hui, K. Y. Chan, and E. K. N. Yung, "The low-profile hemispherical helical antenna with circular polarization radiation over a wide angular range", IEEE Trans. Antennas Propagat., vol. 51 (6), pp. 1415-1418, Jun. 2003.

11 H. T. Hui, E. K. N. Yung, C. L. Law, Y. S. Koh, and W. L. Koh, "Design of a small and low-profile 2×2 hemispherical helical antenna array for mobile satellite communications", IEEE Trans. Antennas Propagat., vol. 52 (1), pp. 346-348, Jan. 2004.

12 K. Y. Chan, H. T. Hui, and E. K. N. Yung, "Central-fed hemispherical helical antenna", IEEE APS Int. Symp., 2001, vol. 4, pp. 545 - 548, Jul. 2001.

13 Y. Zhang and H. T. Hui, "A printed hemispherical helical antenna for GPS receivers", IEEE Microwave and Wireless Components Letters, vol. 15 (1), pp. 10-12, Jan. 2005.

14 E. Weeratumanoon and A. Safaai-Jazi, “Truncated spherical helical antennas”, IEE Electronics Letters, vol. 36 (7), pp. 607-609, Mar. 2000.

15 Y. Ding, J.-H. Qiu, and W.-Y. Qin, “A New Spherical Helical Antenna”, IEEE APS Int. Symp., 2005, vol. 2A, pp. 292 - 295, Jul. 2005.

16 J. Wong and H. King, “Broadband quasi-taper helical antennas”, IEEE Trans. Antennas Propagat., vol. 27 (1), pp. 72-78, Jan. 1979.

17 C. Donn, “A new helical antenna design for better on-and off-boresight axial ratio performance”, IEEE Trans. Antennas Propagat., vol. 28 (2), pp. 264-267, Mar. 1980.

18 U. R. Kraft and G. Monich, “Main-beam polarization properties of modified helical antennas”, IEEE Trans. Antennas Propagat., vol. 38 (5), pp. 589-597, May 1990.

19 H. Nakano, K. Nogami, S. Arai, H. Mimaki, and J. Yamuchi, “A spiral antenna backed by a conducting plane reflector”, IEEE Trans. Antennas Propagat., vol. 34 (6), pp. 791-796, Jun. 1986.

20 H. Nakano, S. Kerner, and N. Alexopoulos, “The moment method solution for printed wire antennas of arbitrary configuration”, IEEE Trans. Antennas Propagat., vol. 36 (12), pp. 1667-1674, Dec. 1988.

21 R. M. Edwards, G. G. Cook, S. K. Khamas, R. J. Aidley, and B. Chambers, “Design of circularly polarised printed spiral antenna using dual objective genetic algorithm”, IEE Electronics Letters, vol. 34 (7), pp. 608-609, Apr. 1998.

22 N. J. Champagne II, J. T. Williams, and D. R. Wilton, “The use of curved segments for numerically modelling thin wire antennas and scatterers”, IEEE Trans. Antennas Propagat., vol. 40 (6), pp. 682-689, Jun. 1992.

23 S. K. Khamas and G. G. Cook, “Moment-method analysis of printed wire spirals using curved piecewise sinusoidal subdomain basis and testing functions”, IEEE Trans. Antennas Propagat., vol. 45 (6), pp. 1016-1022, Jun. 1997.

24 S. K. Khamas, G. G. Cook, R. J. Waldron, and R. M. Edwards, “Moment method analysis of printed single-arm wire spiral antennas using curved segments”, IEE Proc-Microw. Antennas Propag, vol. 144 (4), pp. 261-265, Aug. 1997.

25 Z. Saghi, S. K. Khamas, G. G. Cook, "Two Element Spiral Array Over A Cylindrical Contour", Loughborough Antennas and Propagation Conference (LAPC2006), pp. 161-164, Apr. 2006.

26 K. Mei and M. Meyer, “Solutions to spherical anisotropic antennas”, IEEE Trans. Antennas Propagat., vol. 12 (4), pp. 459-463, Jul. 1964.

27 H. B. Riblet, “A Broad-Band Spherical Satellite Antenna”, Proceedings of the IRE, vol. 48 (4), pp. 631-635, Apr. 1960.

28 Y. Rahmat-Samii and E. Michielssen, “Electromagnetic Optimization by Genetic Algorithms”, New York : Wiley, 1999.

29 R. L. Haupt, “An introduction to genetic algorithms for electromagnetics”, IEEE Antennas Propag. Mag., vol. 37 (2), pp. 7-15, Apr. 1995.

30 J. M. Johnson and V. Rahmat-Samii, "Genetic algorithms in engineering electromagnetics", IEEE Antennas Propag. Mag., vol. 39 (4), pp. 7-21, Aug. 1997.

31 J. Robinson and Y. Rahmat-Samii, “Particle swarm optimization in electromagnetics”, IEEE Trans. Antennas Propagat., vol. 52 (2), pp. 397-407, Feb. 2004.

32 S. Kirkpatrick, C. D. Gelatt, Jr., and M. P. Vecchi, “Optimization by simulated annealing,” Science, vol. 220, pp. 671-680, 1983.

33 A. Boag, E. Michielssen, and R. Mittra, “Design of electrically loaded wire antennas using genetic algorithms”, IEEE Trans. Antennas Propagat., vol. 44 (5), May 1996.

34 K. Deb, “Multi-Objective Optimization using Evolutionary Algorithms”, Wiley & Sons, Chichester, 2001.

35 E. E. Altshuler, and D. S. Linden, “Wire-antenna designs using genetic algorithms”, IEEE Antennas Propag. Mag., vol. 39 (2), pp. 33-43, Apr. 1997.

36 E. E. Altshuler, “Design of a Vehicular Antenna for GPS/IRIDIUM using a genetic algorithm”, IEEE Trans. Antennas Propagat., vol. 48 (6), pp. 968-972, Jun. 2000.

37 A. Boag, E. Michielssen, and R. Mittra, “Design of electrically loaded wire antennas using genetic algorithms”, IEEE Trans. Antennas Propagat., vol. 44 (5), pp. 687-695, May. 1996.

38 C. Delabie, M. Villegas, and O. Picon, “Creation of new shapes for resonant microstrip structures by means of genetic algorithms”, IEE Electronics Letters, vol. 33 (18), Aug. 1997.

39 S. Caorsi, “Genetic algorithms as applied to the numerical computation of electromagnetic scattering by weakly nonlinear dielectric cylinders”, IEEE Trans. Antennas Propagat., vol. 47 (9), pp. 1421-1428, Sep. 1999.

40 D. H. Werner, P. L. Werner, and K. H. Church, “Genetically engineered multiband fractal antennas”, IEE Electronics Letters, vol. 37 (19), pp. 1150-1151, Sep. 2001.

41 B. Chambers and A. Tennant, "Design of wideband Jaumann radar absorbers with optimum oblique incidence performance", IEE Electronics Letters, vol. 30 (18), pp. 1530-1521, Sep. 1994.

42 J. Horn, N. Nafpliotis, and D. E. Goldberg, "A niched Pareto genetic algorithm for multiobjective optimization", Proceedings of the First IEEE Conference on Evolutionary Computation, 1994.

43 E. H. Newman, "ESP5 The Electromagnetic Surface Patch Code", The Ohio State University, ElectroScience Laboratory (http://esl.eng.ohio-state.edu/codes/esp5_sum.php)

44 G. J. Burke and A. J. Poggio, "Numerical Electromagnetics Code (NEC) – Method of Moments," Technical Document 116, Naval Ocean Systems Center, San Diego, California, Jan. 1981.

2 Method of Moments

2.1 Introduction

The Method of Moments technique [1] is a powerful tool which can be used to model many types of antennas, including dipoles, helices, arrays, and printed antennas [2], including those with arbitrary configurations [3]. It works by breaking down an antenna problem into a set of simultaneous equations which can be solved using matrix techniques. The solution obtained gives the current distribution on the antenna, which in turn can be used to calculate radiation patterns, input impedance, and various other properties which are of use to engineers. The method is limited only by the computing power available to solve the simultaneous equations. In thin-wire antennas, such as the dipole, it is usual to assume that the current exists only on the wire surface and is axially directed. The field boundary conditions are then satisfied along the axis of the wire. This is known as the thin-wire or reduced kernel approximation, and has been used frequently [4,5,6].

2.2 Applying the Method of Moments

The first step in applying the Method of Moments to an antenna problem is to derive an appropriate Electric Field Integral Equation (EFIE) or Magnetic Field Integral Equation (MFIE). MFIEs are more suited to closed form geometries, whereas EFIEs work best with open form geometries [7]. It is simplest to model a wire antenna as a hollow tube of current with no ends, so an EFIE is sought. This is derived from Maxwell's equations, after which the boundary conditions of a specific geometry are imposed. The antenna is then broken up into a number of segments and the current distribution along the antenna approximated by a series of overlapping pulses. The mathematical description of the shape of these pulses is known as the basis function. Each of the current pulses gives rise to an impressed electric field everywhere on the antenna. By considering only the field from a particular current pulse (known as the source) and integrating this field over a particular segment (known as the observation segment) a value for the mutual impedance between the segments or pulses is found [8]. This can then be calculated for every pair of segments, and the values built up into a two-dimensional matrix known as the impedance (Z) matrix. When integrating over a particular observation segment, a weighting function, known as the testing function, is applied. If the basis and testing functions are identical, then it is known as the Galerkin method [9]. Throughout this thesis, piecewise sinusoidal functions have been used for both the basis and testing functions.

2.3 Source models

Two source models exist: delta-gap [9] and the magnetic frill generator [10]. The delta-gap model assumes that an excitation voltage is placed across a narrow gap between two connected segments. This voltage gives rise to an impressed electric field which exists only in the gap. The magnetic frill generator models a coaxial feed terminated with an aperture in an infinite ground plane. An annular region of circumferential current is then assumed to exist over this aperture and the fields due to this are calculated on the surface of the wire. Because the delta-gap model assumes a source which cannot physically exist, it is less accurate than the magnetic frill generator, but due to its simplicity it is more widely used. The magnetic frill generator model leads to a more accurate solution, particularly when comparing with results obtained experimentally. This is however at the expense of being much more computationally extensive to obtain [7].

2.4 Curved segments

The number of segments into which an antenna geometry is split is important in determining the computing resources needed, and the time taken to generate a solution; the larger the number of segments, the more memory is needed and the longer the solution takes. When dealing with non-linear geometries, the number of linear segments needed to approximate a curve can often exceed the number of segments needed to approximate the current distribution. This leads to inefficiencies in the model and are best avoided. Curved segments have been proposed [11,12] which alleviate this problem by defining segments which accurately follow the curve of the antenna. The drawback to this is an increased complexity in the impedance matrix calculations. Due to the desire to analyse Spherical Helix Antennas which may have a large number of turns, curved segments have been used throughout this thesis.

2.5 Derivation of impedance matrix equation

In order to model the Spherical Helix Antenna an EFIE is required which is suitable for curved segments. Such an equation can be derived as set out here. The first part of this development is based on the standard treatment of Maxwell's equations. Similar workings can be seen in [9]. Figure 2.1 shows the geometry and variables which will be used in the derivation. R defines the distance between the source and observation points while $\hat{\ell}'$ and $\hat{\ell}$ describe unit vectors tangential to the wire at these points.

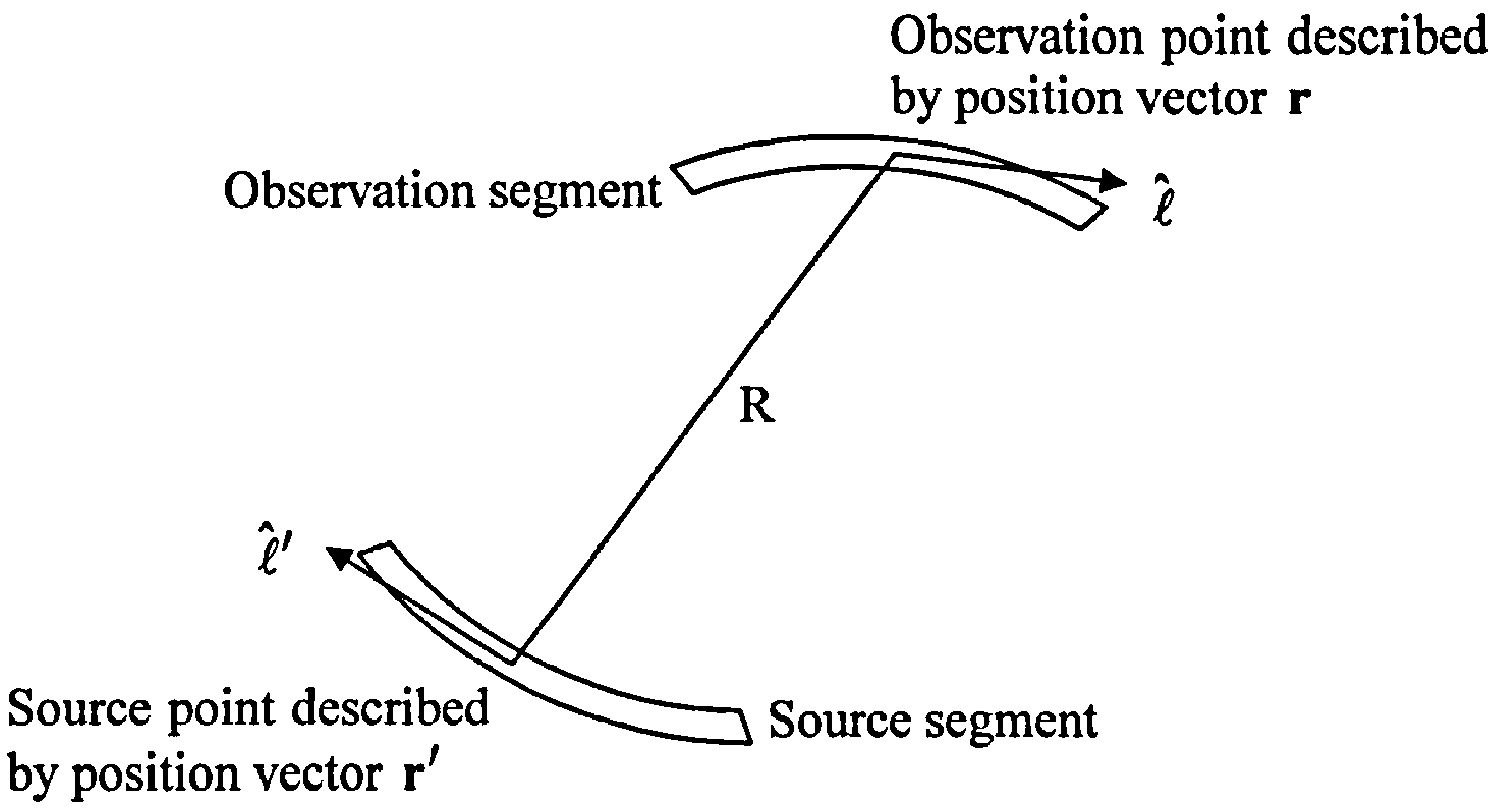

Figure 2.1 – Geometry and variables used in impedance matrix equation

We begin by defining:-

$$\mathbf{H} = \nabla \times \mathbf{A} \tag{1}$$

$$\nabla \Phi = -\mathbf{E} - j\omega\mu\mathbf{A} \tag{2}$$

and obtain the Lorentz gauge condition:-

$$\nabla \cdot \mathbf{A} = -j\omega\varepsilon\Phi \tag{3}$$

Recall Maxwell's 2nd equation:-

$$\nabla \times \mathbf{H} = j\omega \mathbf{D} + \mathbf{J}_T$$

which, using $\mathbf{D} = \varepsilon \mathbf{E}$ and (1) gives:-

$$\nabla \times \nabla \times \mathbf{A} = j\omega\varepsilon \mathbf{E} + \mathbf{J}$$

Substituting (2), then using the vector identity $\nabla \times \nabla \times \mathbf{A} = \nabla(\nabla \cdot \mathbf{A}) - \nabla^2 \mathbf{A}$

$$\nabla \times \nabla \times \mathbf{A} = j\omega\varepsilon(-j\omega\mu\mathbf{A} - \nabla\Phi) + \mathbf{J}$$

$$\nabla(\nabla \cdot \mathbf{A}) - \nabla^2 \mathbf{A} = \omega^2\varepsilon\mu\mathbf{A} - j\omega\varepsilon\nabla\Phi + \mathbf{J}$$

$$\nabla^2 \mathbf{A} = \nabla(\nabla \cdot \mathbf{A} + j\omega\varepsilon\Phi) - \omega^2\varepsilon\mu\mathbf{A} - \mathbf{J}$$

Using (3), then defining $\beta^2 = \omega^2\varepsilon\mu$ gives the vector wave equation:-

$$\nabla^2 \mathbf{A} + \beta^2 \mathbf{A} = -\mathbf{J}$$

Its solution in free space ($\varepsilon \to \varepsilon_0$, $\mu \to \mu_0$) for our current tube is:-

$$\mathbf{A} = \iint_S \mathbf{J} G(R) ds'$$

where $G(R) = \frac{e^{-j\beta R}}{4\pi R}$ and $R = \sqrt{(z-z')^2 + (\rho-\rho')^2 + a^2}$

$$\mathbf{A}(\mathbf{r}) = \iint_S \mathbf{J}_S(\mathbf{r}') G(R) ds' \qquad (4)$$

From (2) and (3) :-

$$\mathbf{E}_S = -j\omega\mu_0\mathbf{A} - \nabla\left(\frac{1}{-j\omega\varepsilon_0}\nabla \cdot \mathbf{A}\right)$$

$$\mathbf{E}_S = -j\omega\mu_0\mathbf{A} - j\frac{1}{\omega\varepsilon_0}\nabla(\nabla \cdot \mathbf{A})$$

$$\mathbf{E}_S = \frac{-j}{\omega\varepsilon_0}\left[\beta^2\mathbf{A} + \nabla(\nabla \cdot \mathbf{A})\right]$$

If PEC, then $\hat{\mathbf{n}} \times (\mathbf{E}_S + \mathbf{E}_i) = \mathbf{0}$

$$\hat{\mathbf{n}} \times \mathbf{E}_S = -\hat{\mathbf{n}} \times \mathbf{E}_i$$

$$\hat{\mathbf{n}} \times \mathbf{E}_i = \hat{\mathbf{n}} \times \frac{j}{\omega\varepsilon_0}\left[\beta^2 \mathbf{A} + \nabla(\nabla \cdot \mathbf{A})\right] \tag{5}$$

Substituting (4) into (5):-

$$\hat{\mathbf{n}} \times \mathbf{E}_i = \hat{\mathbf{n}} \times \frac{j}{\omega\varepsilon_0}\left[\beta^2 \iint_S \mathbf{J}_S(\mathbf{r}') G(R) ds' + \nabla\left(\nabla \cdot \iint_S \mathbf{J}_S(\mathbf{r}') G(R) ds'\right)\right]$$

$$\hat{\mathbf{n}} \times \mathbf{E}_i = \hat{\mathbf{n}} \times \frac{j}{\omega\varepsilon_0} \iint_S \left[\beta^2 \mathbf{J}_S(\mathbf{r}') G(R) + (\nabla' \cdot \mathbf{J}_S(\mathbf{r}'))\nabla' G(R)\right] ds'$$

where the ∇' means that the "del" operator now works on the source coordinates, $\mathbf{r}'$.

Applying the thin-wire approximation and defining $\hat{\ell}'$ as a vector which follows the contour of the spiral at the source point: -

$$\mathbf{J}_s(\mathbf{r}') = I(\ell')\hat{\ell}'$$

Using $\nabla' \cdot \left(I(\ell')\hat{\ell}'\right) = \frac{\partial}{\partial \ell'} I(\ell')$ gives: -

$$\hat{\ell} \cdot \mathbf{E}_i = \hat{\ell} \cdot \frac{j}{\omega\varepsilon_0} \int_{\ell'} \left[\hat{\ell}' \beta^2 I(\ell') G(R) + \left(\frac{\partial}{\partial \ell'} I(\ell')\right) \nabla' G(R)\right] d\ell'$$

Making use of $\hat{\ell} \cdot \nabla G(R) = \frac{\partial}{\partial \ell} G(R)$

$$\hat{\ell} \cdot \mathbf{E}_i = \frac{j}{\omega\varepsilon_0} \int_{\ell'} \left[\left(\hat{\ell} \cdot \hat{\ell}'\right) \beta^2 I(\ell') G(R) + \frac{\partial}{\partial \ell'} I(\ell') \frac{\partial}{\partial \ell} G(R)\right] d\ell'$$

Integrating by parts, noting that the current must be zero at the ends of the wire, gives:-

$$\hat{\ell}\cdot\mathbf{E}_i = \frac{j}{\omega\varepsilon_0}\int_{\ell'}\left[\left(\hat{\ell}\cdot\hat{\ell}'\right)\beta^2 I(\ell')G(R) - I(\ell')\frac{\partial^2}{\partial\ell\partial\ell'}G(R)\right]d\ell'$$

Applying the Method of Moments: -

$$\int_{\ell} W_m(\ell)\hat{\ell}\cdot\mathbf{E}_i d\ell = \frac{j}{\omega\varepsilon_0}\sum_n I_n \begin{bmatrix} \beta^2 \int_{\ell} W_m(\ell)\int_{\ell'}\left(\hat{\ell}\cdot\hat{\ell}'\right)U_n(\ell')G(R)d\ell' d\ell \\ -\int_{\ell} W_m(\ell)\int_{\ell'} U_n(\ell')\frac{\partial^2}{\partial\ell\partial\ell'}G(R)d\ell' d\ell \end{bmatrix}$$

where: -

$$W_m(\ell) = \text{weighting function} \quad = \begin{cases} \dfrac{\sin\beta(\ell-\ell_{m-1})}{\sin\beta\Delta\ell} & \ell_{m-1}\le\ell\le\ell_m \\ \dfrac{\sin\beta(\ell_{m+1}-\ell)}{\sin\beta\Delta\ell} & \ell_m\le\ell\le\ell_{m+1} \end{cases}$$

$$U_n(\ell') = \text{basis function} \quad = \begin{cases} \dfrac{\sin\beta(\ell'-\ell_{n-1})}{\sin\beta\Delta\ell'} & \ell_{n-1}\le\ell'\le\ell_n \\ \dfrac{\sin\beta(\ell_{n+1}-\ell')}{\sin\beta\Delta\ell'} & \ell_n\le\ell'\le\ell_{n+1} \end{cases}$$

comparing with $\sum_{n=1}^{N} Z_{mn}I_n = V_m$ gives: -

$$Z_{mn} = \frac{j}{\omega\varepsilon_0}\begin{bmatrix} \beta^2 \int_{\ell_m} W_m(\ell)\int_{\ell_n}\left(\hat{\ell}\cdot\hat{\ell}'\right)U_n(\ell')G(R)d\ell' d\ell \\ -\int_{\ell_m} W_m(\ell)\int_{\ell_n} U_n(\ell')\frac{\partial^2}{\partial\ell'\partial\ell}G(R)d\ell' d\ell \end{bmatrix} \qquad (6)$$

Equation (6) contains a differentiated Green's function, which will need to be solved analytically or computed numerically for each curve. Computing it numerically will add significant computing time to the model, whilst solving it analytically will require individual and tedious calculations to be incorporated into the code for every shape of curve to be modelled.

The following derivation uses integration by parts to remove the differentiation from the Green's function, thus allowing efficient implementation of the Method of Moments with arbitrary curves. Such a derivation has not been seen elsewhere in the literature, and is novel to this research.

Integrating the 2nd line of (6) by parts gives:-

$$Z_{mn} = \frac{j}{\omega\varepsilon_0}\left[\begin{array}{l} \beta^2 \int\limits_{\ell_m} W_m(\ell) \int\limits_{\ell_n} \left(\hat{\ell}\cdot\hat{\ell}'\right) U_n(\ell') G(R)\, d\ell' d\ell \\ -U_n(\ell') \int\limits_{\ell_m} W_m(\ell) \frac{\partial}{\partial \ell} G(R)\, d\ell \\ + \int\limits_{\ell_m} W_m(\ell) \int\limits_{\ell_n} \frac{\partial}{\partial \ell} G(R) \frac{\partial}{\partial \ell'} U_n(\ell')\, d\ell' d\ell \end{array}\right] \tag{7}$$

Then, again integrating by parts, the 2nd line of (7) becomes:-

$$-\Big[U_n(\ell')\left[W_m(\ell) G(R)\right]_{\ell\approx\ell_m}\Big]_{\ell'\approx\ell_n} + \left[U_n(\ell') \int\limits_{\ell_m} \frac{\partial}{\partial \ell} W_m(\ell) G(R)\, d\ell\right]_{\ell'\approx\ell_n} \tag{8}$$

And the 3rd line becomes:-

$$\left[W_m(\ell) \int\limits_{\ell_n} G(R) \frac{\partial}{\partial \ell'} U_n(\ell')\, d\ell'\right]_{\ell\approx\ell_m} - \int\limits_{\ell_m} \frac{\partial}{\partial \ell} W_m(\ell) \int\limits_{\ell_n} G(R) \frac{\partial}{\partial \ell'} U_n(\ell')\, d\ell' d\ell \tag{9}$$

Putting (8) and (10) back into (7) gives:-

$$Z_{mn}=\frac{j}{\omega\varepsilon_0}\left[\begin{array}{l}
\beta^2\int\limits_{\ell_m}W_m(\ell)\int\limits_{\ell_n}\left(\hat{\ell}\cdot\hat{\ell}'\right)U_n(\ell')G(R)\,d\ell' d\ell \\
+\left[W_m(\ell)\int\limits_{\ell_n}G(R)\frac{\partial}{\partial\ell'}U_n(\ell')\,d\ell'\right]_{\ell\approx\ell_m} \\
+\left[U_n(\ell')\int\limits_{\ell_m}\frac{\partial}{\partial\ell}W_m(\ell)G(R)\,d\ell\right]_{\ell'\approx\ell_n} \\
-\left[U_n(\ell')\left[W_m(\ell)G(R)\right]_{\ell\approx\ell_m}\right]_{\ell'\approx\ell_n} \\
-\int\limits_{\ell_m}\frac{\partial}{\partial\ell}W_m(\ell)\int\limits_{\ell_n}G(R)\frac{\partial}{\partial\ell'}U_n(\ell')\,d\ell' d\ell
\end{array}\right]
\begin{array}{l}
\\
\text{2nd line only needed if obs. pulse is half pulse} \\
\text{3rd line only needed if src. pulse is half pulse} \\
\text{4th line only needed if both are half pulses} \\
\\
\end{array}
\qquad (10)$$

Equation (10) will form the heart of the computer code used to model the antenna. The double integrations will need to be calculated numerically as no closed-form solutions exist for the complex geometry of the Spherical Helical Antenna. The second, third, and forth lines of the equation are only needed when either the source and/or observation pulses are half pulses (which occur either side of sharp bends in the wire.) When both source and observation are full-pulses, these terms equate to zero. Through the use of integration by parts, the equation has been engineered to avoid any differentiated Green's functions, G(R), which makes the calculations much easier. Within the integrations, the only quantities required are G(R), the distance between the source and observation point, and $\left(\hat{\ell}\cdot\hat{\ell}'\right)$ which is determined from the angle between the vectors tangential to the wire at the source and observation points.

Appendix A gives expressions for the G(R) and $\left(\hat{\ell}\cdot\hat{\ell}'\right)$ terms for the SHA geometries considered in this thesis.

2.6 Discussion

This chapter has described the Method of Moments and the theory on which this research has been based. Delta-gap and magnetic frill source models have been considered, and both of these will be incorporated into the SHA-MoM code. The ability to simulate two different source models will be useful when comparing results both with modelled results from other authors, and with measurements.

An equation for calculating the impedance matrix elements has been derived. This equation is rigorous for both half- and full- pulses, and can be used with segments which are arbitrarily curved. The equation includes double-integrations which must be solved numerically. Crucially the equation contains no differentiated Green's functions so can be applied to any shape of curve without the need for tedious analysis each time.

The following chapter will describe how the equation for mutual impedance developed here has been incorporated into the FORTRAN code SHA-MoM, which can then be used to model the Spherical Helical Antenna.

References

1 R. F. Harrington, “Field Computations by Moment Methods”, New York : Macmillan, 1968.

2 Newman, E.; Tulyathan, P., “Analysis of microstrip antennas using moment methods”, IEEE Trans. Antennas Propagat., vol. 29 (1), pp. 47-53, Jan. 1981.

3 H. Nakano, S. Kerner, and N. Alexopoulos, “The moment method solution for printed wire antennas of arbitrary configuration”, IEEE Trans. Antennas Propagat., vol. 36 (12), pp. 1667-1674, Dec. 1988.

4 K. K. Mei, “On the integral equation of thin wire antennas”, IEEE Trans. Antennas Propagat., vol. 13 (3), pp. 374-378, May 1965.

5 J. H. Richmond, “Digital computer solutions of the rigorous equations for scattering problems”, Proceedings of the IEEE, vol. 53 (8), pp. 796-804, Aug. 1965.

6 R. W. P. King, “The Linear Antenna - Eighty Years of Progress”, Proceedings of the IEEE, vol. 55 (1), pp. 2-16, Jan. 1967.

7 C. A. Balanis, “Antenna theory : analysis and design”, New York : Wiley & Sons, 2nd Ed., 1997

8 W. A. Imbriale, “Applications of the Method of Moments to Thin-Wire Elements and Arrays” in R. Mittra, “Numerical and asymptotic techniques in electromagnetics”, New York : Springer-Verlag, 1974.

9 W. L. Stutzman and G. A. Thiele, "Antenna theory and design", New York : Wiley, 1981.

10 L. L. Tsai, “A Numerical Solution for the Near and Far Fields of an Annular Ring of Magnetic Current”, IEEE Trans. Antennas Propagat., vol. 20 (5), pp. 569-576, Sep. 1972.

11 N. J. Champagne II, J. T. Williams, and D. R. Wilton, “The use of curved segments for numerically modelling thin wire antennas and scatterers”, IEEE Trans. Antennas Propagat., vol. 40, pp. 682-689, Jun. 1992.

12 Khamas, S.K.; Cook, G.G.; Waldron, R.J., “Moment-method analysis of printed circular wire-loop antenna using curved piecewise sinusoidal subdomain basis and test functions”, IEEE Trans. Antennas Propagat., vol. 44 (9), pp. 1303-1305, Sep. 1996.

3 Software and Validation

3.1 Introduction

Many of the results presented in this thesis have been produced using independent MoM code developed specifically for this research. This has allowed the implementation of curved segments [1,2] which would not otherwise have been possible. It is of course crucially important that the code be thoroughly validated against external controls before the data it outputs can be trusted. Validation has been achieved in two ways; against published results, and against a piece of well known EM software.

A small number of published papers [3-8] have addressed various geometries of Spherically Helical Antennas (SHAs). These have incorporated both modelled and measured results with various parameters of the antennas being reported graphically. It was possible to reproduce many of these graphs with the independent MoM code, and some of these comparisons will be given later in this chapter.

Due to the desire to model a unique geometry for a SHA, a centre-fed balanced variety, which has not been reported elsewhere, a second source of control data was also required. NEC [9] was chosen for this due to its strong reputation and widespread use. The main drawback to using NEC for SHA geometries is its restriction to using linear segments, which will be shown to add a great deal of inefficiency to the computations involved in the modelling. Comparisons with NEC will be presented in section 3.4 of this chapter.

3.2 SHA-MoM code

Dedicated FORTRAN code, referred to in this thesis as SHA-MoM (Spherical Helical Antenna – Method of Moments code) was written to assist the research. The main reason for developing custom code was to allow the modelling of curved segments – a feature which is not available in any of the commercial or public domain implementations of the Method of Moments. In addition to this, SHA-MoM has allowed a greater control over the source model and choice of basis/testing functions. It has also allowed a greater understanding of the physics and maths which form the foundation of antenna analysis and of how the results are being produced and thus how the results can be interpreted.

3.2.1 Program operation

The SHA-MoM code takes as its input a text file named `parameters.csv`. This file contains a list of options and values needed to define the geometry of the antenna and indicate what output data the program should produce. After reading this file, the program calculates the mutual impedance between each pair of segments using equation (10) given in Chapter 2. These values form the impedance matrix which is then inverted and multiplied by the voltage matrix to give the current distribution along the wire. From this distribution, various characteristics of the antenna can then be calculated. These include the far-field radiation patterns, gain and axial ratio values, and the input impedance of the antenna. Appendix B gives details of the expressions used by SHA-MoM for calculating these values.

3.2.2 Input parameters

A list of parameters which can be passed to the program are given in Table 3.1. If a particular parameter is not specified in the input file, the default value shown in the table is applied.

Name	**Description**	**Default**
GEOMETRY_TYPE	Type of geometry to model:- 1 = CVD type SHA 2 = CCD type SHA 3 = Twin-arm centre-fed CCD type SHA 4 = Cylindrical helix above g.p. 5 = Monopole above a ground plane 6 = CVD type upper hemisphere above g.p. 7 = (not implemented) 8 = Edge-fed CVD hemisphere above g.p.	1
N	Number of turns	7
R	Radius of sphere (cm)	1.95
H	Height of sphere above ground plane (cm)	0.4
WIRE_RADIUS	Wire radius (cm)	0.04
FREQUENCY	Frequency (MHz)	2870
NLS	Number of segments in linear section	1
NS	Number of segments in curved section(s) (see notes below)	50
NS2		0
GP_PRESENT	0 = antenna is in free space 1 = a ground is present	1
END_POINT	The proportion of the wire in the lower hemisphere before truncating	1.0
END_POINT2	The proportion of the wire in the upper hemisphere before truncating	1.0

`MAG_FRILL`	0 = use delta gap source model 1 = use magnetic frill source model	0
`COAX_OUTER_MULT`	Radius of coax outer as a multiple of WIRE_RADIUS (only used when MAG_FRILL = 1)	0.45

Table 3.1 – List of parameters for setting the geometry of the antenna to be modelled

Notes:-

The meaning of `NS` and `NS2` depends on the `GEOMTERY_TYPE` used.

It is often desirable to model a particular antenna whilst varying some parameter over a specified range. The SHA-MoM code allows for this by the inclusion of the '`RUNS`' parameter, shown in Table 3.2, which indicates that the model should be repeated a given number of times. The parameter to be varied is then specified by the word '`VARIABLE`' followed by a list of values to be used. An example of such is shown in Figure 3.1.

`RUNS`	Number of times to repeat the model whilst varying one or more of the parameters	1

Table 3.2 – Additional parameter to allow multiple models to be analysed

```
RUNS,3
GEOMETRY_TYPE,1
N,7
R,VARIABLE
1,1.85
2,1.95
3,2.05
H,0.4
```

Figure 3.1 – Example of a parameters.csv file

The code generates a series of text files in which the results of its calculations are stored. The main file produced contains a line of data for each run which summarises the important antenna parameters such as input impedance, gain, and axial ratio. In addition to this, individual text files can be produced, one for each of the runs, which contain more detailed output data including the current distribution along the wire, and the far-field pattern. The choice of what output data is produced can be set by the inclusion of additional option lines in the `parameters.csv` file. These are shown in Table 3.3 which also explains in more detail what data can be produced.

`SAVE_INDIVIDUAL_FILES`	0 = produce only the summary output file (all the following options are then ignored)	1
`SAVE_GEOMETRY`	1 = record the coordinates of each of the segments	0
`SAVE_V_MATRIX`	1 = record the voltage matrix	1
`SAVE_Z_MATRIX`	1 = record the impedance matrix	1
`SAVE_Z_MATRIX_DEBUG`	1 = record various intermediate values produced whilst calculating the impedance matrix (useful for debugging)	0
`SAVE_I_MATRIX`	1 = record the current matrix	1
`SAVE_I_EXTENDED`	1 = record a more detailed current distribution by interpolating the current matrix	1
`CURRENT_SUBSEGMENTS`	Sets the number of points per segment at which to record the current distribution	50
`SAVE_FAR_FIELD`	1 = record the far-field pattern including field strength and axial ratio	1
`NUMBER_OF_CUTS`	Determines the number of radiation patterns to compute	2

Table 3.3 – List of parameters for controlling the output data produced by the program

3.3 Validation with published results

The simplest form of the Spherical Helical Antenna is that shown in Figure 3.2. It consists of a single wire shaped as if to wrap around an imaginary sphere and fed against a ground plane. There are three parameters of the geometry which can be varied; the radius of the sphere, R; the height above the ground plane, h; and the number of turns in the wire, N.

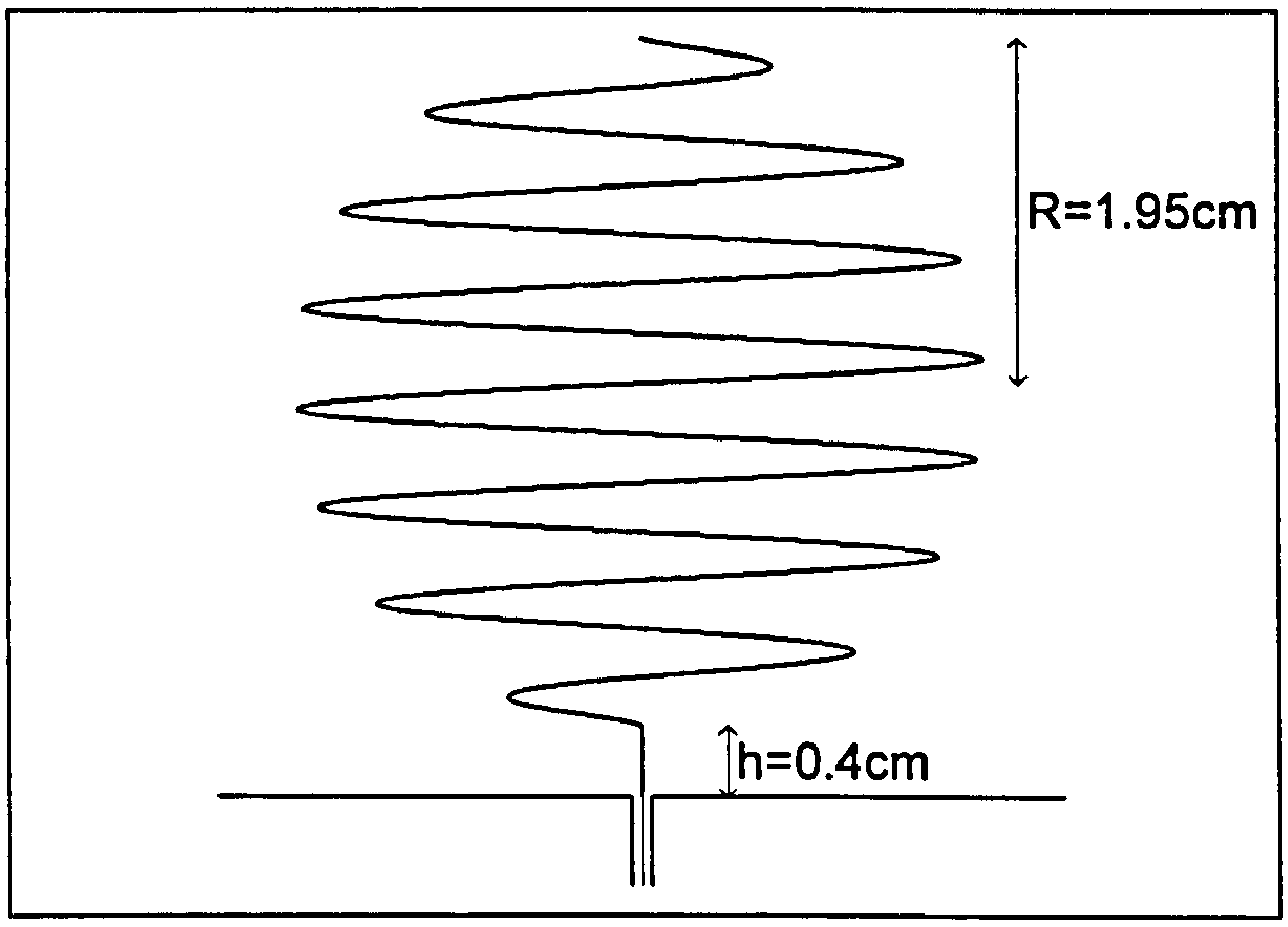

Figure 3.2 – Geometry of a simple Spherical Helical Antenna

Hui[7] has modelled this shape of antenna using the commercial Electromagnetic Surface Patch (ESP) code, and his paper includes graphical results for an antenna with parameters N=7, R=1.95cm, h=0.4cm. This provided an excellent opportunity for confirming the reliability of the SHA-MoM code. The comparison can be seen in Figure 3.3, where the lighter of the two graphs is copied directly from Hui's paper, and overlaid onto this is the output of the SHA-MoM code. The graph shows the magnitude and phase progression of the current along the antenna.

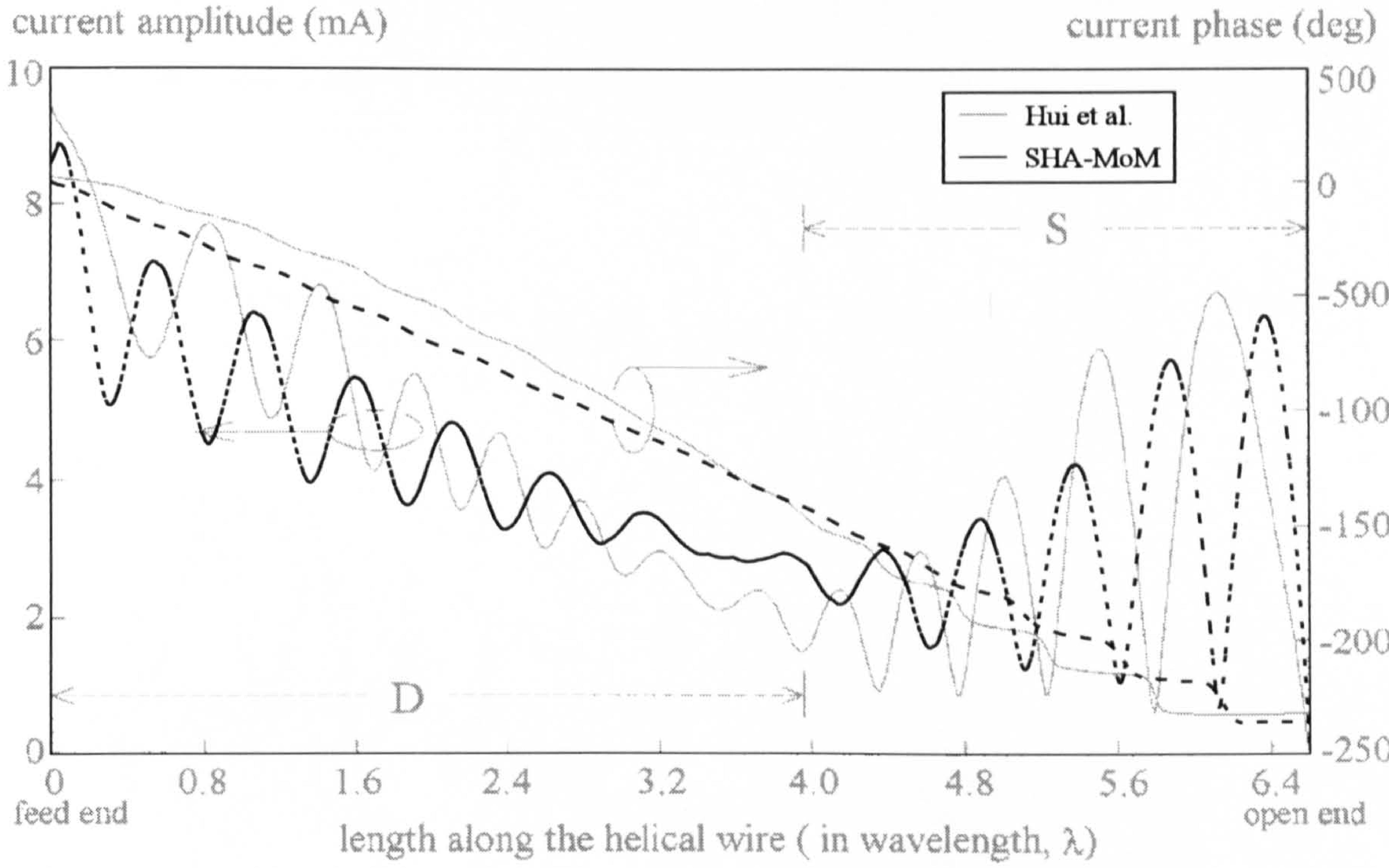

Figure 3.3 – Comparison of current magnitude and phase progression with published results

(N=7, R=1.95cm, WireRad=0.04cm, h=0.4cm, NS=variable, NLS=1, f=2.87GHz)

Although the general shapes of the graphs in Figure 3.3 agree, there is a warping along the x-axis, particularly near the ends. The ends correspond to the very top and bottom of the sphere, where the turns are wrapped very tightly. It is expected that the fluctuations in the current along the wire have constant period, but Hui's graph seems to show stretching at the ends. It was suspected that Hui may have plotted the current against the angular quantity ϕ instead of ℓ.

By replotting the current amplitude and phase against ϕ instead of ℓ, and overlaying this onto Hui's graph, much better agreement is obtained. Figure 3.4 shows this.

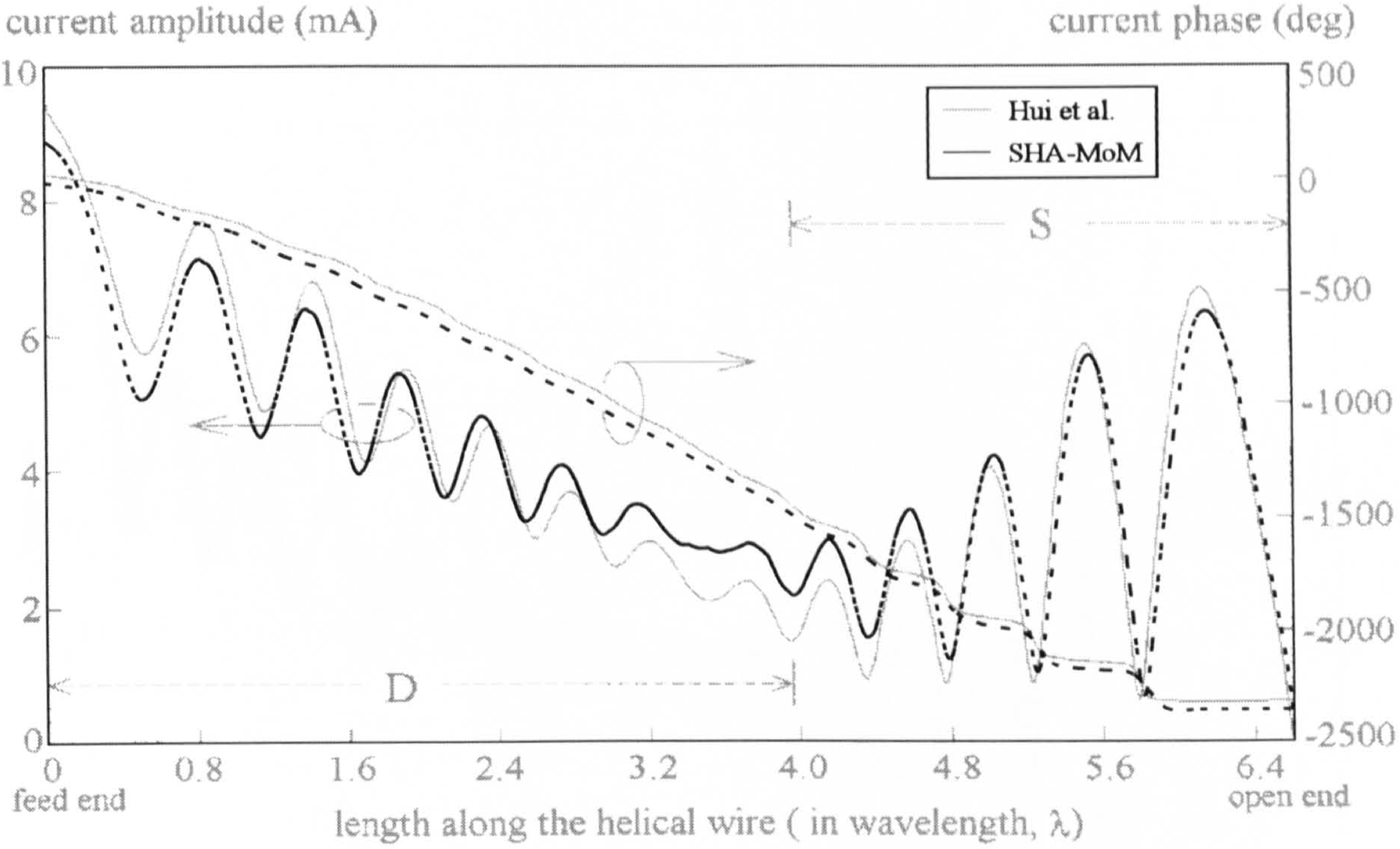

Figure 3.4 – Current magnitude and phase progression and overlay plotted against ϕ instead of ℓ

(N=7, R=1.95cm, WireRad=0.04cm, h=0.4cm, NS=variable, NLS=1, f=2.87GHz)

To check this assumption, the same model was run in NEC. See Figure 3.5. This confirmed that the spacing between the current oscillations should be equally spaced, providing further evidence that Hui may have mislabelled his x-axis or misinterpreted the output from his model.

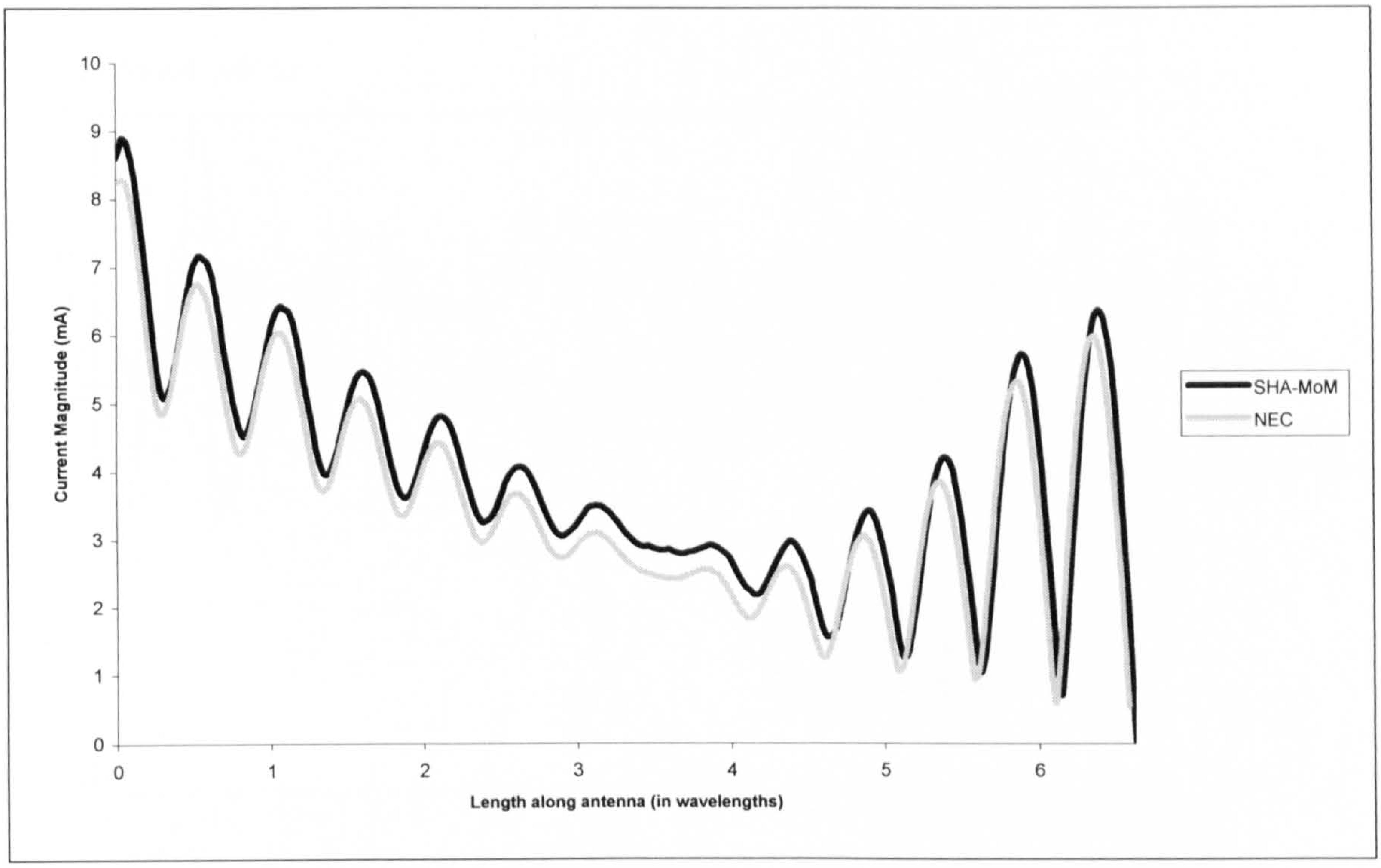

Figure 3.5 – Current magnitude along wire of 7-turn SHA, modelled with NEC and SHA-MoM

In addition to the current distributions, Hui published a graph showing how the input impedance of the antenna varied with frequency. Input impedance is a sensitive antenna parameter so obtaining good agreement provides confidence that the code is correct. The result of this comparison is shown in Figure 3.6.

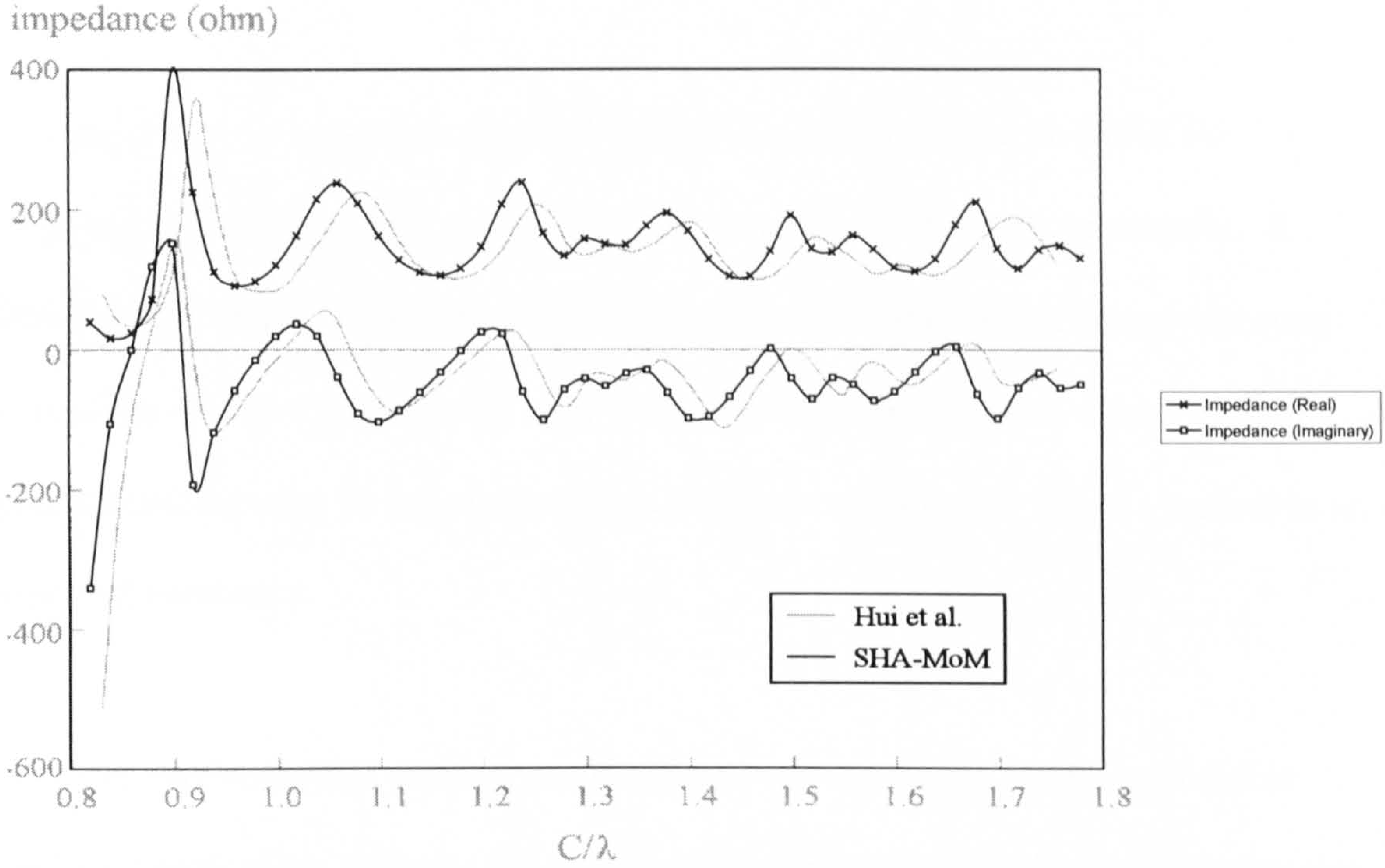

Figure 3.6 – Comparison of impedance characteristics
(N=7, R=1.95cm, WireRad=0.04cm, h=0.4cm, NS=50, NLS=1, f=variable)

3.4 Validation with NEC

The Numerical Electromagnetics Code (NEC) [9] is a freely available program which also implements the Method of Moments. It was developed at the Lawrence Livermore Laboratory, Livermore, California, under the sponsorship of the Naval Ocean Systems Center and the Air Force Weapons Laboratory.

Utilising the combination of an EFIE for thin-wire structures and an MFIE for voluminous structures, NEC can model a large number of different geometries. It allows for the inclusion of non-radiating networks and transmission lines connecting parts of the structure, perfect and imperfect conductors, and lumped-element loading. A ground plane can also be incorporated which may be modelled as either a perfect or an imperfect conductor.

NEC was used to further confirm that the SHA-MoM code was producing reliable results for each of the different SHA geometries discussed in this thesis, including the centre-fed SHA seen in Figure 3.7.

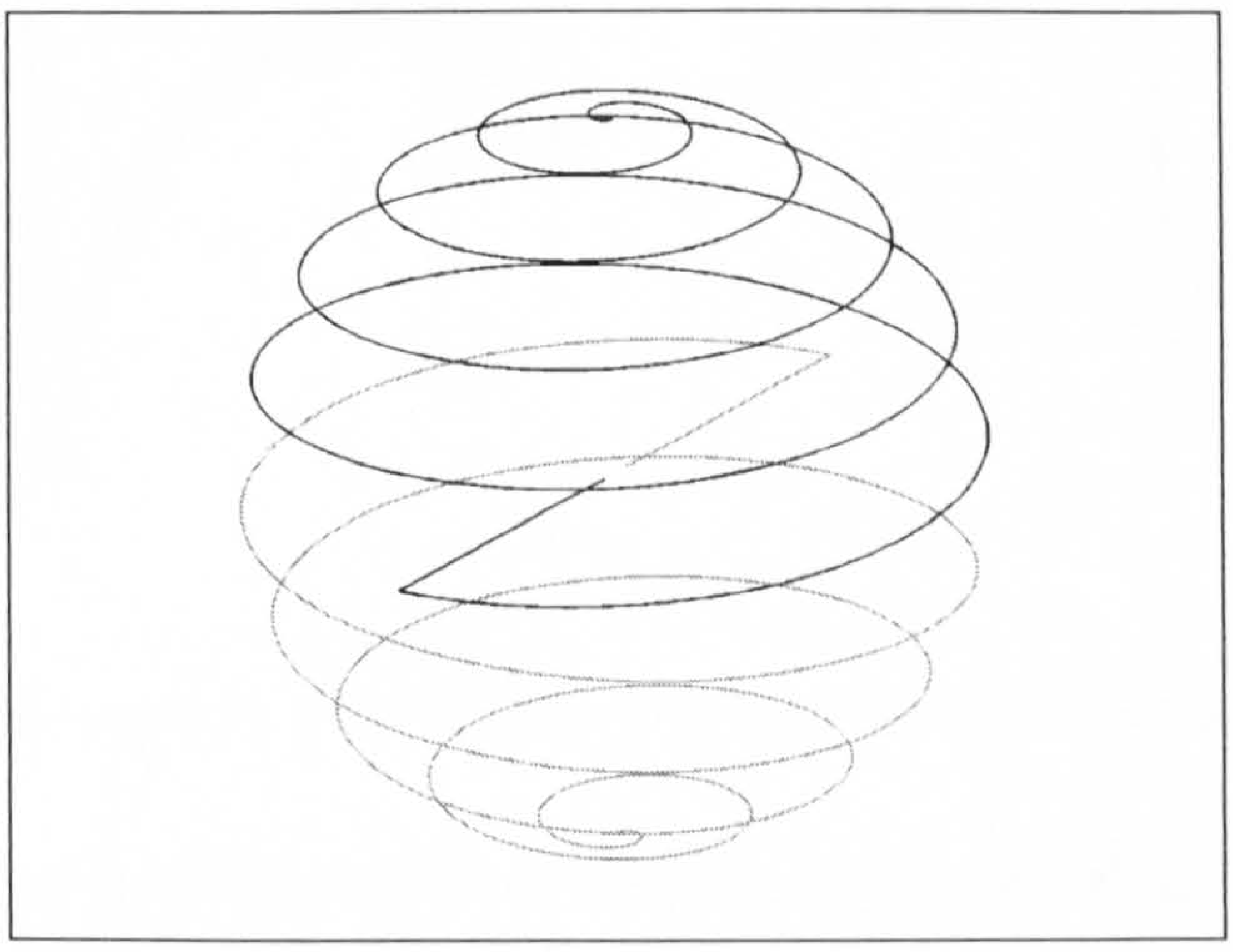

Figure 3.7 – Centre-fed Spherical Helical Antenna

The geometry in Figure 3.7 has been the main focus of this research so validating the output of the SHA-MoM code for this antenna was of utmost importance. Figure 3.8 and Figure 3.9 show the real and imaginary parts of the input impedance of the antenna against frequency with results presented from both the MoM code and NEC.

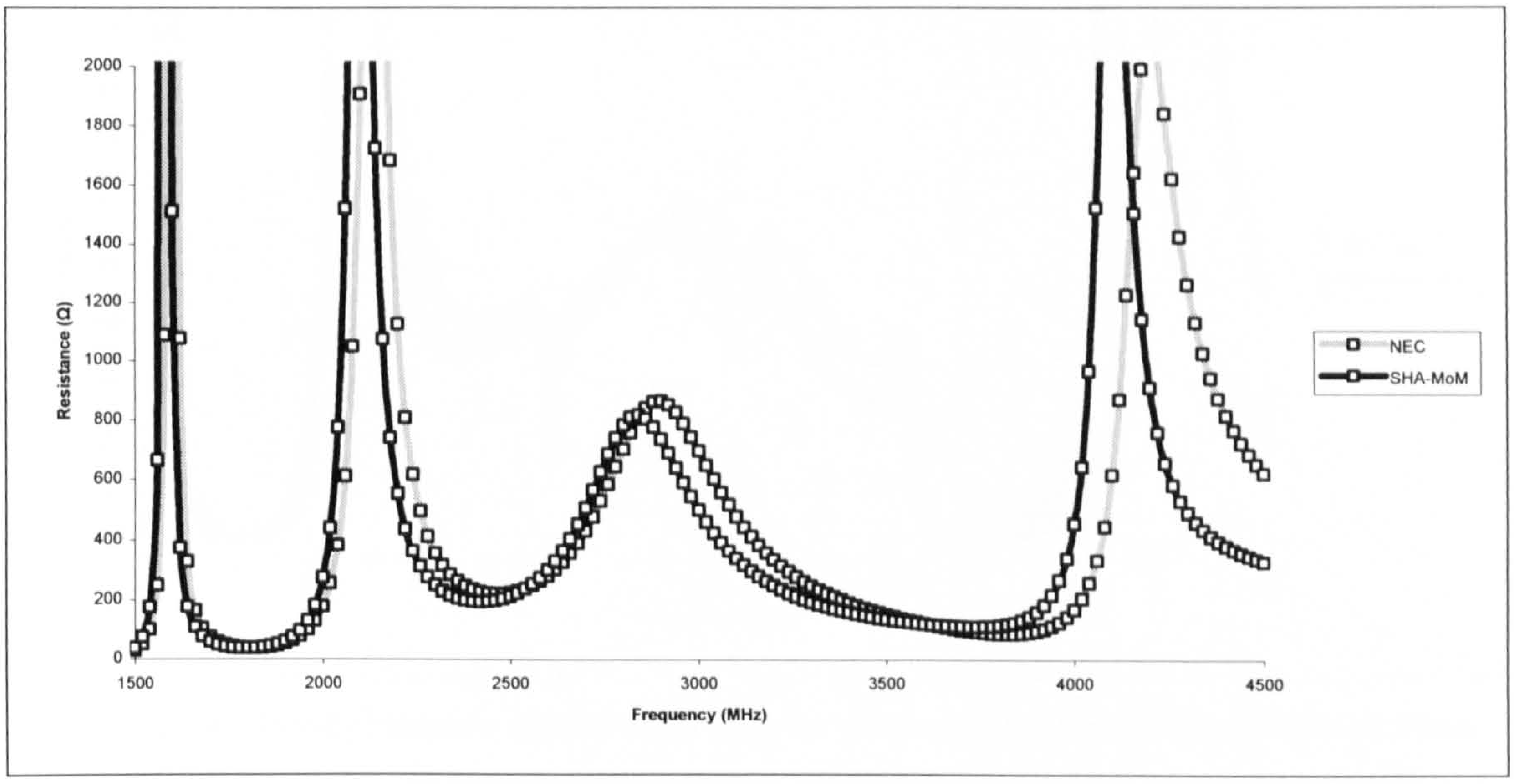

Figure 3.8 – Input resistance for a 7-turn centre-fed SHA of radius 1.95cm in free-space

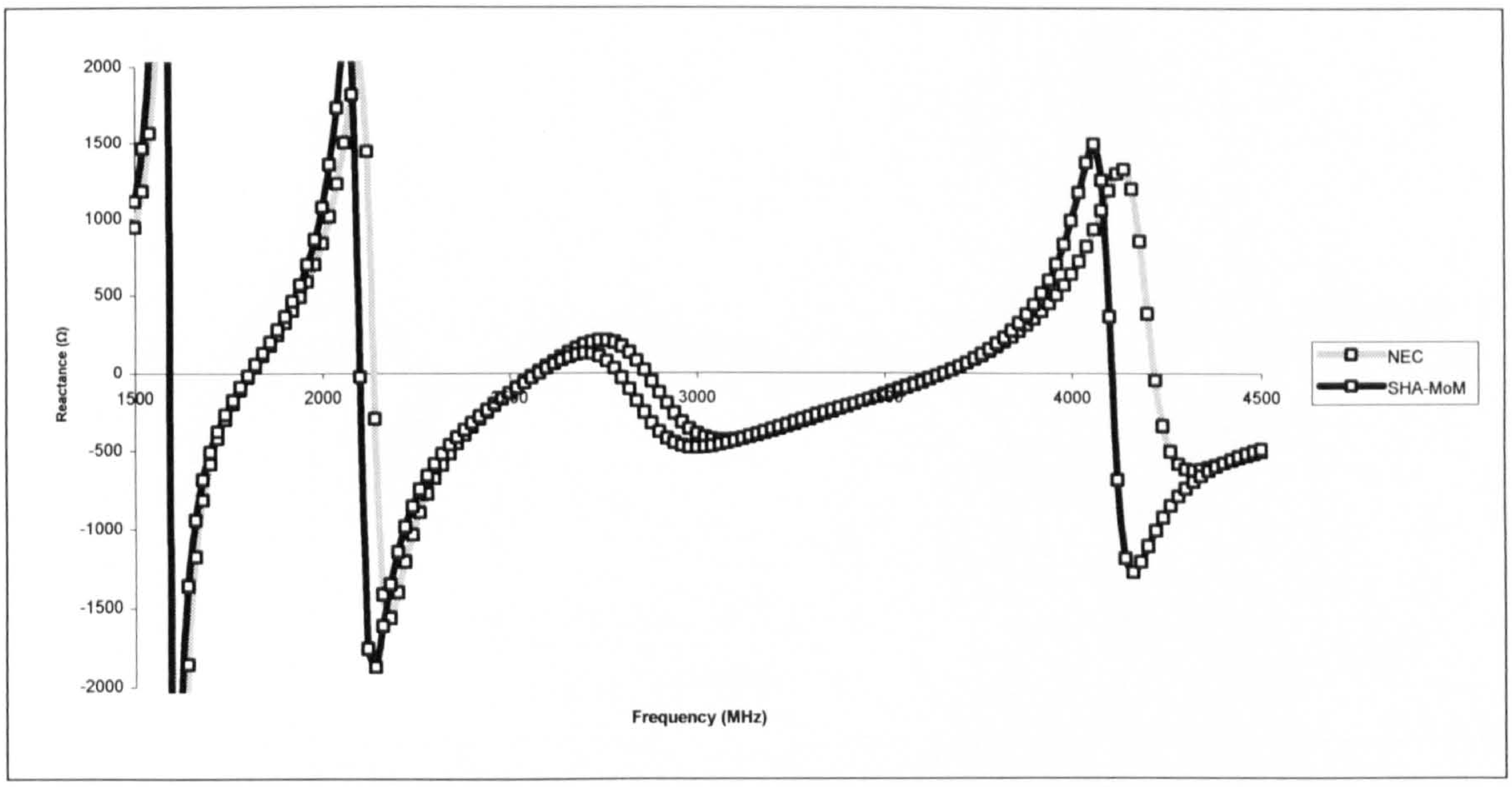

Figure 3.9 – Input reactance for a 7-turn centre-fed SHA of radius 1.95cm in free-space

The graphs show good agreement, particularly in the maximum and minimum values of input impedance. There seems to be a slight shift along the frequency axis which is believed to be a product of the differing segmentation schemes used by NEC and the

MoM code. The centre-fed SHA will also be considered positioned above an infinite ground-plane. Figure 3.10 and Figure 3.11 show similar comparisons for this modified geometry.

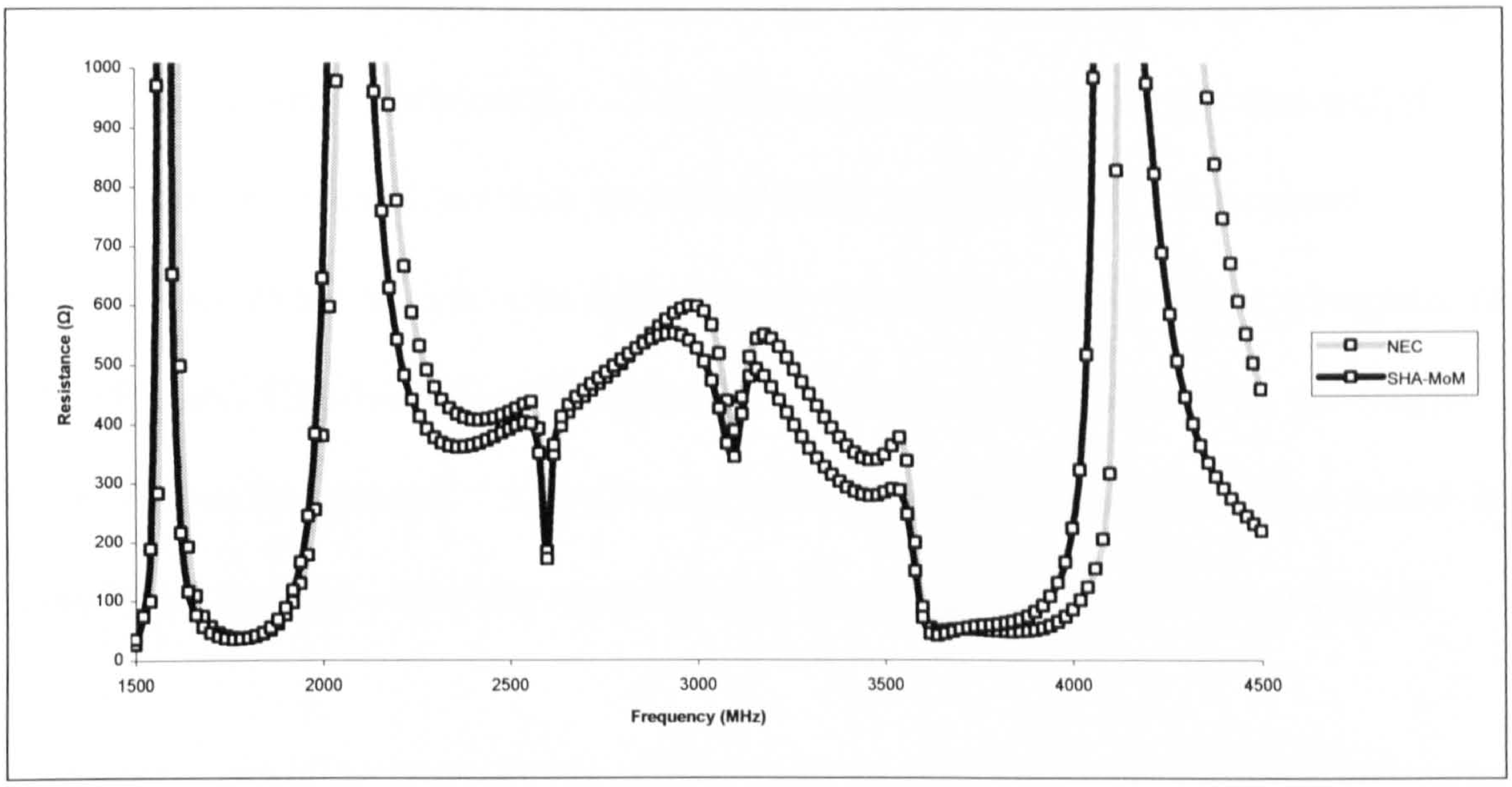

Figure 3.10 – Input resistance against frequency for a 7-turn centre-fed SHA of radius 1.95cm situated 0.4cm above an infinite ground-plane

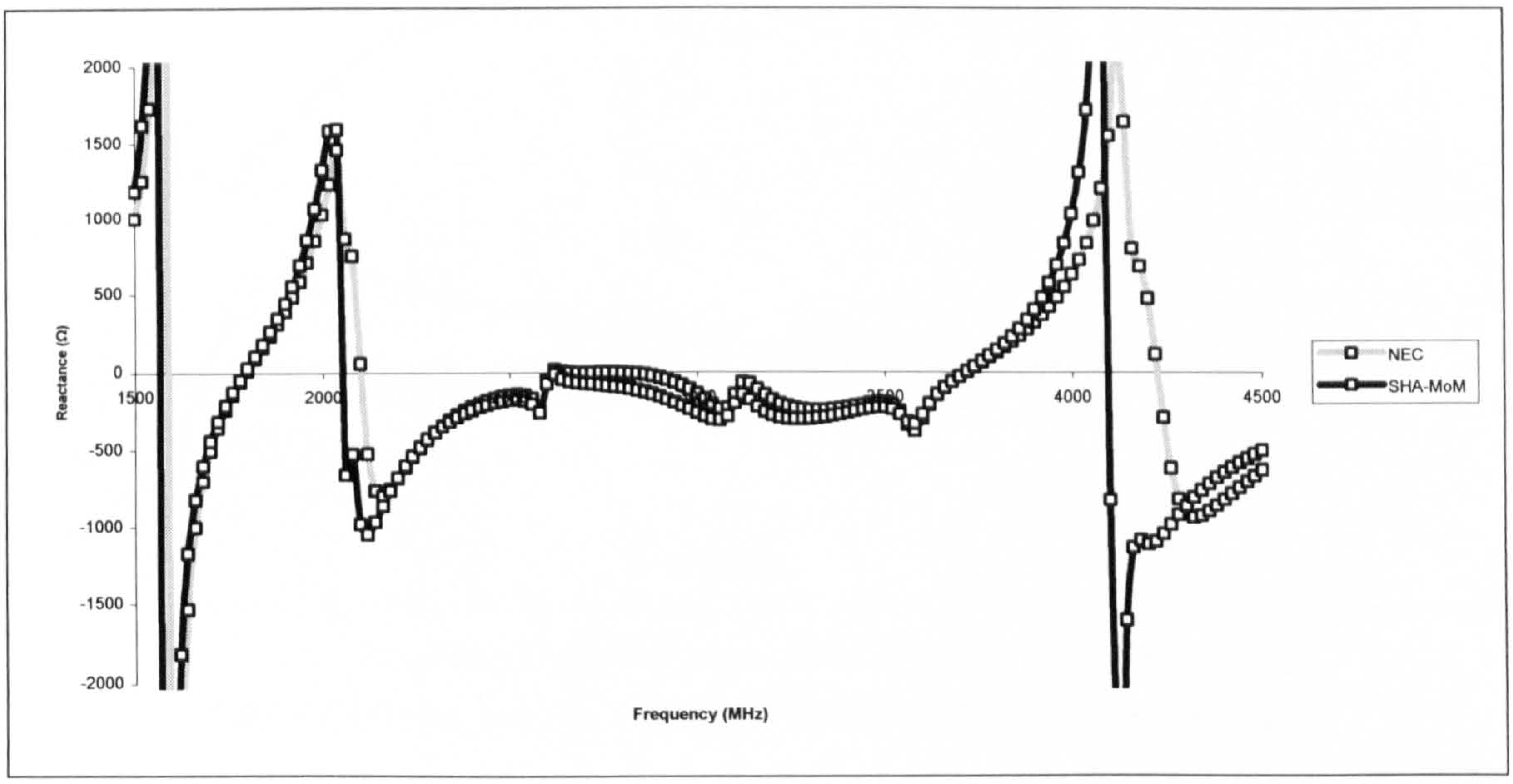

Figure 3.11 – Input reactance against frequency for a 7-turn centre-fed SHA of radius 1.95cm situated 0.4cm above an infinite ground-plane

Again the results with SHA-MoM in Figures 3.10 and 3.11 show good agreement showing that the code has been accurately implemented and is producing reliable results.

3.5 Convergence

An important parameter when implementing the Method of Moments is the number of segments which the structure is decomposed into. This value must be set large enough to allow for accurate representation of the current distribution along the wire and, if linear segments are used, accurate modelling of the geometry itself. For curved antennas such as the SHA it is the latter criterion which dominates. The convergence of both NEC and SHA-MoM was investigated for a number of different SHA geometries, and at various frequencies. One such case, which is representative of all those tested, is given below to demonstrate the advantage of curved segments over linear segments.

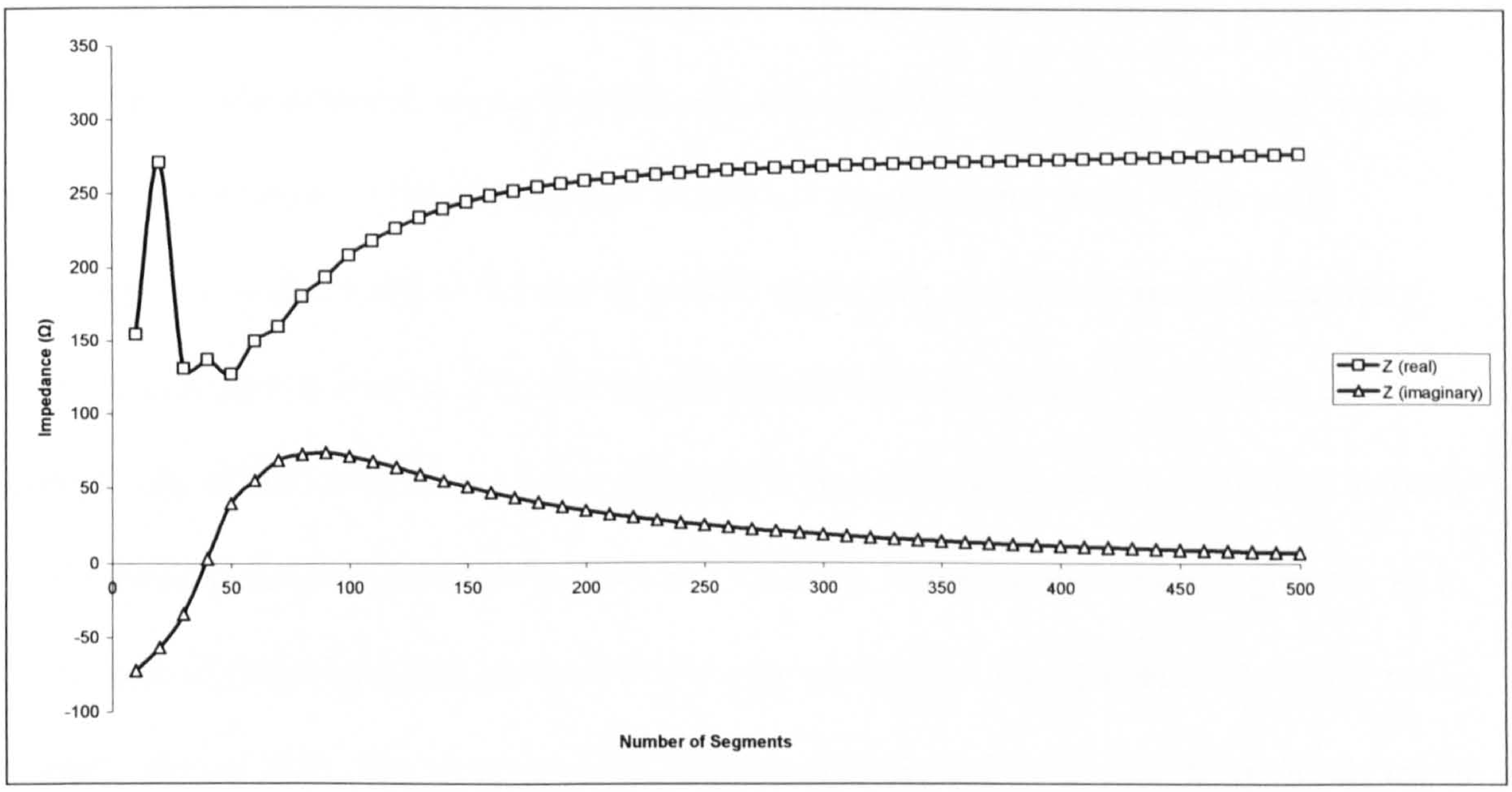

Figure 3.12 – Convergence of NEC (linear segments)
(7-turn CVD type SHA, C = 1.23λ, h = 0.04λ above infinite ground-plane)

Figure 3.12 above shows the convergence of NEC which uses linear segmentation. The graph shows slow convergence with around 400 segments being needed to provide an accurate model. The author's code, SHA-MoM, implements curved segments and a similar convergence plot is given in Figure 3.13.

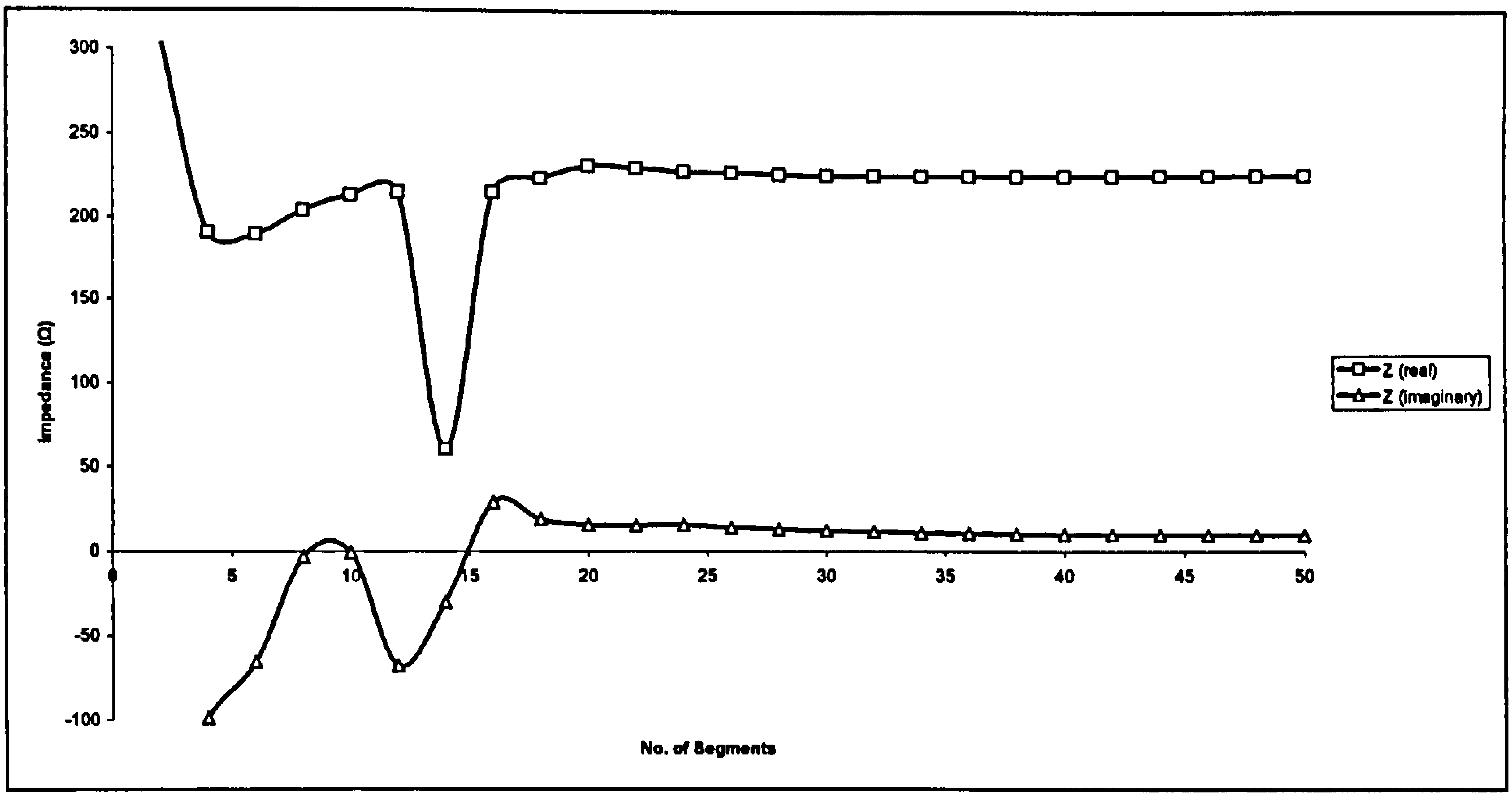

Figure 3.13 – Convergence of SHA-MoM code (curved segments)
(7-turn CVD type SHA, $C = 1.23\lambda$, $h = 0.04\lambda$ above infinite ground-plane)

It is clear from comparing Figures 3.12 and 3.13 that convergence occurs around 20 times faster when curved segments are used, with a good result being obtained with as few as 20 segments. This corresponds to about 3 segments per loop. This rapid convergence is attributed to the use of curved segments, and results in a substantially smaller impedance matrix. The use of curved segments do, however, increase the complexity of the calculations needed to obtain the impedance matrix elements, as both of the nested integrations must be done numerically. When using linear segments, as in NEC, one of these integrations can be solved analytically. As a result SHA-MoM runs slightly slower than NEC, taking perhaps a few minutes per model; NEC typically takes less than one minute per model. It should be noted however that NEC has been optimised for speed, whereas SHA-MoM has not. It is envisaged that the speed of SHA-MoM could be improved to match or better that of NEC.

The oscillations in impedance for small numbers of segments, and in particular the sharp dip in the input resistance value for 14 segments seen in Figure 3.13 are worth commenting on. In order to understand what is happening here, it is necessary to consider the current distribution along the wire, and how this is represented by the Method of Moments. As discussed in Chapter 2, the current is approximated by a series of overlapping basis function, or pulses. The magnitude of each pulse is given by the corresponding element in the current matrix once this has been solved by the MoM.

There are a number of basis functions which can be used, but in this research piecewise sinusoidal functions have been chosen. Each current pulse spans two segments and is described by the expression:-

$$U_n(\ell') = \begin{cases} \dfrac{\sin\beta\left(\ell' - \ell_{n-1}\right)}{\sin\beta\Delta\ell'} & \ell_{\mathrm{n-1}} \le \ell' \le \ell_n \\ \dfrac{\sin\beta\left(\ell_{n+1} - \ell'\right)}{\sin\beta\Delta\ell'} & \ell_{\mathrm{n}} \le \ell' \le \ell_{n+1} \end{cases}$$

where:-

$\Delta\ell'$ is the segment length

$\ell_{\mathrm{n-1}}$ is the position where the first segment being spanned starts

ℓ_{n} is the position where the first segment ends and the second begins

$\ell_{\mathrm{n+1}}$ is the position where the second segment being spanned ends

The shape of this function depends on the segment length being used. Examples of four segment lengths and their corresponding current pulses have been plotted and are given in Figure 3.14.

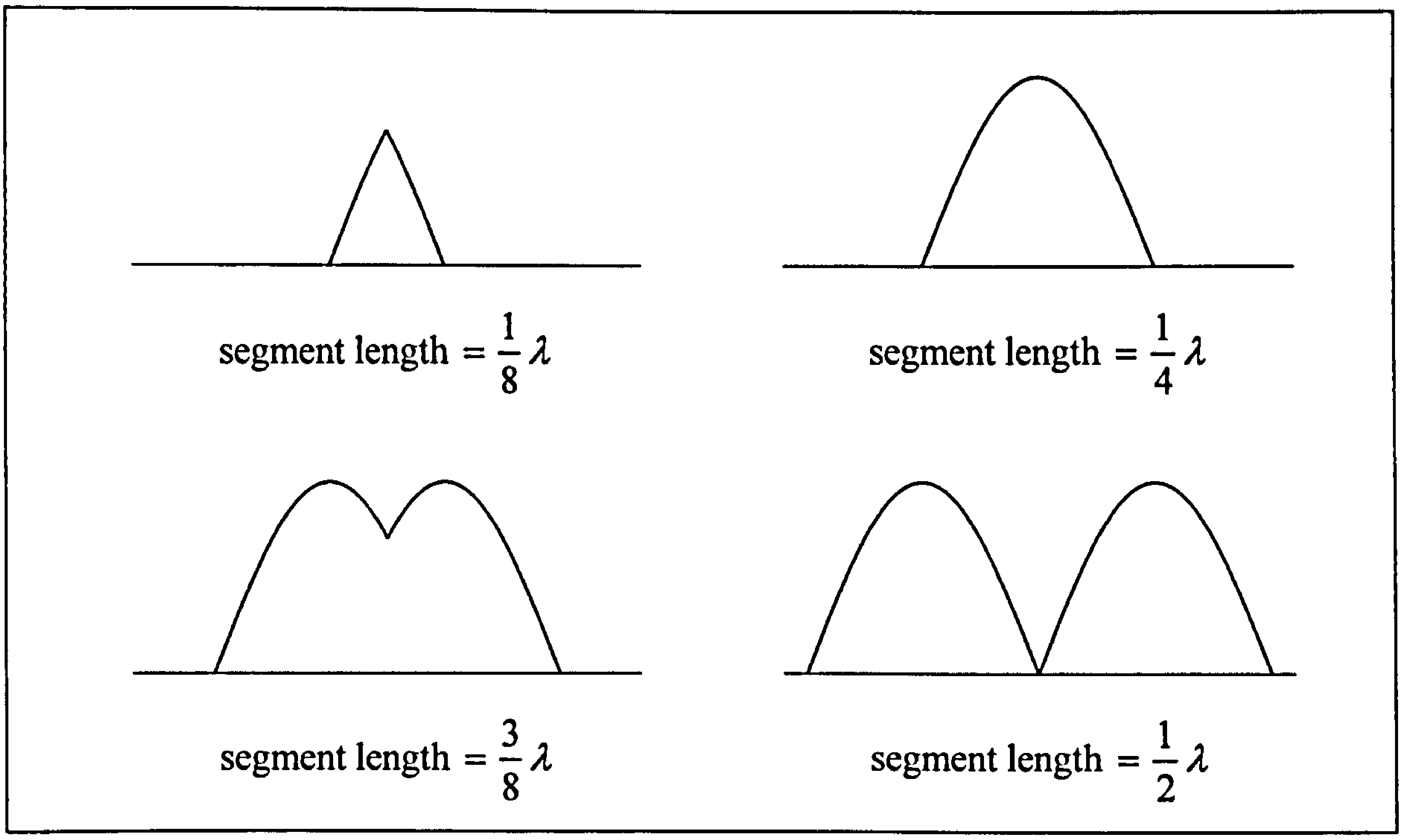

segment length $= \frac{1}{8}\lambda$

segment length $= \frac{1}{4}\lambda$

segment length $= \frac{3}{8}\lambda$

segment length $= \frac{1}{2}\lambda$

Figure 3.14 – Shape of current pulses as determined by the segment length

It can be seen that if the segment length is λ/4 or less, the current pulse contains no dips, but if the segment length is more than λ/4, a dip occurs in the pulse. Figure 3.15 shows the effect of overlapping the current pulses. For both cases three pulses have been shown with the middle of these plotted in bold for clarity. For segment lengths not greater than λ/4 smooth current distribution can be obtained, however if there are dips present this can adversely effect the current distribution. For the special case where the segment length reaches λ/2, the pulses overlap exactly. When this occurs the current is forced to zero at the end of each segment. This is very restrictive to the current distribution and will prevent an accurate solution being obtained.

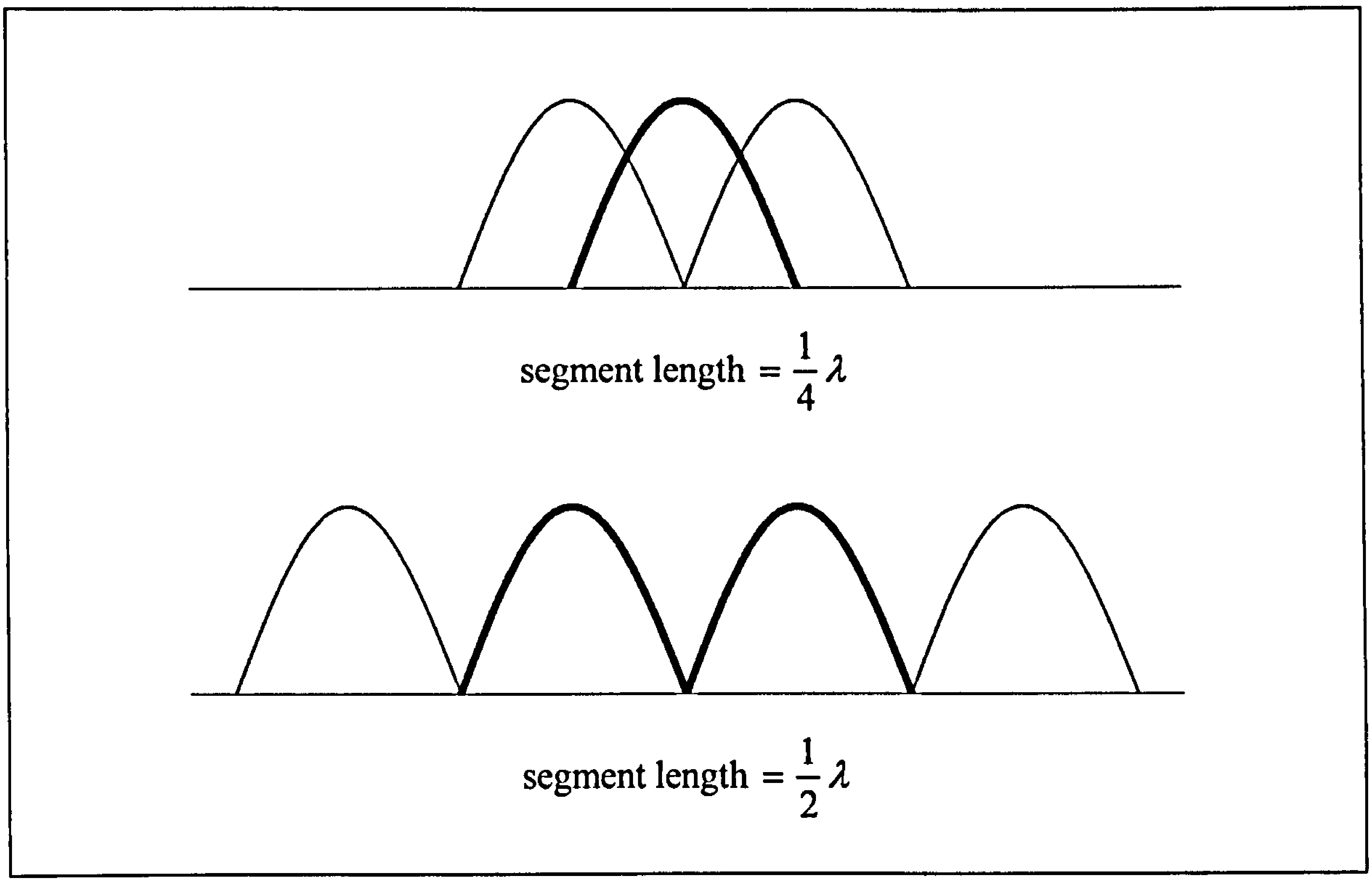

Figure 3.15 – Three overlapping current pulses shown for two different segment lengths

Referring back to Figure 3.13, a sharp dip occurs in the input resistance when 14 segments are used. To calculate the segment length being used we require the total length of the helix which is given by the expression:-

$$\text{Curved length} = a\int_{0}^{2\pi N}\sqrt{\left(1-\psi^{2}\right)+\frac{1}{\left(\pi N\right)^{2}\left(1-\psi^{2}\right)}}\,d\phi$$

For a 7-turn SHA with a circumference of 1.225λ, as used for the converge graph, this gives a curved length of 6.84λ. If this length is then split up into 14 equal segments, each one will have a length of 0.49λ. This is very close to the λ/2 case considered above and will cause the current to be forced to nearly zero at the end of each segment.

3.6 Discussion

Independent MoM code has been written and carefully validated. The code is capable of modelling a number of different geometries including several forms of SHAs and cylindrical helices. These antenna shapes will be investigated using the SHA-MoM code in the next chapter. SHA-MoM can produce a number of different outputs including current distributions, far-field radiation patterns, input impedance characteristics, and gain and axial ratio values.

Output from the SHA-MoM code has been compared with that of NEC, a trusted and popular MoM engine, and with published results from peer reviewed journals. The good agreement obtained has given confidence to the code, allowing it to be used throughout this research.

The convergence of SHA-MoM with an increasing number of segments has also been considered and compared against the convergence of NEC. The SHA-MoM code uses curved segments whereas NEC is limited to approximating geometries with a series of linear segments. It has been shown that by using curved segments, 20 times fewer segments are needed for accurate modelling than are needed if linear segments are employed. This leads to very worthwhile computational savings.

References

1 N. J. Champagne II, J. T. Williams, and D. R. Wilton, "The use of curved segments for numerically modelling thin wire antennas and scatterers", IEEE Trans. Antennas Propagat., vol. 40 (6), pp. 682-689, Jun. 1992.

2 S. K. Khamas, G. G. Cook, and R. J. Waldron, "Moment-method analysis of printed circular wire-loop antenna using curved piecewise sinusoidal subdomain basis and test functions", IEEE Trans. Antennas Propagat., vol. 44 (9), pp. 1303-1305, Sep. 1996.

3 J. C. Cardoso and A. Safaai-Jazi, "Spherical helical antenna with circular polarisation over a broad beam", IEE Electronics Letters, vol. 29 (4), pp. 325-326, Feb. 1993.

4 A. Safaai-Jazi and J. C. Cardoso, "Radiation characteristics of a spherical helical antenna", IEE Proc-Microw. Antennas Propag, vol. 143, pp. 7-12, Feb. 1996.

5 H. T. Hui, K. Y. Chan, E. K. N. Yung, and X. Q. Shing, "Coaxial-feed axial mode hemispherical helical antenna", IEE Electronics Letters, vol. 35 (23), pp. 1982-1983, Nov. 1999.

6 E. Weeratumanoon and A. Safaai-Jazi, "Truncated spherical helical antennas", IEE Electronics Letters, vol. 36 (7), pp. 607-609, Mar. 2000.

7 H. T. Hui, K. Y. Chan, and E. K. N. Yung, "The input impedance and the antenna gain of the spherical helical antenna", IEEE Trans. Antennas Propagat., vol. 49 (8), pp. 1235-1237, Aug. 2001.

8 H. T. Hui, K. Y. Chan, and E. K. N. Yung, "The low-profile hemispherical helical antenna with circular polarization radiation over a wide angular range", IEEE Trans. Antennas Propagat., vol. 51 (6), pp. 1415-1418, Jun. 2003.

9 G. J. Burke and A. J. Poggio, "Numerical Electromagnetics Code (NEC) – Method of Moments," Technical Document 116, Naval Ocean Systems Center, San Diego, California, Jan. 1981.

4 Modelling

4.1 Introduction

This chapter describes how the SHA-MoM code has been used to investigate various spherical helical geometries. Results from the code are presented to illustrate the characteristics of the geometries being investigated. Several modifications to the original SHA are proposed, and the effects these have on the antenna characteristics are shown.

The first modification to be investigated relates to the spacing between adjacent turns. Previous investigations of the SHA [1-7] have all defined a constant vertical separation (CVS) between adjacent turns. In this chapter, a new scheme is proposed and examined in which adjacent turns assume a constant circumferential spacing (CCS).

Also considered are geometries with a non-integer number of turns. Again, this is an area which has not been considered previously in papers relating to the SHA.

A novel balanced twin-arm feed is then proposed. This geometry comprises two hemispherical helical arms which curve around opposite hemispheres. The arms are fed from the centre of the sphere via two linear sections.

Finally, a cylindrical helix is modelled and its characteristics compared with those of the SHA.

4.2 Spacing between turns

As discussed in section 1.4, various methods exist for defining a constant spacing between turns. Figure 4.1 and Figure 4.2 show two such methods, namely Constant Vertical Separation (CVS) and Constant Circumferential Separation (CCS). For both cases a 10-turn SHA is shown.

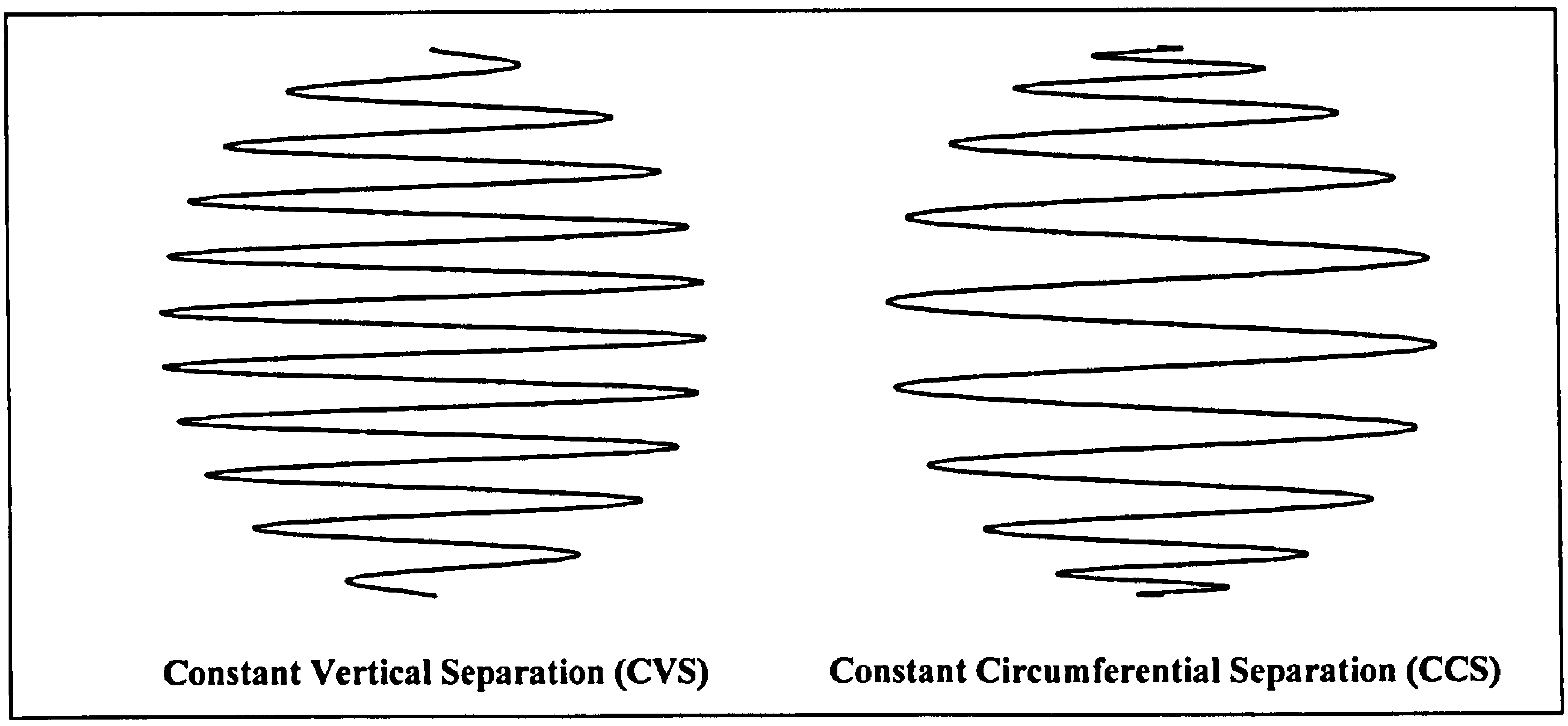

Figure 4.1 – 10-turn SHAs viewed from the side

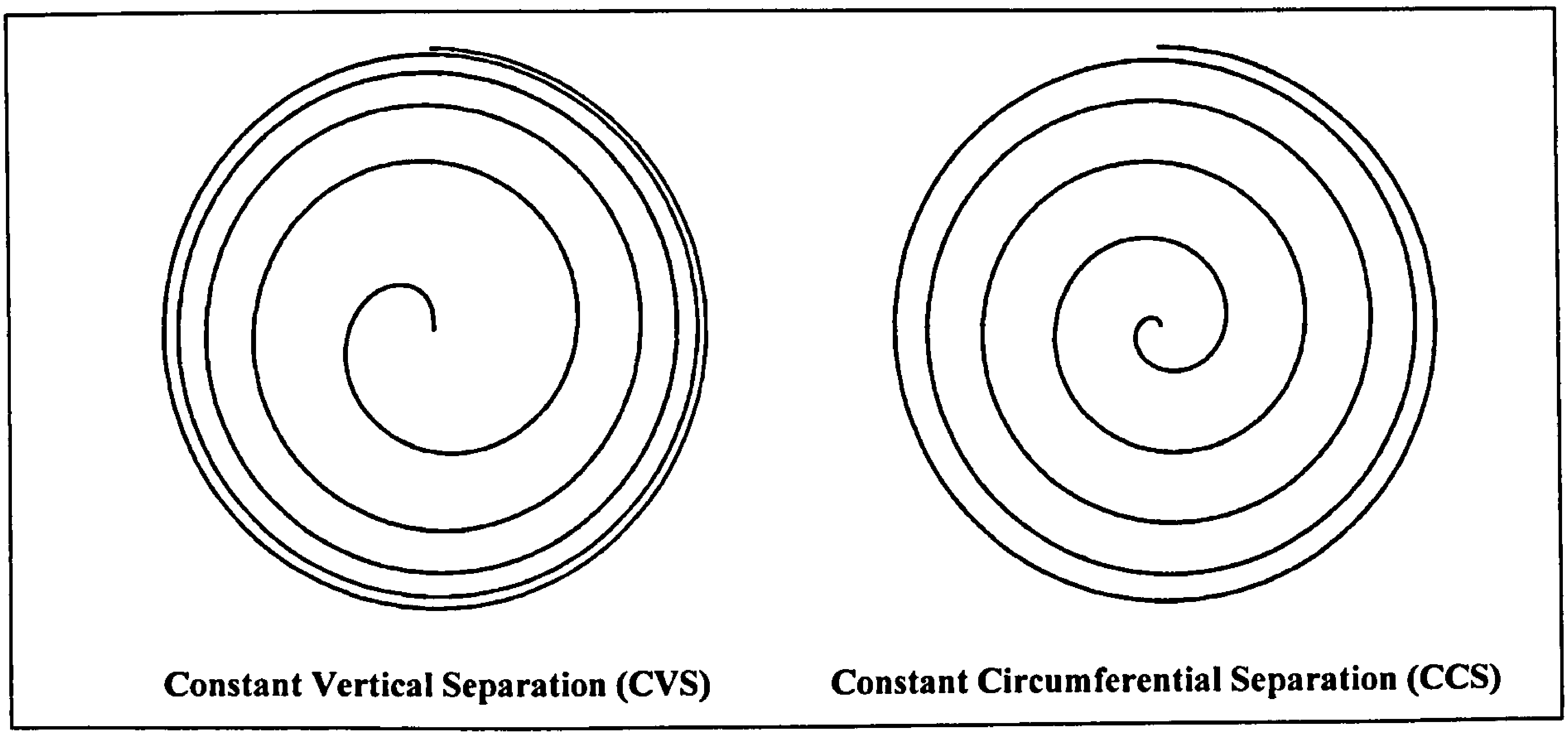

Figure 4.2 – 10-turn SHAs viewed from above (for clarity, only the upper hemisphere is shown)

The papers published on the SHA to date [1-7] all use the CVS geometry and none have mentioned alternatives to this. Given the desire for the antenna to provide a wide beamwidth, it seems logical that the antenna should look as similar as possible when viewed from different angles. A CVS SHA will only appear to have constant separation when viewed from the side, with the top-down view looking the most irregular. The CCS geometry will appear to have turns which are more regularly spaced when viewed from both the side and the top, and thus provides the best compromise for invariance due to viewing angle.

The two geometry types have been modelled using the SHA-MoM code for the case of 3-turn antennas, and the axial ratio on boresight characteristics are given in Figure 4.3.

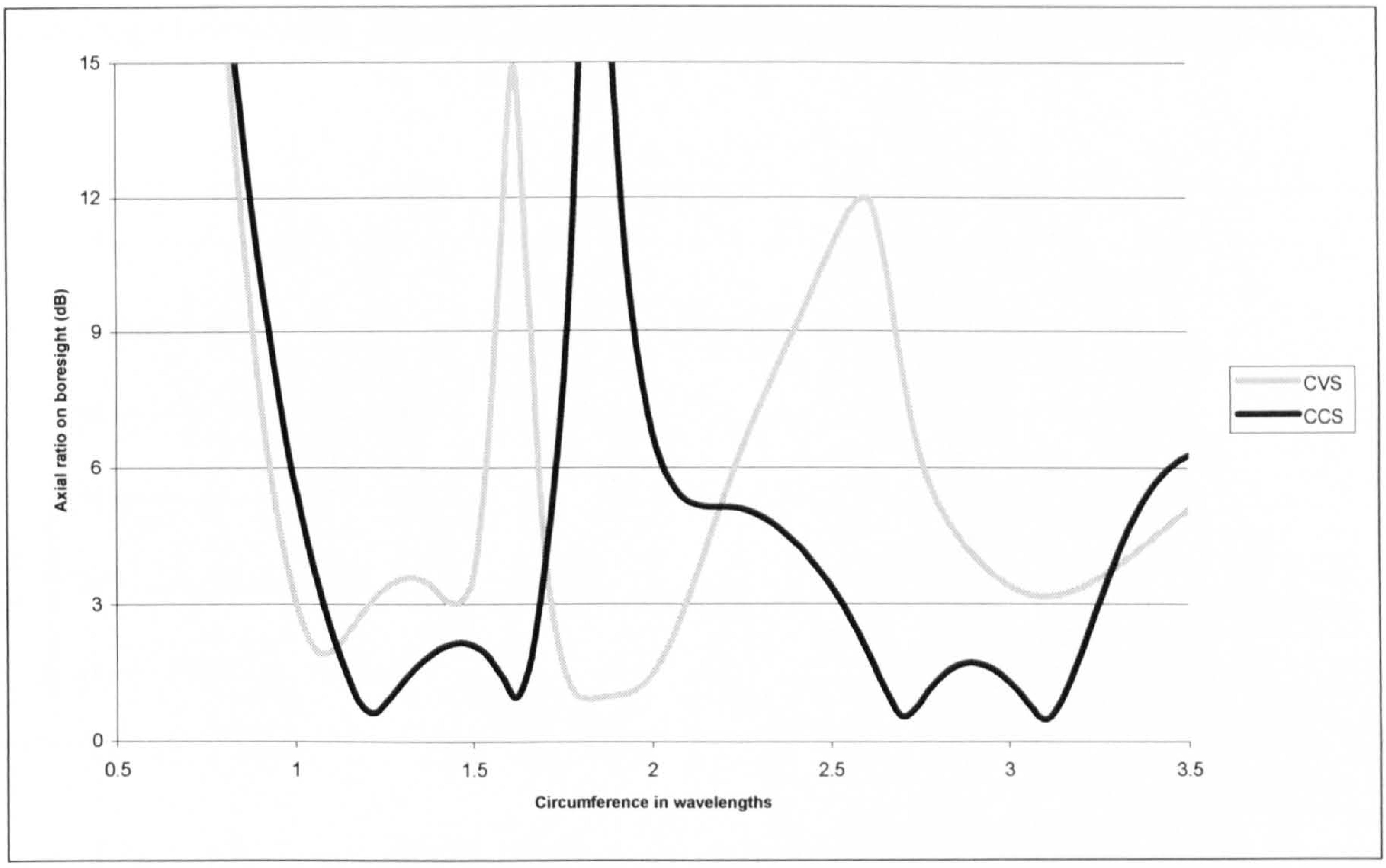

Figure 4.3 – Axial ratio on boresight for 3-turn CVS and CCS geometries

Figure 4.3 clearly shows that over the majority of the range, the axial ratio in the boresight direction is lower for the CCS geometry than for the CVS scheme. This agrees with the prediction above, and confirms the usefulness of the CCS geometry proposed here.

An axial ratio of 0dB indicates pure circular polarisation; anything higher than this technically shows elliptical polarisation with linear polarisation being indicated by an infinite axial ratio. It is generally considered [8] that an axial ratio of less than 3dB indicates acceptable circular polarisation. Using this criterion it is possible to define a beamwidth over which reasonable CP is produced. This can be termed the axial ratio beamwidth.

Figure 4.4 shows the axial ratio beamwidths for the 3-turn geometries currently under consideration. The graphs are discontinuous as a beamwidth is only defined if the axial ratio drops below 3dB; Figure 4.3 showed that this is not the case for all frequencies.

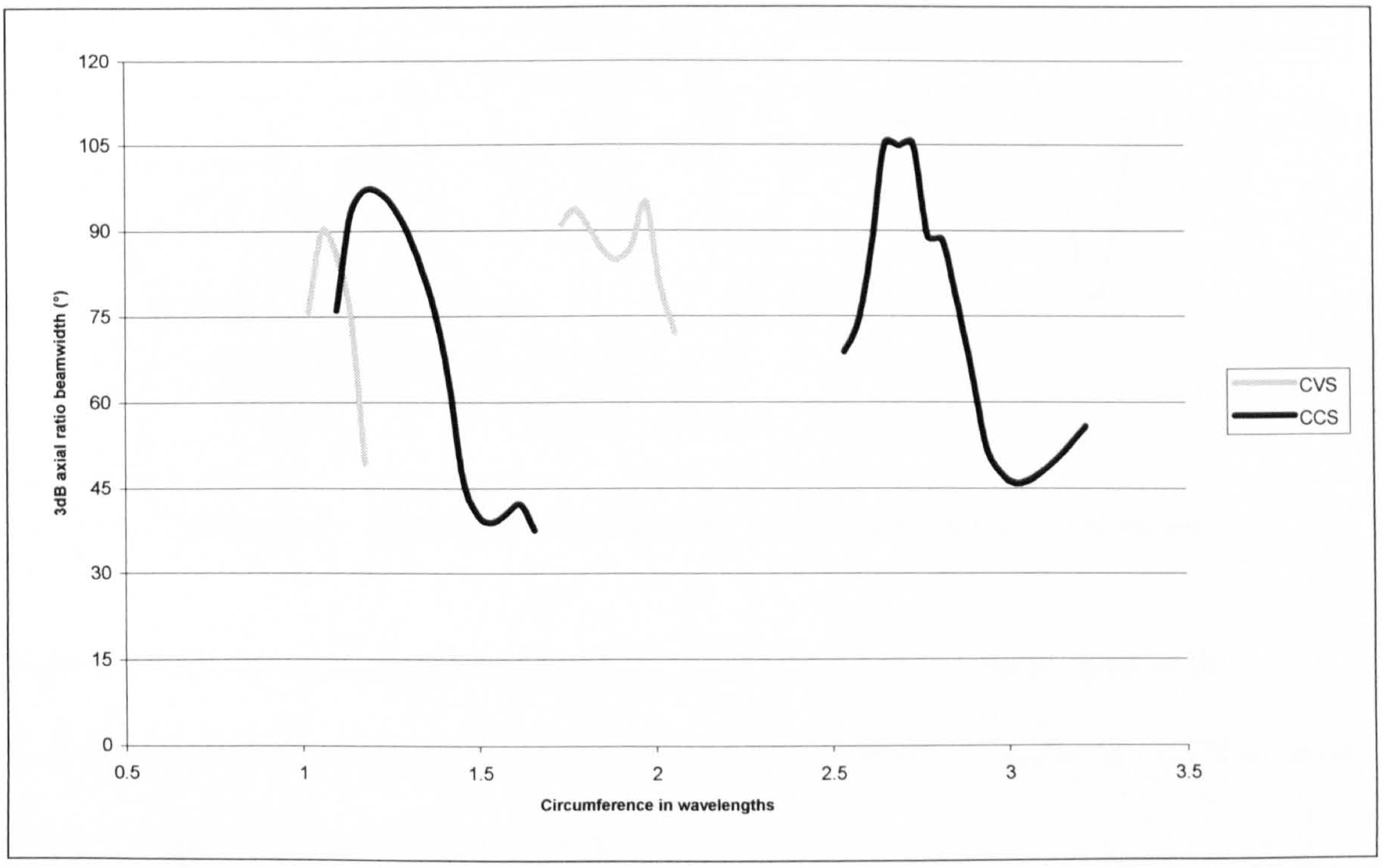

Figure 4.4 – Axial ratio beamwidth for 3-turn CVS and CCS geometries

From Figure 4.4 it is clear that for 3-turn antennas the CCS geometry produces both larger 3dB beamwidths than the CVS geometry, and also maintains these beamwidths over wider frequency ranges. For example, the CCS geometry maintains an AR beamwidth of 75° over a 23% bandwidth, compared with 11% for the CVS antenna. At a slightly higher frequency, the CCS geometry maintains a 90° AR beamwidth over a 6% bandwidth.

Looking at antennas with a few more turns, Figure 4.5 considers the axial ratio values for 7-turn antennas, again comparing the CVS and CCS geometry types.

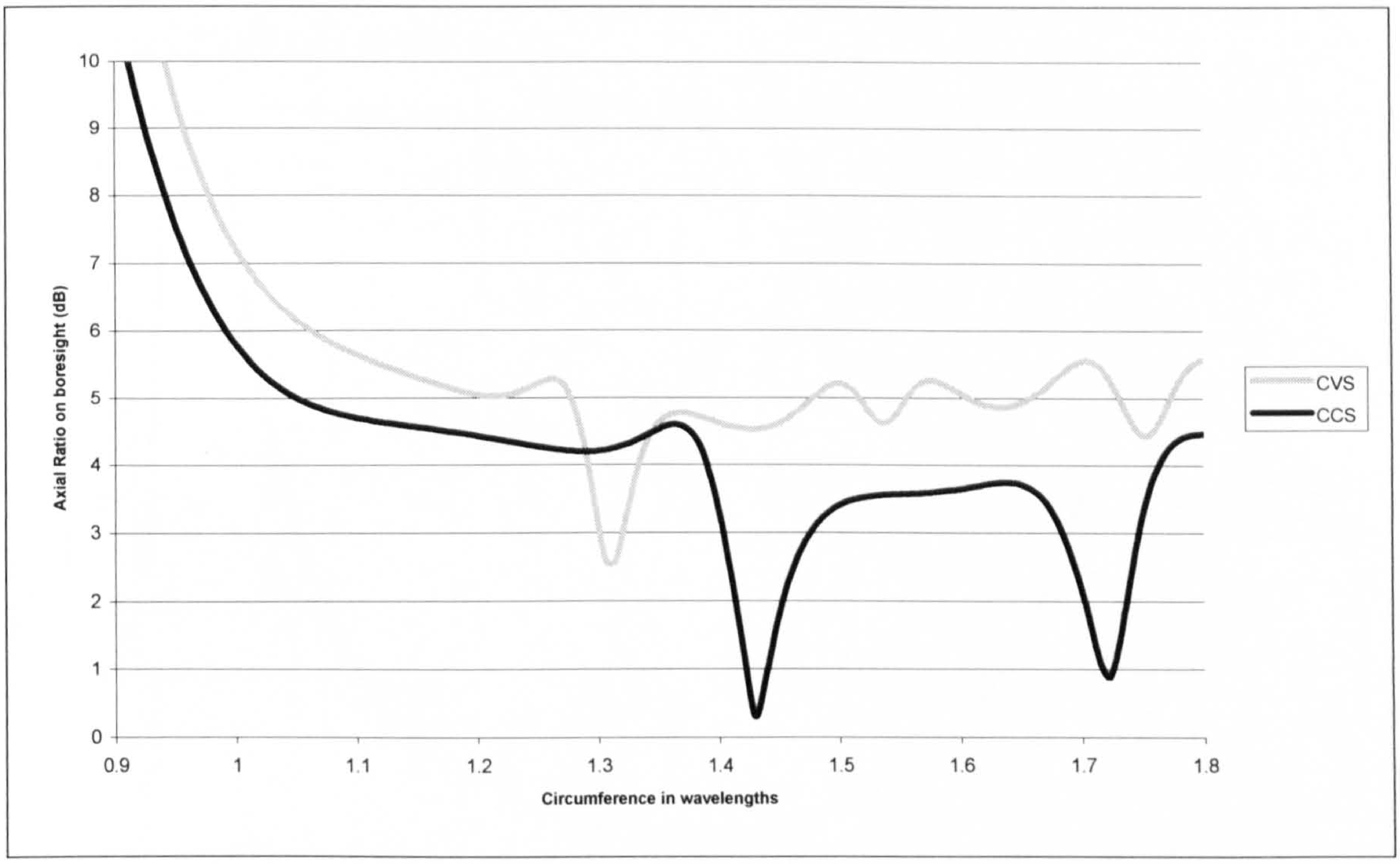

Figure 4.5 – Axial ratio on boresight for 7-turn CVS and CCS geometries

Figure 4.5 shows again that over the majority of the range, the axial ratio in the boresight direction is noticeably lower for the CCS geometry than for the CVS scheme. The axial ratio response is also smoother for CCS.

Although only 3-turn and 7-turn results are presented here, several antennas with turns ranging from 2 to 10 have been investigated with the CCS geometries showing similar improvements in the axial ratio and axial ratio beamwidth irrespective of number of turns.

Figure 4.6 shows how axial ratio varies with theta for the two geometries. Frequencies were chosen to coincide with the minimum values of axial ratio shown in Figure 4.5. These correspond to a 7-turn CVS antenna with a circumference of 1.31λ, and a 7-turn CCS antenna with a circumference of 1.43λ. The CCS antenna is seen to give lower axial ratio values over the majority of the angular range, showing that it is better at providing CP off-axis as well as on.

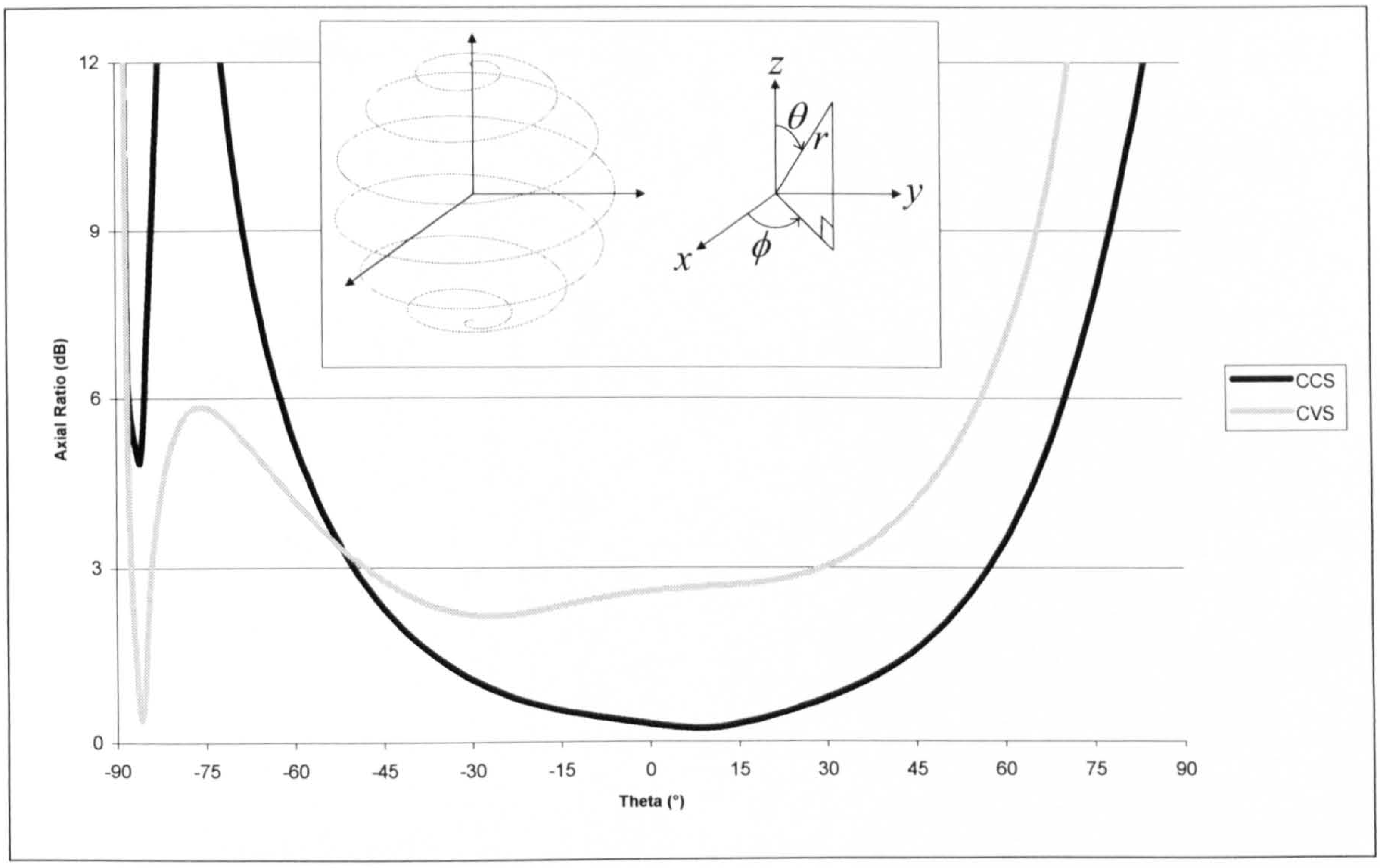

Figure 4.6 – Axial ratio in the $\phi = 0°$ elevation plane for 7-turn CVS and CCS geometries

From Figure 4.6 the AR beamwidths for the CVS and CCS geometries are 78° and 107° respectively. Clearly at the frequencies chosen, the CCS geometry provides CP over a wider angular range.

For pure circular polarisation the E_θ and E_θ components must be equal in magnitude and must have a 90° phase difference. Figure 4.7 and Figure 4.9 show that the field components in and around the boresight direction are almost equal for both geometries. However, Figure 4.8 shows a phase difference of 105° whereas Figure 4.10 shows a phase difference of 90°. This is the reason that the axial ratio is lower for the CCS.

Whether E_θ leads or lags E_θ determines the sense of the polarisation; either right-hand circular polarisation (RHCP) or left-hand circular polarisation (LHCP). Figure 4.8 shows that for the CVS antenna the phase difference switches polarity near the $\theta = 90°$ direction. This also occurs for the CCS antenna in Figure 4.10 but near the $\theta = -90°$ direction. This indicates that the sense of the polarisation can be reversed near to the equator of the antenna.

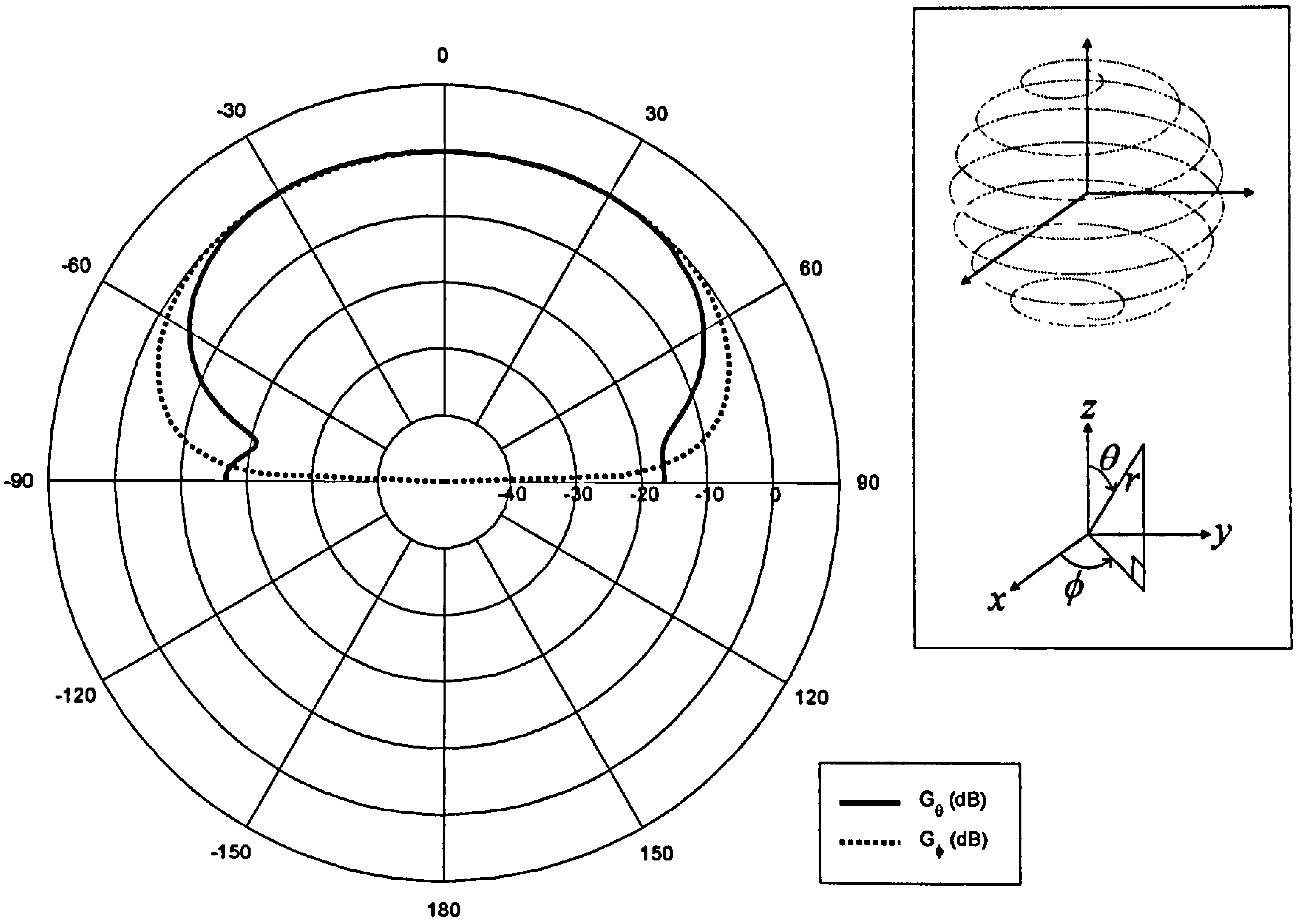

Figure 4.7 – Radiation pattern for a 7-turn CVS SHA with C=1.31λ, $\phi = 0°$, $-180° < \theta < 180°$

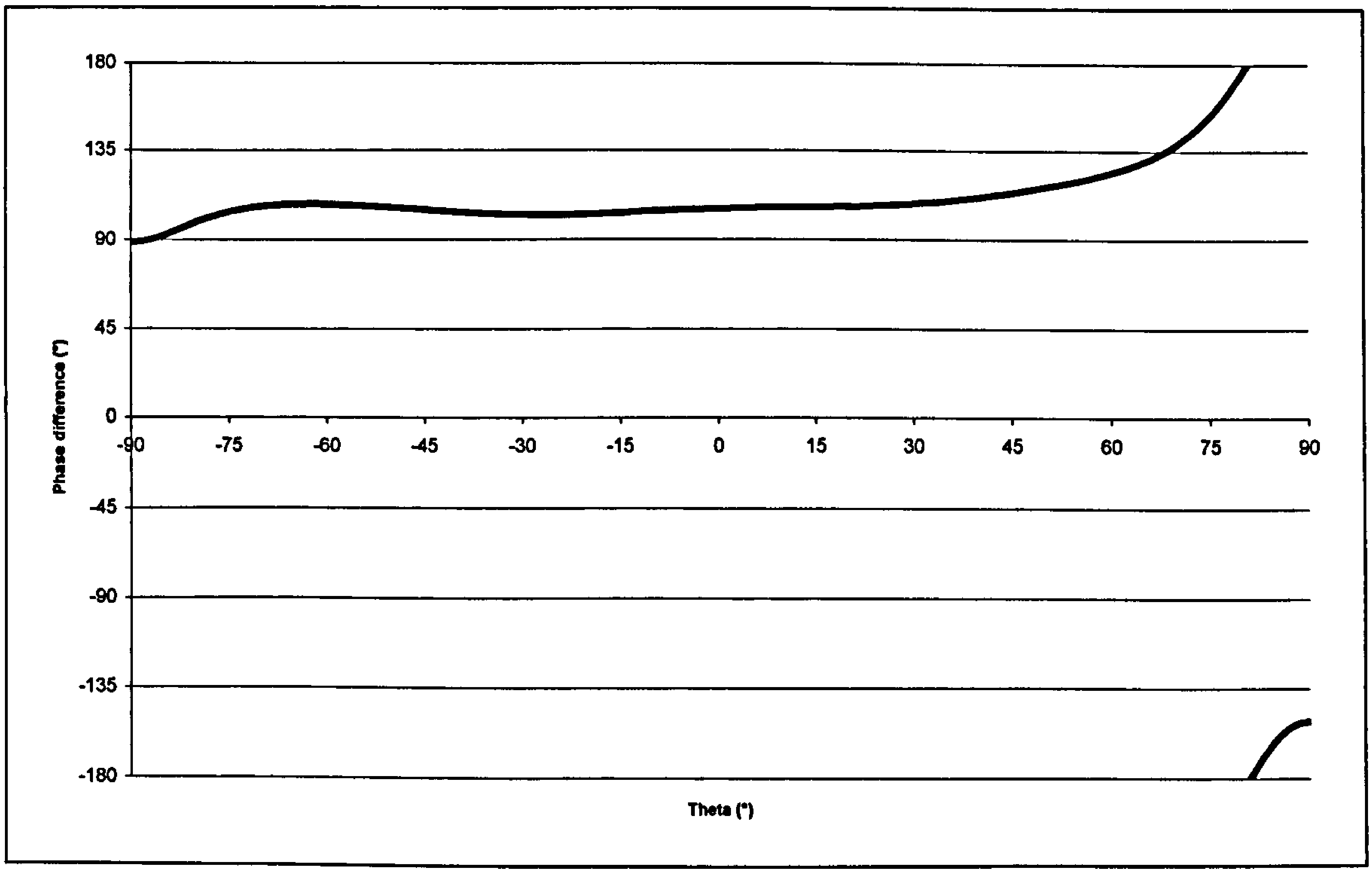

Figure 4.8 – Phase difference between E_θ and E_ϕ for a 7-turn CVS SHA with C=1.31λ, $\phi = 0°$

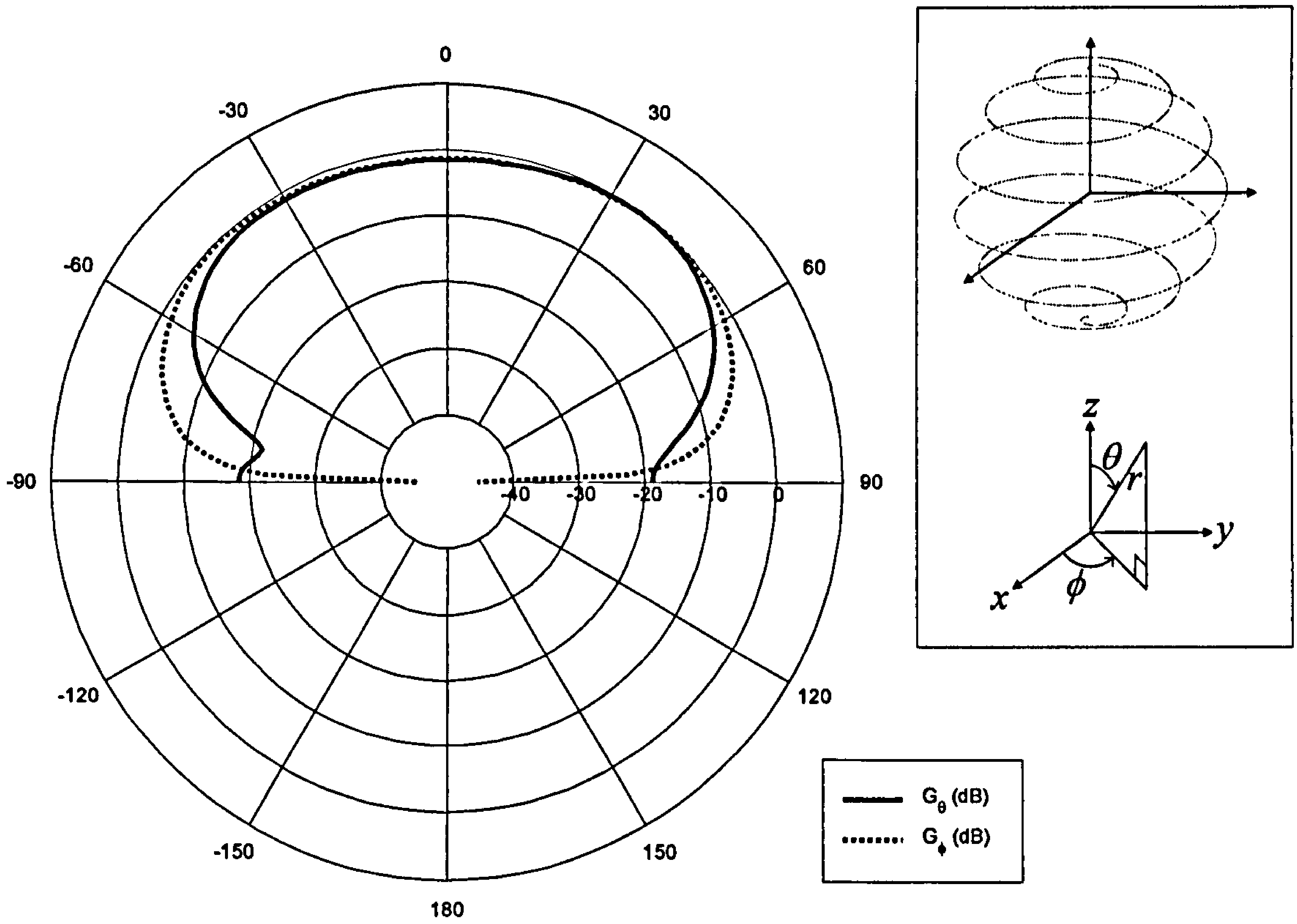

Figure 4.9 – Radiation pattern for a 7-turn CCS SHA with C=1.43λ, $\phi = 0°$, $-180° < \theta < 180°$

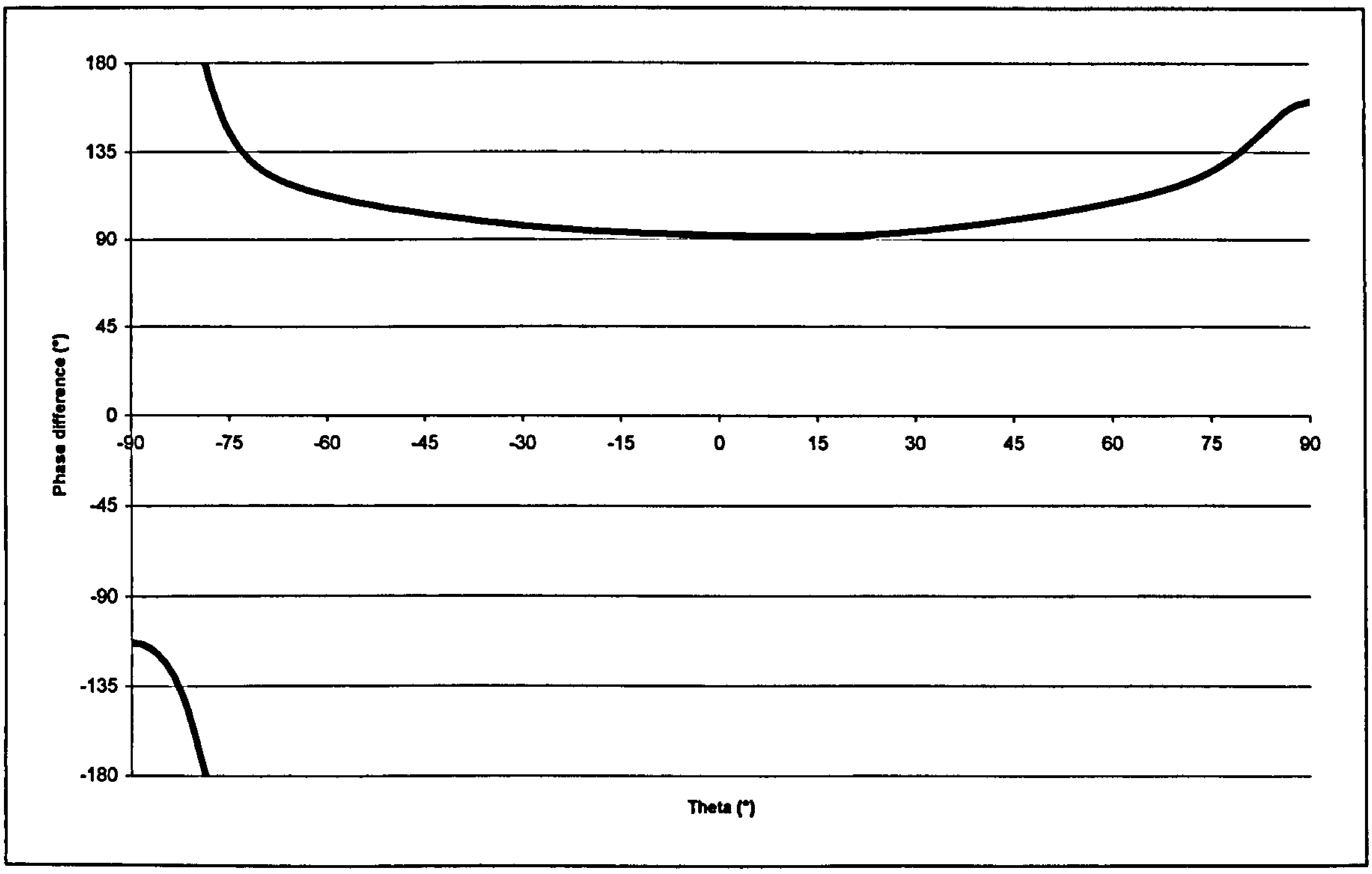

Figure 4.10 – Phase difference between E_θ and E_ϕ for a 7-turn CCS SHA with C=1.43λ, $\phi = 0°$

In addition to the radiation and polarisation properties considered so far, the input characteristics of the antenna are also important as these determine the impedance bandwidth of the antenna. Figures 4.11 and 4.12 show how the input impedance varies with frequency for 3-turn and 7-turn CVS and CCS geometries.

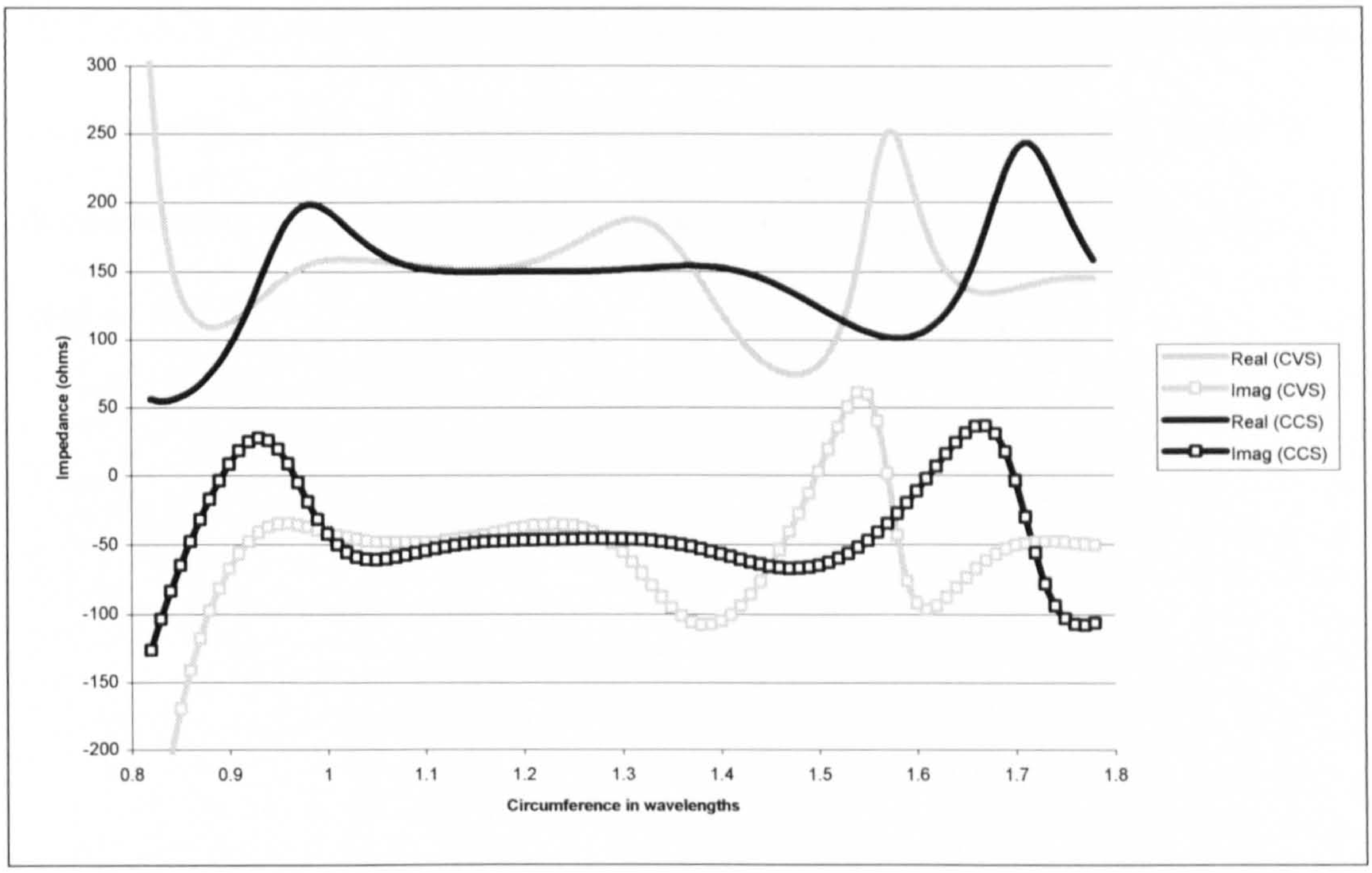

Figure 4.11 – Impedance characteristics of 3-turn CVS and CCS geometries

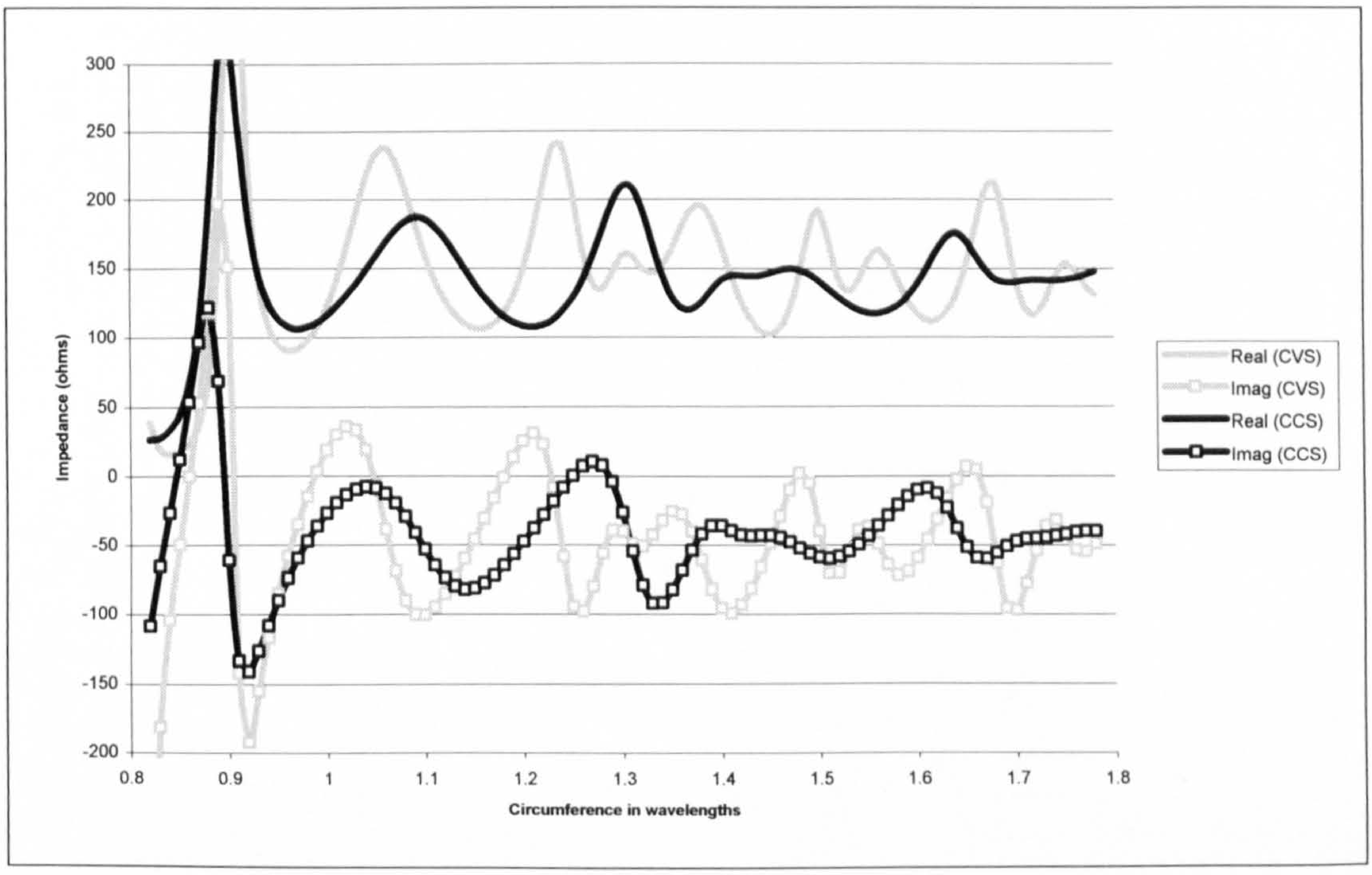

Figure 4.12 – Impedance characteristics of 7-turn CVS and CCS geometries

It can be seen in Figures 4.11 and 4.12 that the input impedance for the CCS geometry is smoother over the frequency range with fewer oscillations. This would allow the antenna to be matched over a wider bandwidth.

Whilst the CCS scheme of spacing proposed here does not offer increased performance at all frequencies, it does so over a considerable proportion of them. It is certainly worth considering therefore as a replacement to the CVS scheme which has been reported so far.

4.3 Non-integer number of turns

To date, the literature on Spherical Helical Antennas [1-7] has only considered geometries with an integer number of turns. This makes the discussions simpler but is unnecessarily restrictive; geometries can certainly exist with a non-integer number of turns – it simply means that the wire reaches the upper pole of the sphere at an arbitrary angle, instead of a fixed one. Figure 4.13 shows this effect by considering a number of geometries with non-integer numbers of turns.

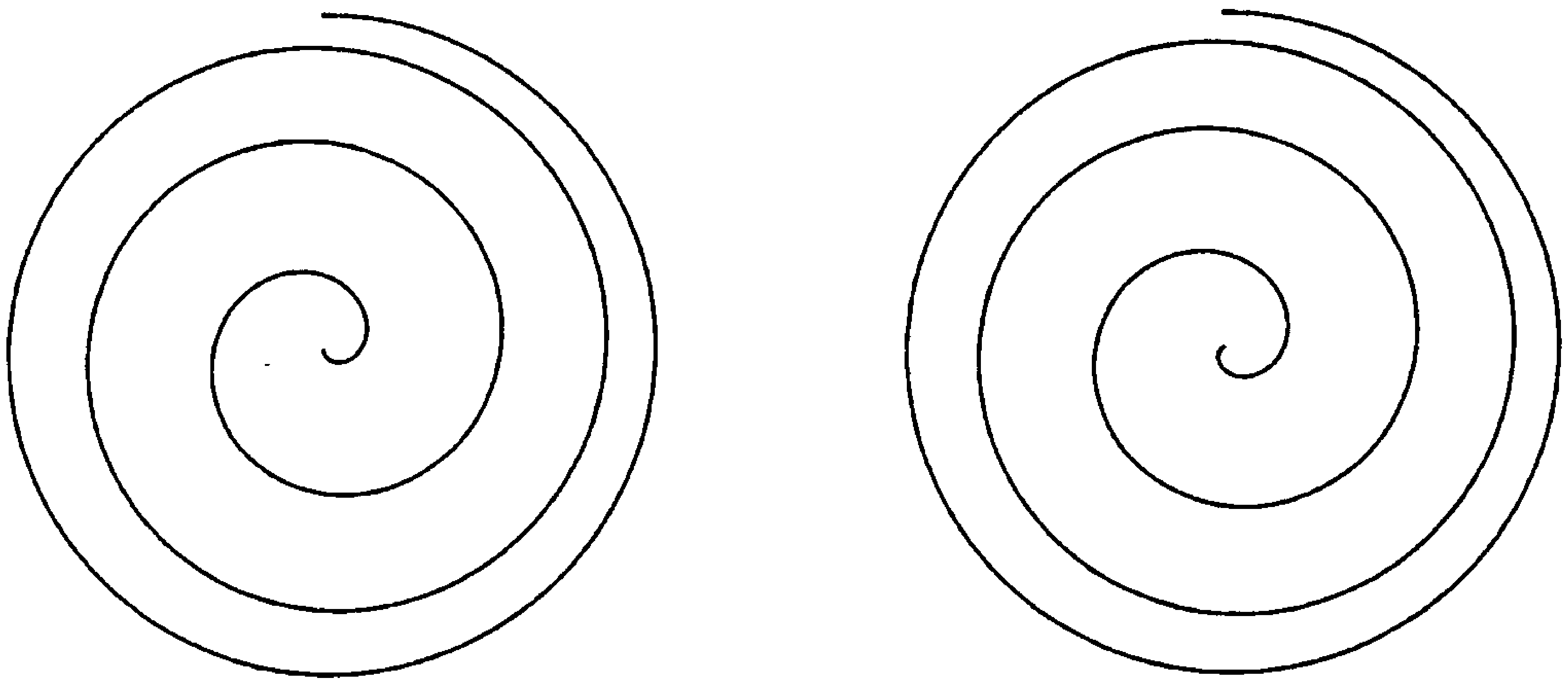

7-turn CCS **7.33-turn CCS**

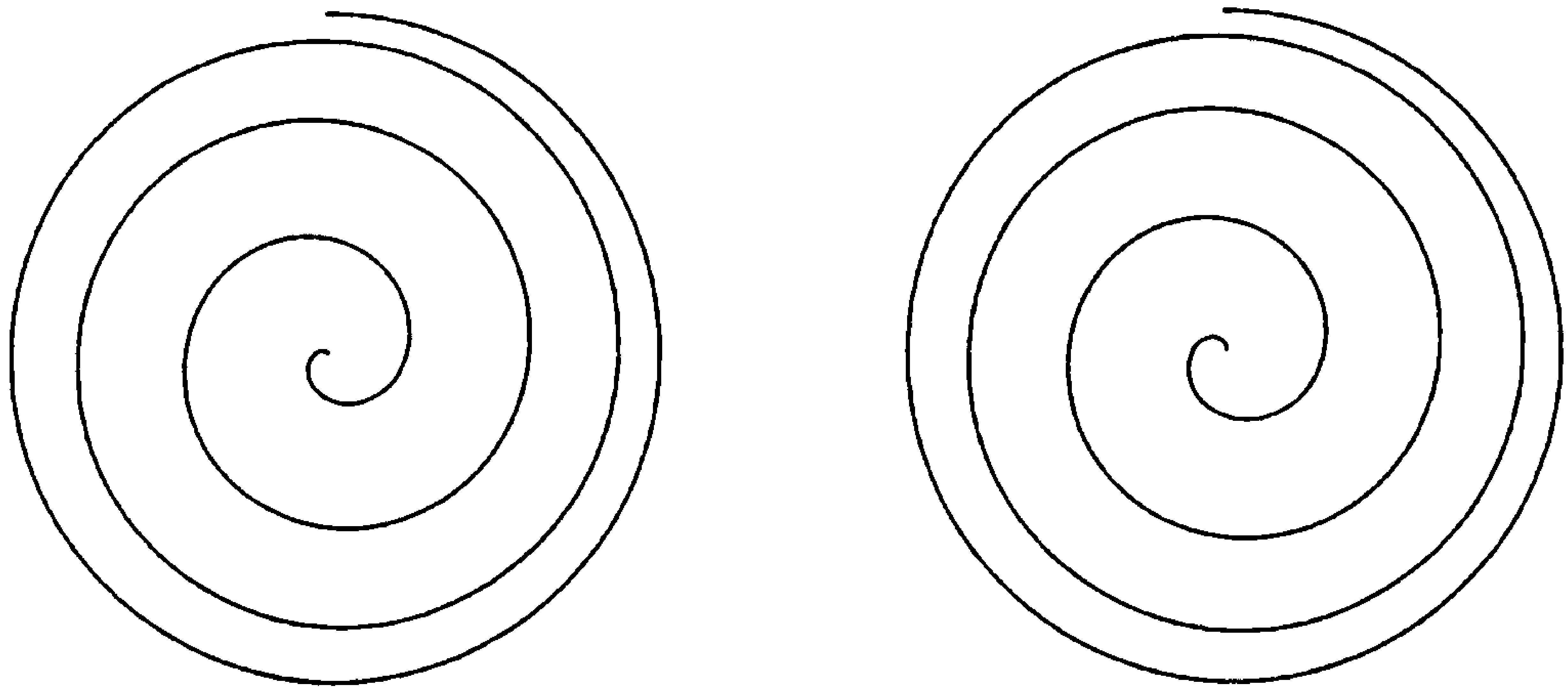

7.67-turn CCS **8-turn CCS**

Figure 4.13 – SHA geometries with varying, non-integer, numbers of turns

(for clarity, only the upper hemispheres are shown)

Adhering to the unnecessary restriction of integer turns may lead to an antenna with useful characteristics being overlooked. This will be particularly relevant when optimising the antenna as it is desirable to maximise the search space.

By considering various examples, it was found that useful properties were indeed obtained for antennas with a non-integer number of turns. Figure 4.14 shows the axial ratio for an SHA with CVS spacing and a circumference of 1.125λ as the number of turns is increased from 2 to 3.

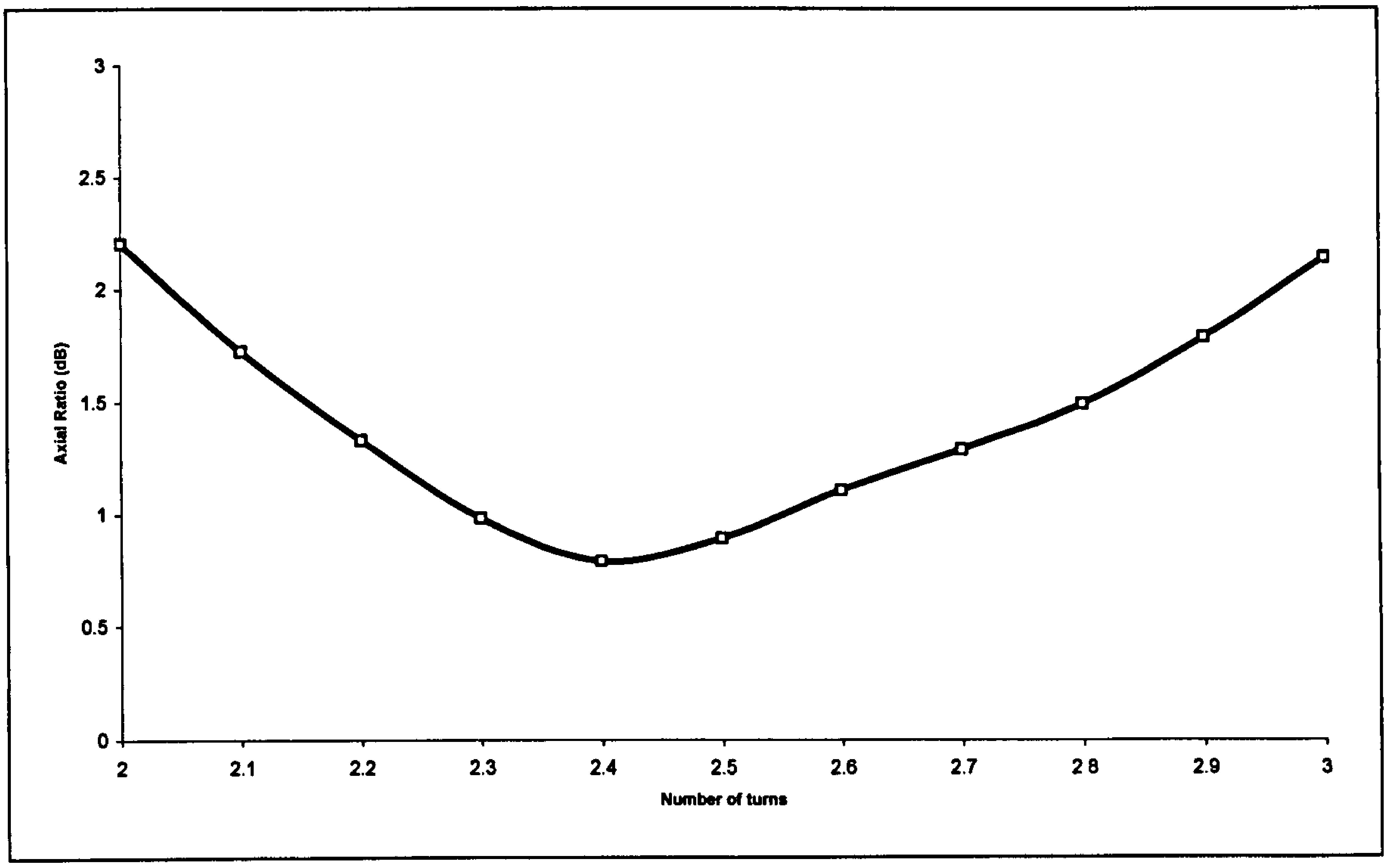

Figure 4.14 – Axial ratio in boresight direction for CVS SHA with C=1.125λ

Clearly it can be seen from Figure 4.14 that the best axial ratio is obtained between the two integer number of turns. If the number of turns had been restricted to integer values this geometry would have been overlooked.

4.4 Twin-arm geometry with CCS

The twin-arm geometry, introduced in section 1.4, and shown again in Figure 4.15 modifies the SHA into a balanced antenna. Balanced antennas can operate without a ground plane and thus offer the advantages of compactness and resilience to detuning effects caused when objects are brought into the close proximity of the antenna. The twin-arm antenna proposed here uses the CCS scheme of spacing between turns, as this was found to give better CP performance in section 4.2.

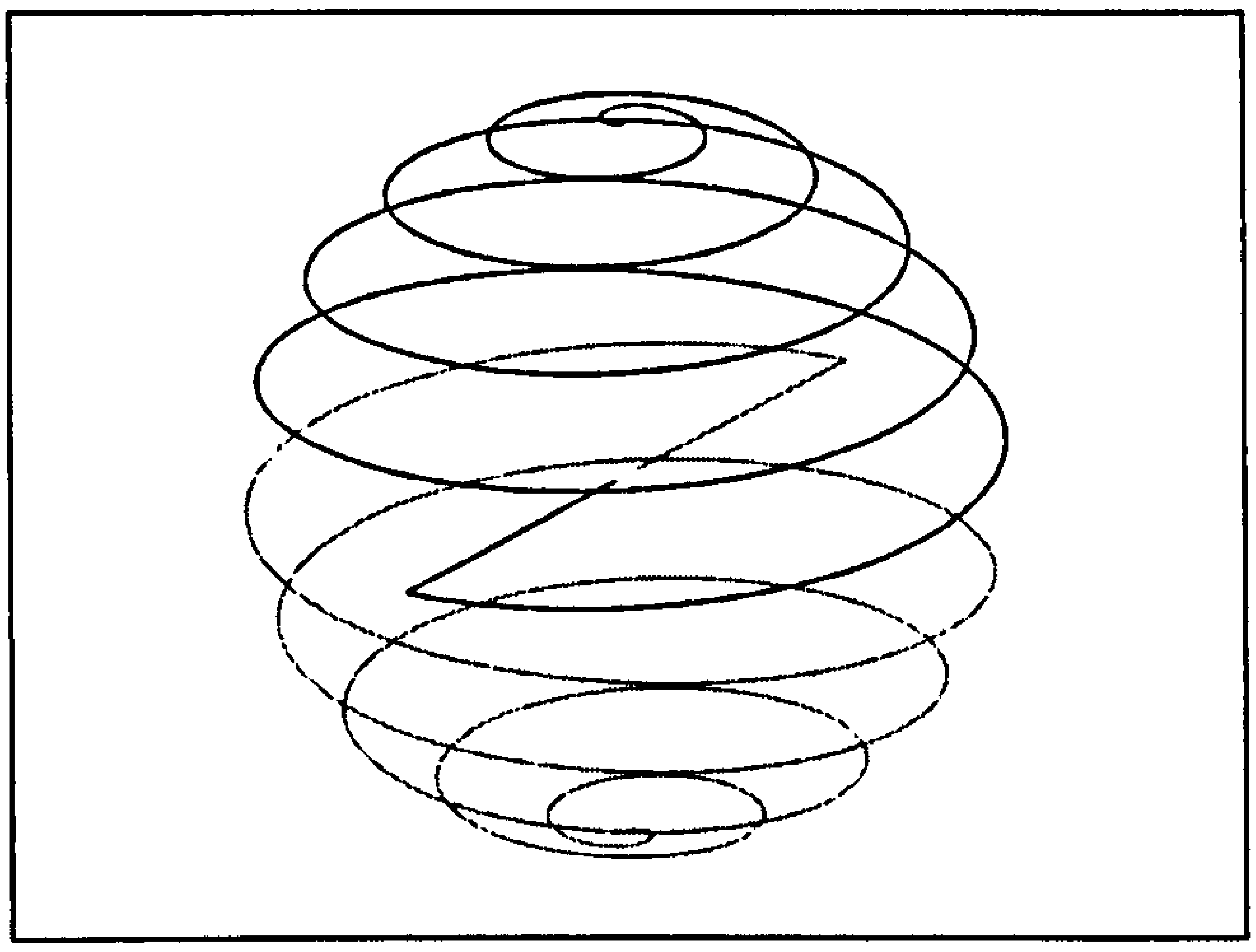

Figure 4.15 – Centre-fed Spherical Helical Antenna

The twin-arm geometry consists of two hemispherical helical arms which are positioned back-to-back, pointing in opposite directions. Each of these arms is fed via a linear section originating at the centre of the sphere. In previous work Chan et al. [9] had fed a hemispherical antenna mounted above a ground plane with a similar linear section from the centre, as was shown in Figure 1.1. The twin-arm geometry proposed here is effectively the combination of two such antennas to form a balanced structure, and remove the need for a ground plane. The twin-arm geometry is therefore novel to this research.

Analysis of the twin-arm geometry with SHA-MoM has shown a strong similarity between this antenna and the conventional SHA. Many of the characteristics of the more usual SHA are repeated, and in particular, the modified geometry is still capable of providing circularly polarised radiation over a wide beamwidth. Antennas with 2-, 3-, 5-, 7-, and 10- turns have been considered. For brevity, only results for 3-turn geometries are presented in this section. Any differences between the characteristics shown, and those of antennas with different numbers of turns will be discussed in the text.

In general, values for axial ratio are slightly worsened, which is thought to be due to the presence of the linear sections which feed the helical arms. The gain of the antenna is also decreased due to the absence of a ground plane, which would otherwise help reflect any back radiation. However, the lack of a ground plane also results in an increase in the beamwidth of the antenna.

Figure 4.16 shows how the axial ratio on boresight varies with frequency for both the twin-arm and conventional SHA. Although the axial ratio values are in general higher for the twin-arm geometry, indicating poorer CP, the modified geometry still provides CP at some frequencies.

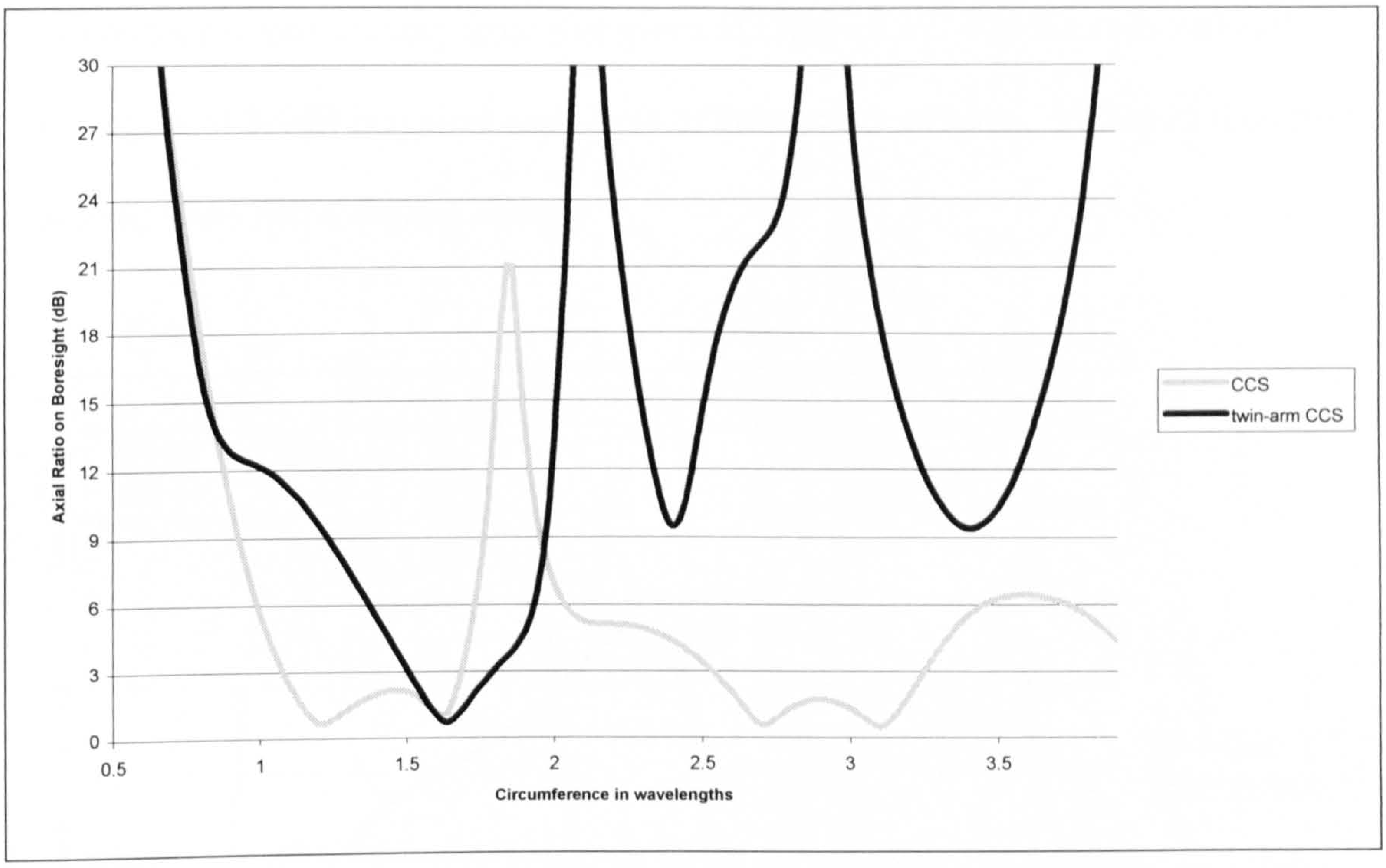

Figure 4.16 – Axial ratio on boresight for 3-turn twin-arm and conventional SHA geometries

Considering antennas with other numbers of turns, it has been found that twin-arm antennas with 2-, 3-, and 10- turns did produce regions of CP, whereas 5- and 7- turn antennas did not. The axial ratio characteristics also vary more considerably when altering the number of turns, than they do for the conventional SHA.

Figure 4.17 shows the gain in the boresight direction for the conventional and twin-arm geometries. The gain of the twin-arm SHA varies between about 2dB and 6dB and is lower than the gain of 8-10dB achieved by the single-wire SHA. For twin-arm geometries with 2-, 5-, 7-, and 10- turns the gain also fluctuates between 2-6dB, though the frequency responses vary from that given in Figure 4.17. For the conventional SHA, a gain of 8-9dB is typical regardless of the number of turns. This gain then rises to around 10dB before falling sharply.

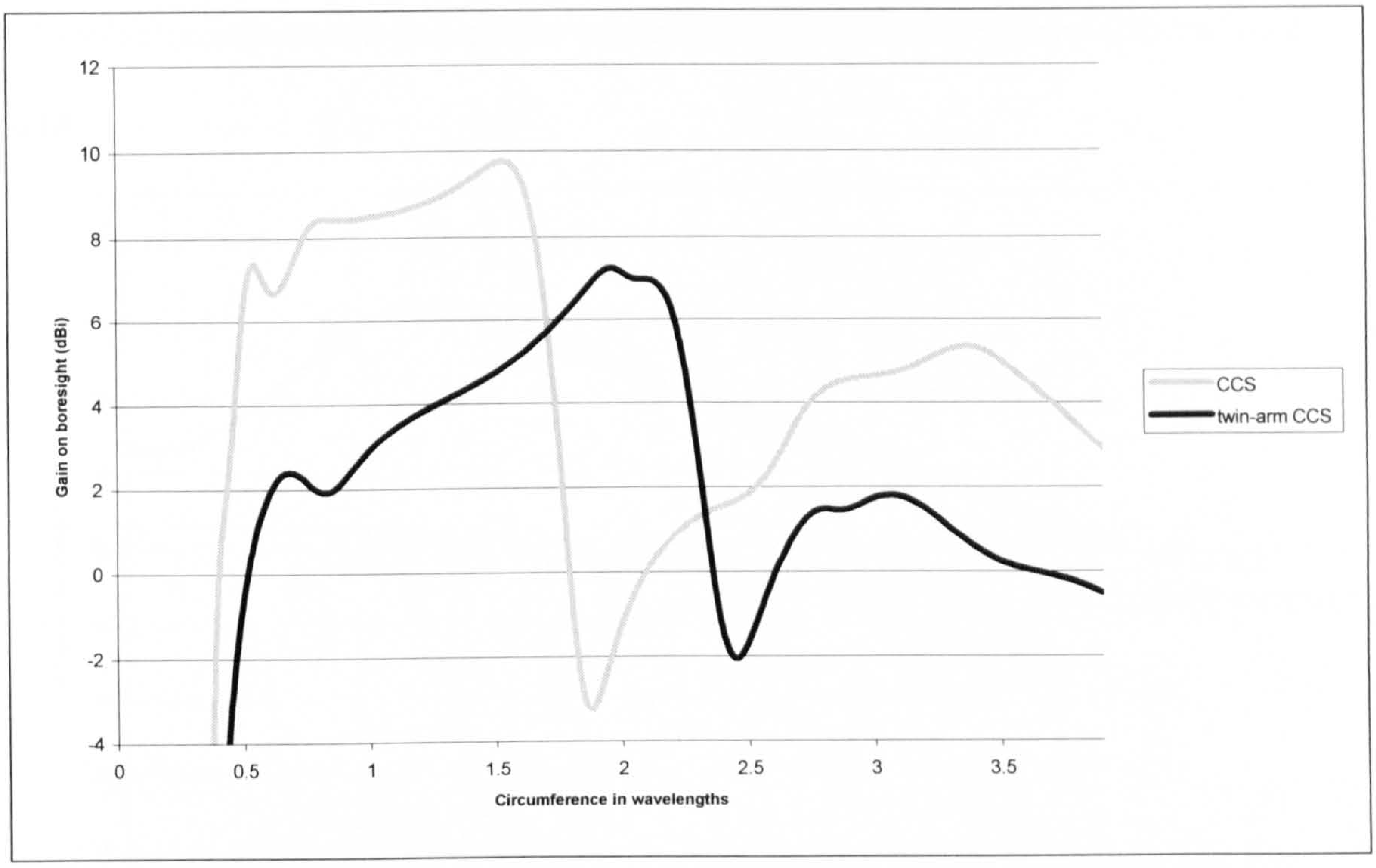

Figure 4.17 – Gain on boresight for 3-turn twin-arm and conventional SHA geometries

The reason the gain drops sharply for the single-wire SHA is due to the current distribution on the wire [2]. If the circumference of the SHA is 2λ then for turns near the equator the currents at opposite sides of the turn are in-phase, however the direction of the helix is 180° reversed so the far-field patterns produced by the two points interfere destructively in the boresight direction. The additional interference of turns away from the equator means that this phenomenon occurs for circumferences just under 2λ, and decreases in frequency for geometries with a greater number of turns. Such a phenomenon has not been found with the twin-arm geometry due to the different feeding arrangement. The current phases at the ends of the linear sections, where the helical arms begin, are held in anti-phase by the balanced feed regardless of the electrical circumference of the SHA.

The lack of a ground plane in the twin-arm geometry also has a potentially beneficial effect, as it causes the directivity of the antenna to decrease. This can be seen in Figure 4.18 which compares the half-power beamwidths for the twin-arm and conventional SHA.

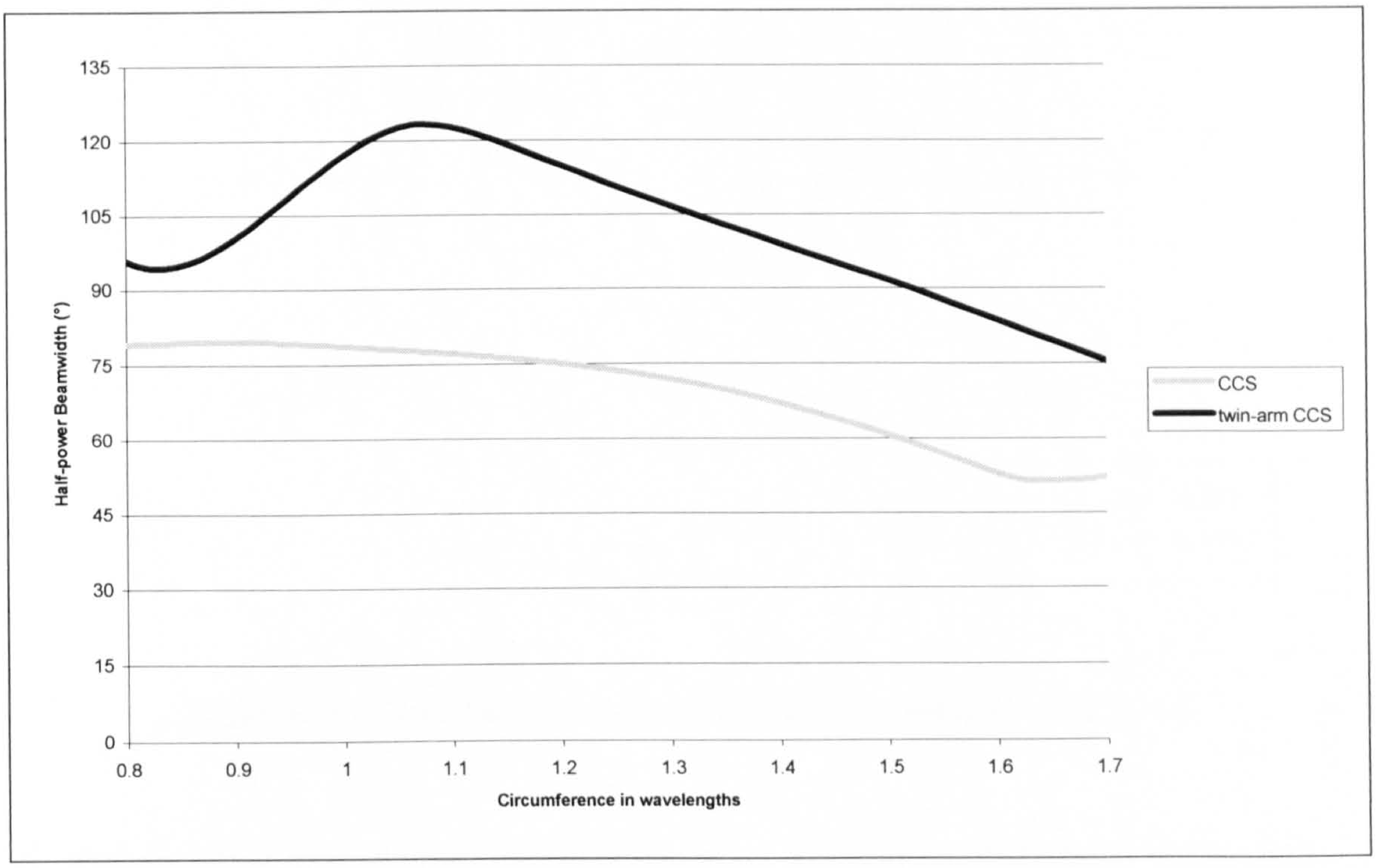

Figure 4.18 – Half-power beamwidth for 3-turn twin-arm and conventional SHA geometries

It is an aim of this research to find an antenna which is capable of producing CP over a wide beamwidth. In order for the CP to be usable, the radiation pattern must be as flat as possible over this range, thus a less-directive antenna with a greater HPBW is desirable.

Considering the gain and polarisation properties in the $\phi = 0°$ plane, shows that the twin-arm geometry is capable of maintaining its low axial ratio off-axis. Figure 4.19 shows the radiation pattern for a twin-arm SHA with a circumference of 1.6λ. The E_θ and E_ϕ components are plotted as normalised gains and show the characteristic large main lobe with no side lobes reported of the conventional SHA [2].

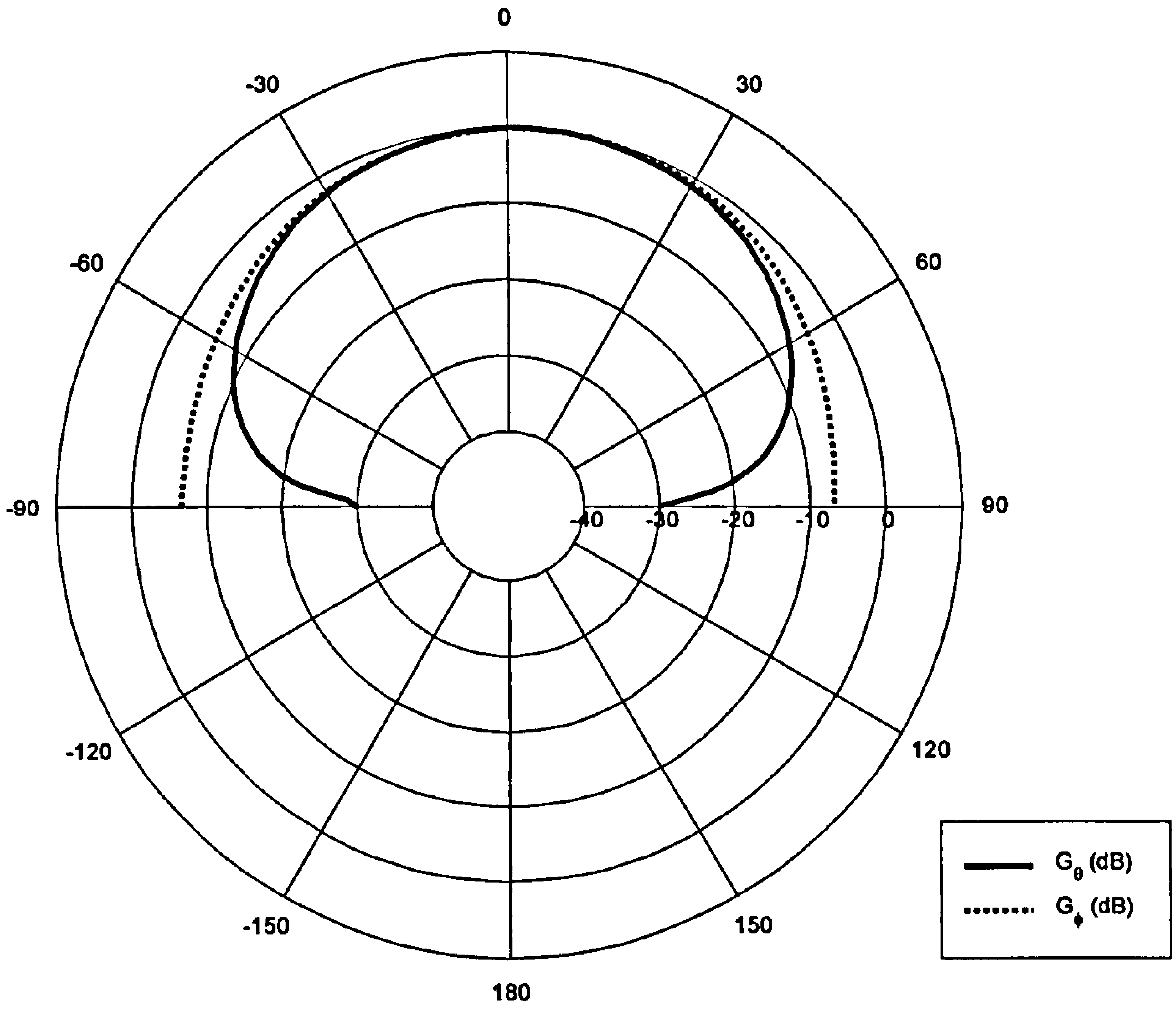

Figure 4.19 – Radiation pattern for 3-turn twin-arm SHA, $\phi = 0°$, C/λ=1.6

E_θ and E_ϕ are similar over a 120° angular range. If the phase difference between the two components is close to 90° in this region, then the CP performance is also maintained off-axis.

The axial ratio has been calculated and is shown in Figure 4.20. The 3dB AR beamwidth is 116° which is comparable, if not slightly better, than those reported for the conventional SHA [1,4,6]. It is also an improvement on the 107° AR beamwidth for the CCS SHA shown in Figure 4.6, though it should be noted that neither antennas were optimised so might be capable of producing greater AR beamwidths.

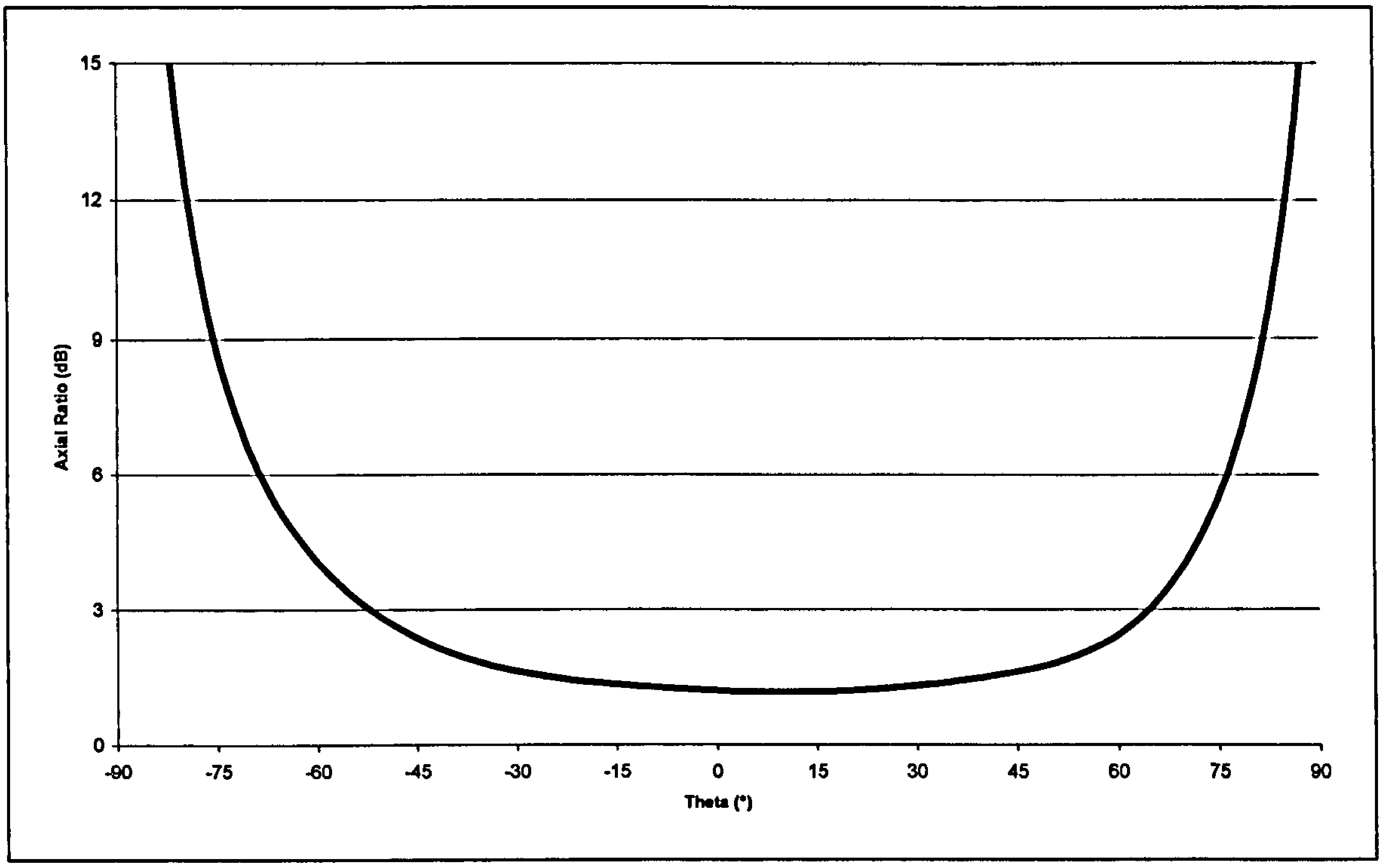

Figure 4.20 – Axial ratio for 3-turn twin-arm SHA with C=1.6λ, $\phi = 0°$

4.5 Cylindrical helix

In addition to modelling SHA geometries, the SHA-MoM code can also model cylindrical helices. This is useful as it allows direct comparison with the SHAs presented here. Kraus [10] reported that a 6-turn cylindrical helix with a 14° pitch angle provides good CP over a wide bandwidth. This antenna has been modelled and results are presented in this section.

Figure 4.21 shows the axial ratio for a frequency range which is centred where the circumference of the helix corresponds to one wavelength.

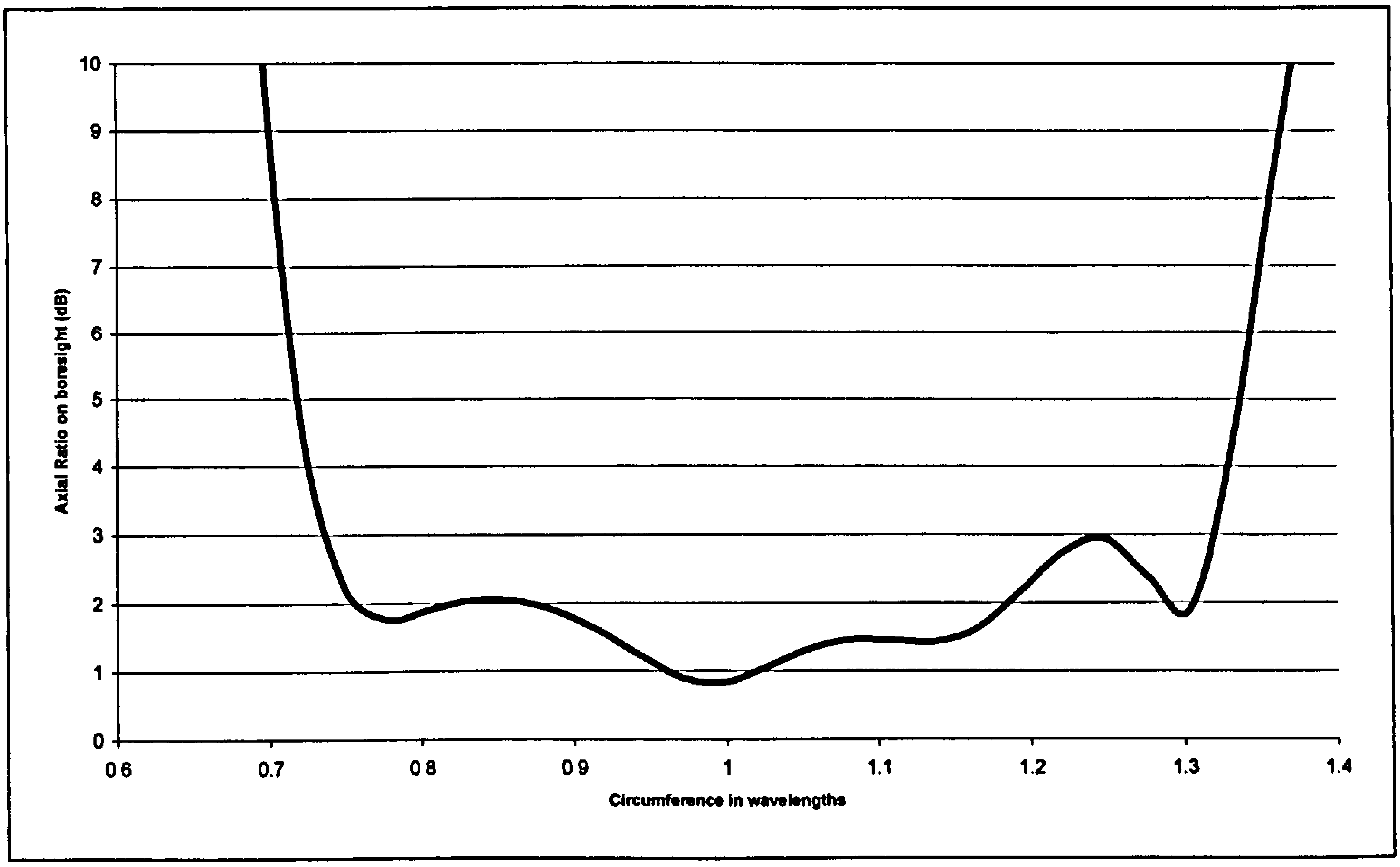

Figure 4.21 – Axial ratio on boresight of 6-turn cylindrical helix with 14° pitch angle, λ/10 above an infinite ground plane

Figure 4.21 shows that an axial ratio value of 3dB or better is achieved over a 57% bandwidth.

Figure 4.22 shows the gain characteristics over the same frequency range.

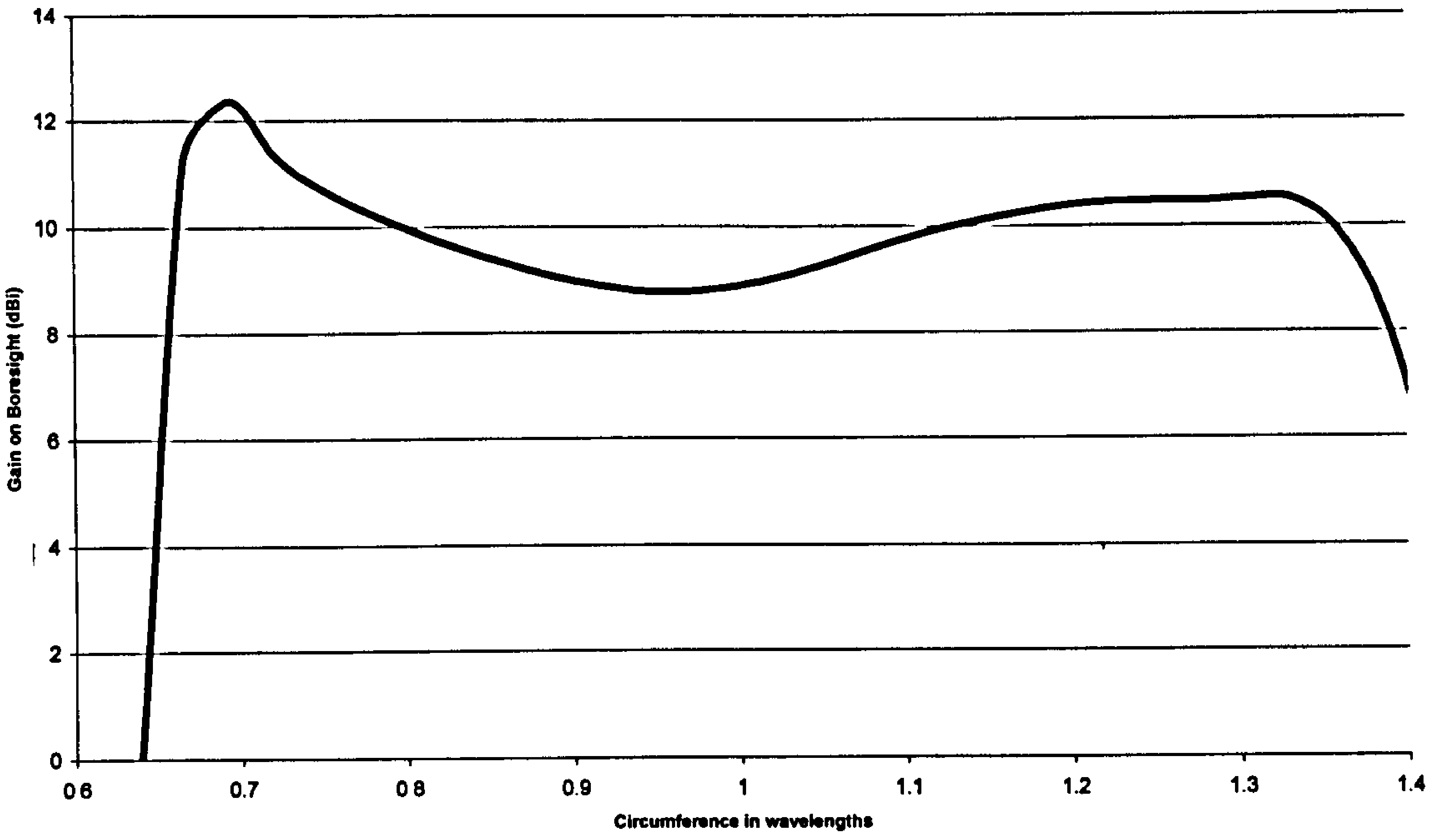

Figure 4.22 – Gain on boresight of 6-turn cylindrical helix with 14° pitch angle, λ/10 above an infinite ground plane

From Figure 4.22 it can be seen that over the 57% bandwidth where CP is radiated, a gain of between 8.8 and 10.7dB is achieved. This is a few dBs higher than that achieved by the SHA geometries shown previously, but the higher gain equates to a more directional antenna, as can be seen in Figure 4.23 which shows the beamwidths of the antenna.

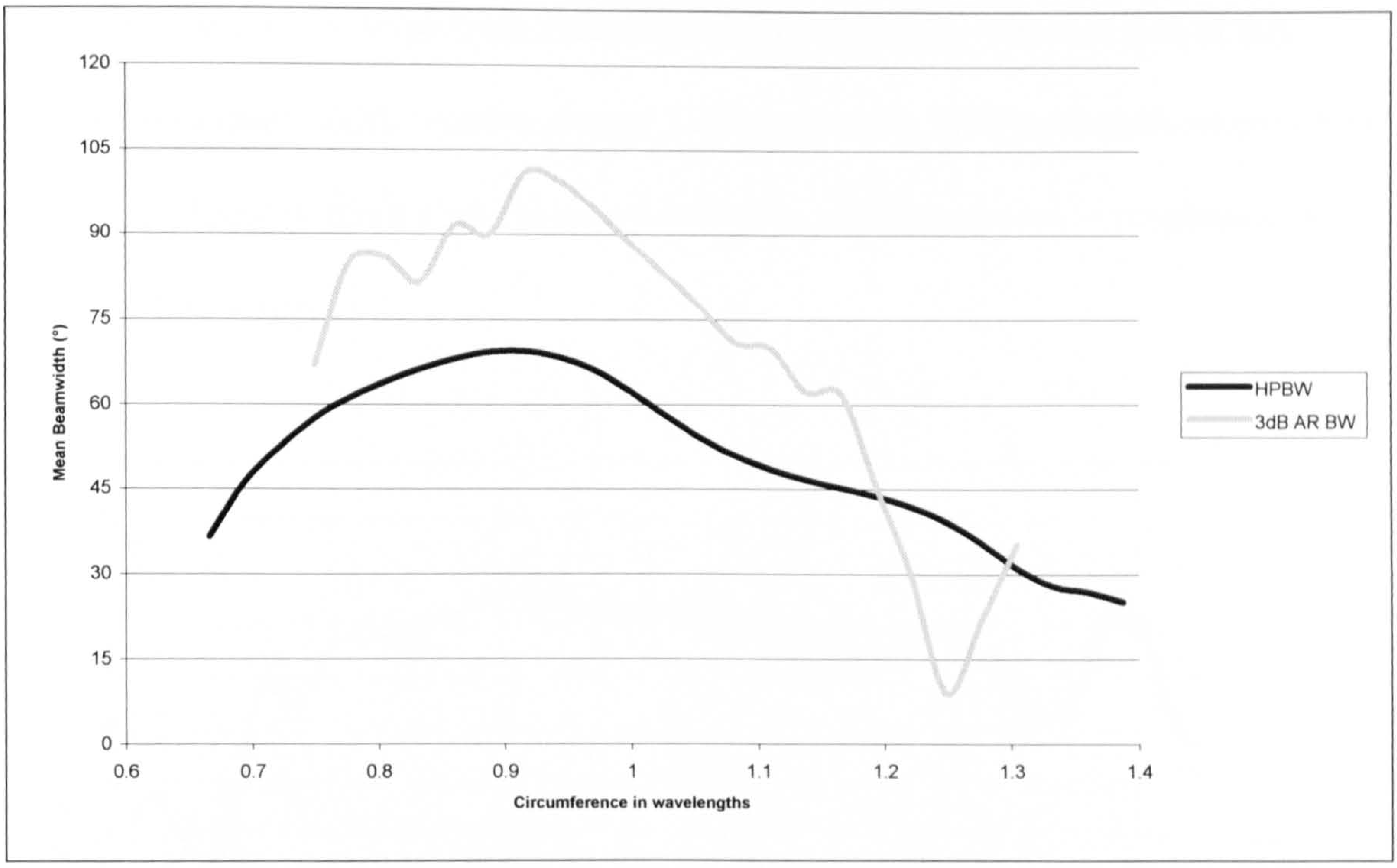

Figure 4.23 – HPBW and 3dB AR BW of 6-turn cylindrical helix with 14° pitch angle, $\lambda/10$ above an infinite ground plane

Figure 4.23 shows that although CP is maintained over a reasonable beamwidth, the HPBW is much lower, and thus is critical to dictating the useable beamwidth of the antenna. With a maximum beamwidth of 70° this helix is not capable of producing beamwidths as great as those shown for the twin-arm SHA geometry, seen previously.

Figure 4.24 shows the impedance characteristics of the helix. The real part of this shows a resistance which remains around 250Ω across the 57% bandwidth where CP is produced. There is also a slight negative reactance which increases in magnitude as frequency increases.

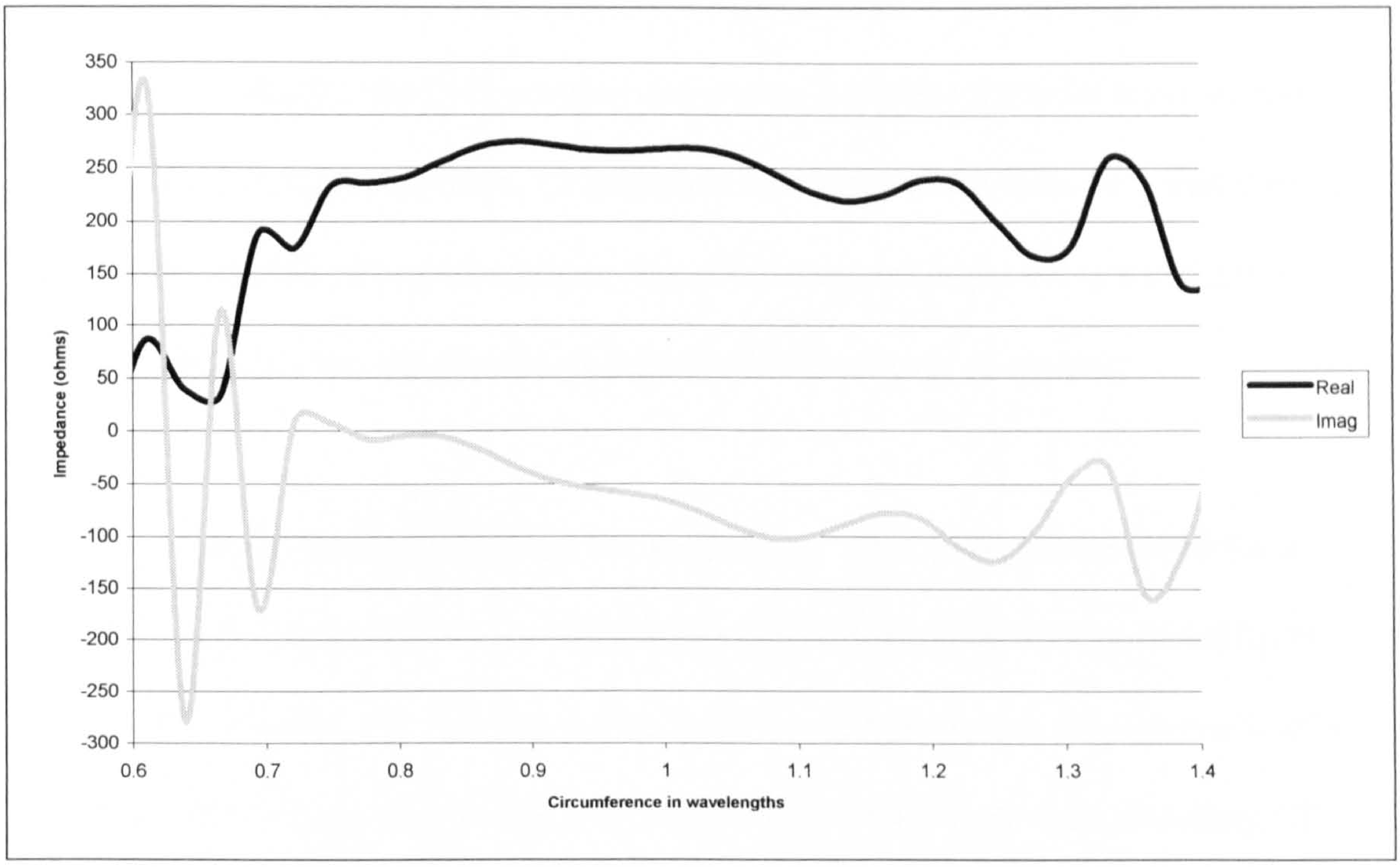

Figure 4.24 – Impedance characteristics of 6-turn cylindrical helix with 14° pitch angle, λ/10 above an infinite ground plane

4.6 Discussion

This chapter has described two significant modifications to the geometry of the conventional SHA, and considered the effects these changes have on the antenna's performance. Firstly, a new method for defining the spacing between turns has been given, and this has been shown to produce better CP both in the boresight direction, and off-axis. Specifically, the CCS scheme was shown to reduce the axial ratio on boresight and increase the AR beamwidth. Of particular interest was the discovery that the CCS geometry is capable of providing these low AR values and high AR beamwidths over larger bandwidths than the previously reported CVS scheme of spacing.

Secondly, a novel balanced feed has been proposed. This alleviates the need for a ground plane and so decreases the directivity of the antenna, increasing its half-power beamwidth. Although the presence of the linear section decreases the antenna's ability to produce CP at some frequencies, the antenna is still able to produce excellent CP with wide AR beamwidths.

The combination of wide half-power and AR beamwidths is encouraging but this chapter has also shown that the characteristics of the twin-arm geometry are less predictable than those of the conventional SHA. This makes antenna design more difficult, thus in the next chapter a GA will be applied to optimise the antenna, searching for a geometry which is capable of providing CP over a wide beamwidth and a reasonable bandwidth.

References

1 J. C. Cardoso and A. Safaai-Jazi, "Spherical helical antenna with circular polarisation over a broad beam", IEE Electronics Letters, vol. 29 (4), pp. 325-326, Feb. 1993.

2 A. Safaai-Jazi and J. C. Cardoso, "Radiation characteristics of a spherical helical antenna", IEE Proc-Microw. Antennas Propag, vol. 143, pp. 7-12, Feb. 1996.

3 H.T. Hui, K.Y. Chan, E.K.N. Yung, X.Q. Shing, "Coaxial-feed axial mode hemispherical helical antenna", IEE Electronics Letters, vol. 35 (23), pp. 1982-1983, Nov. 1999.

4 E. Weeratumanoon and A. Safaai-Jazi, "Truncated spherical helical antennas", IEE Electronics Letters, vol. 36 (7), pp. 607-609, Mar. 2000.

5 H. T. Hui, K. Y. Chan, and E. K. N. Yung, "The input impedance and the antenna gain of the spherical helical antenna", IEEE Trans. Antennas Propagat., vol. 49 (8), pp. 1235-1237, Aug. 2001.

6 H. T. Hui, K. Y. Chan, and E. K. N. Yung, "The low-profile hemispherical helical antenna with circular polarization radiation over a wide angular range", IEEE Trans. Antennas Propagat., vol. 51 (6), pp. 1415-1418, Jun. 2003.

7 Y. Ding, J.-H. Qiu, and W.-Y. Qin, "A New Spherical Helical Antenna", IEEE APS Int. Symp., 2005, vol. 2A, pp. 292 - 295, Jul. 2005.

8 H. Nakano, H. Takeda, T. Honma, H. Mimaki, J. Yamauchi, "Extremely low-profile helix radiating a circularly polarized wave", IEEE Trans. Antennas Propagat., vol. 39 (6), pp. 754-757, Jun. 1991.

9 K. Y. Chan, H. T. Hui, and E. K. N. Yung, "Central-fed hemispherical helical antenna", IEEE APS Int. Symp., 2001, vol. 4, pp. 545 - 548, Jul. 2001.

10 J. D. Kraus, "Antennas", McGraw-Hill, New York, 2nd Ed., 1988.

5 Optimisation

5.1 Introduction

The twin-arm geometry investigated in section 4.4 was found to have low directivity and thus produce wide beamwidths. It was also shown to be capable of producing CP over wide beamwidths. However, its characteristics were seen to change rapidly with both frequency and the number of turns, which makes design and optimisation difficult. In this chapter a GA will be applied to the antenna to optimise its performance.

In addition to the parameters discussed in Chapter 4, namely the number of turns and the electrical size of the antenna, the GA will also be given the ability to truncate the helical arms of the SHA. Weeratumanoon and Safaai-Jazi [6] have shown truncation to be beneficial for the conventional SHA. The twin-arm geometry has two helical arms, each of which can be truncated to a different length. This gives two further degrees of freedom to the GA.

This research has focussed on the ability of the SHA to provide circular polarisation. It is relatively easy to find an operating frequency where the axial ratio on boresight is close to 0dB, but it is more difficult to design an SHA which maintains this over a wide angular range. The added requirement that the gain must also be as flat as possible over the same range adds further complexity. It is this complexity, coupled with the relatively large number of parameters which can be varied to change the shape of the SHA which makes a GA particularly attractive for this problem.

In order to apply a GA, as with any optimisation technique, it is necessary to consider how the objectives are set. The manner in which this is done will play a significant role in determining what solutions are found. A common method in multi-objective optimisation is the use of a cost function, where a mathematical expression relates several performance markers to give an overall fitness value. This value is then either minimised or maximised under the optimisation. One drawback to this method is that the solutions obtained can be very sensitive to the weights set by the cost function. The GA can be used without a cost function. Instead of searching for the one "best" solution, it can search for a set of solutions which meet the various objectives to differing levels, but for which, solutions which offer improvements against all the objectives simultaneously do not exist. This is known as the Pareto-optimal set.

Two different multi-objective GA's were initially applied to this optimisation problem, a niched Pareto algorithm proposed by Horn [1] and a Fast Elitist Non-dominated Sorting GA (NSGA-II) proposed by Deb [2]. The latter of these was found to give faster convergence, which is critically important when each simulation can take several minutes. The results presented in this chapter have all been obtained using the NSGA-II algorithm. Further details of how the algorithm works are given in Appendix C.

The GA has been run a number of times, using different objectives and different ranges for the parameters. Three of these runs are presented in this chapter.

5.2 Mean axial ratio beamwidth

One of the measures of performance which will be maximised by the GA in this chapter is the axial ratio beamwidth. This is the beamwidth over which the axial ratio is less than 3dB, thus the polarisation of the antenna is close to circular.

Previous authors of papers on the SHA [3-9] have given values for the axial ratio beamwidth. In particular, Weeratumanoon and Safaai-Jazi [6] reported a 3dB axial ratio beamwidth of 80° for a 4-turn SHA truncated after 2.75 turns. Hui [8] reported an AR beamwidth of 90° for a 3-turn hemispherical helical antenna with a circumference of 1.2λ. However, neither author gave the AR beamwidth in any other elevation planes.

It has been shown previously [10] that the polarisation of radiation from a tapered cylindrical helix can vary dramatically with both θ and ϕ. Results obtained using SHA-MoM have shown that this is also true for the SHA.

Figure 5.1 and Figure 5.2 on the next page show the upper radiation hemispheres of two SHA antennas. The figures relate to the same geometry but at different frequencies. The angular regions in which the gain is within 3dB of its maximum are shown with solid lines, and the regions in which the axial ratio is less than 3dB are shown with dotted lines. The shaded areas show where both these criteria are satisfied simultaneously.

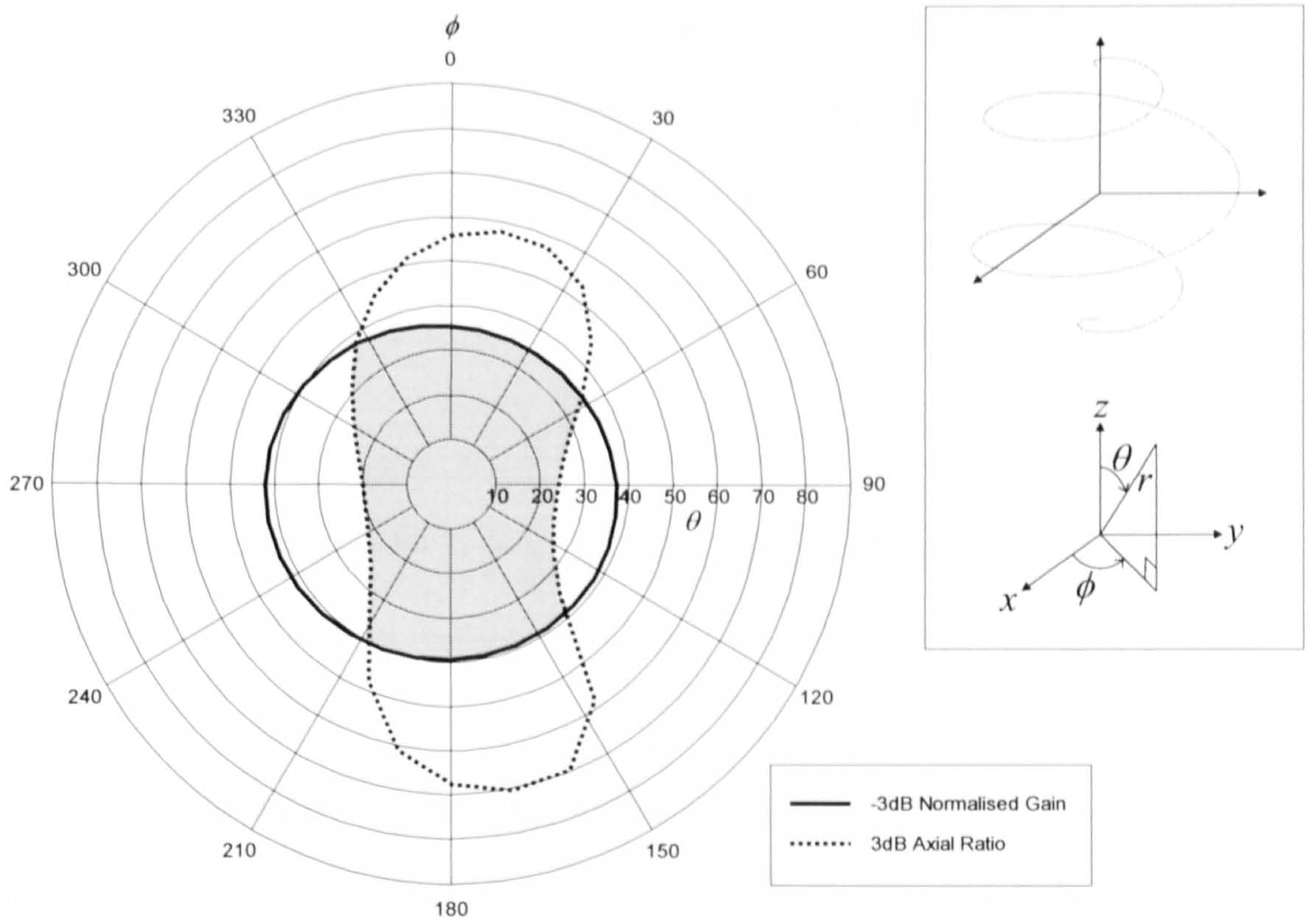

Figure 5.1 – Radiation hemisphere of a 3-turn CCS type SHA above a ground plane, C=1.1λ

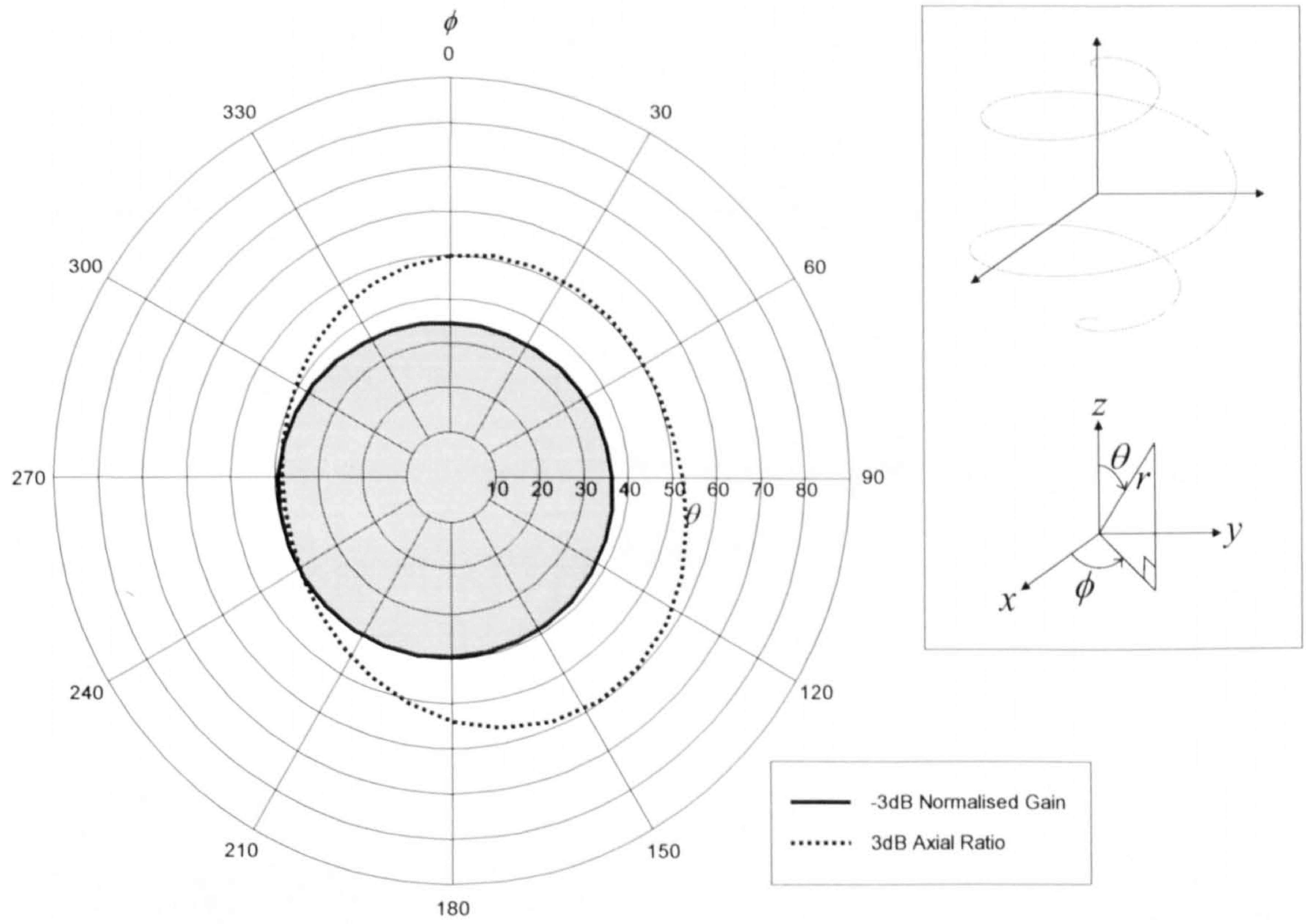

Figure 5.2 – Radiation hemisphere of a 3-turn CCS type SHA above a ground plane, C=1.2λ

Figure 5.1 and Figure 5.2 show that the gain regions are almost circular. Thus the HPBW would be similar irrespective of the azimuth. For the AR regions however, choosing different planes would give very different answers. It is also clear that the angular region of CP is very dependent on frequency.

It is desirable to use CP coverage as one of the objectives for the optimisation, but taking the axial ratio beamwidth in different planes can give dramatically different results. A method is therefore required to alleviate this issue.

The method proposed here is to calculate a mean axial ratio beamwidth. The AR beamwidth is taken in a number of planes then the results averaged. For the GA's presented in this chapter which have used mean axial ratio as an optimisation objective 16-cuts have been used. This number was chosen so as to minimise the chance of fluctuations in the AR beamwidth occurring between cuts, whilst not adding too great a computational overhead to the simulation. As the choice of 16-cuts is somewhat arbitrary it will be reviewed and discussed at the end of this chapter.

For consistency, values for half-power beamwidth will also be averaged over the same 16 cuts, though it should be noted that the HPBW varies substantially less than the AR beamwidth, as can be seen in Figure 5.1 and Figure 5.2.

5.3 Dual-objective optimisation (integer N)

The first optimisation presented here is dual-objective aiming to produce the best CP and the highest gain in the boresight direction. The GA had control over the number of turns in the SHA, though only integer numbers of turns were allowed for this run. The GA was also free to truncate the two arms of the twin-arm geometry independently and at any point from 20% along the curved section of the arm, to the end (i.e. no truncation.) For convenience the frequency at which the antennas were simulated was fixed and the GA varied the radius of the SHA, thus varying the electrical size of the antenna. As the analysis is in free-space the model is completely scalable. Table 5.1 and Table 5.2 summarise the parameter ranges and optimisation goals.

Variable	**Minimum**	**Maximum**
Number of turns	2	10
Upper hemisphere truncation	0%	75%
Lower hemisphere truncation	0%	75%
Circumference of sphere	0.5λ	2λ

Table 5.1 – Parameter ranges for dual-objective optimisation

Objective	**Target**
Axial ratio on boresight	Minimise
Gain on boresight	Maximise

Table 5.2 – Objectives for dual-objective optimisation

A population size of 50 was used, and the GA allowed to run for 50 generations. Figure 5.3 shows the solution space of the initial population which were chosen at random.

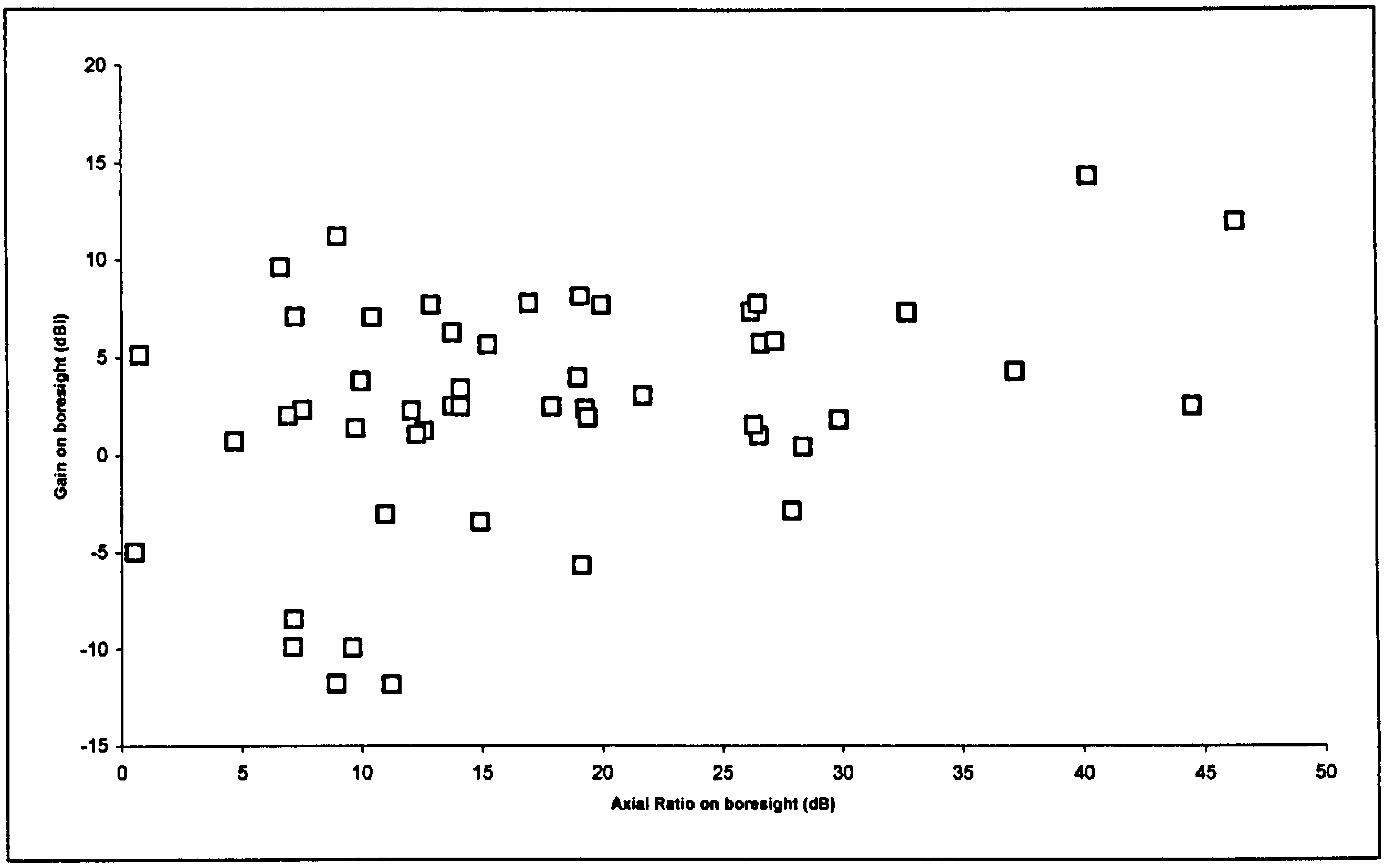

Figure 5.3 – Solution space of initial population

With successive generations the solution space converged quickly and the final generation can be seen in Figure 5.4. Generations from about 20 onwards had solution spaces which were very similar, showing that convergence occurred quickly.

Figure 5.4 also demonstrates how this GA maintains a set of different solutions which satisfy the two criteria, maximum gain and minimum AR, to differing degrees. If a cost function had been used, the weightings would have influenced which of these solutions were deemed to be best, and thus the others would have been discarded. With a set of solutions to choose from, the particular solution which best meets the two criteria for a specific application can be chosen after the optimisation.

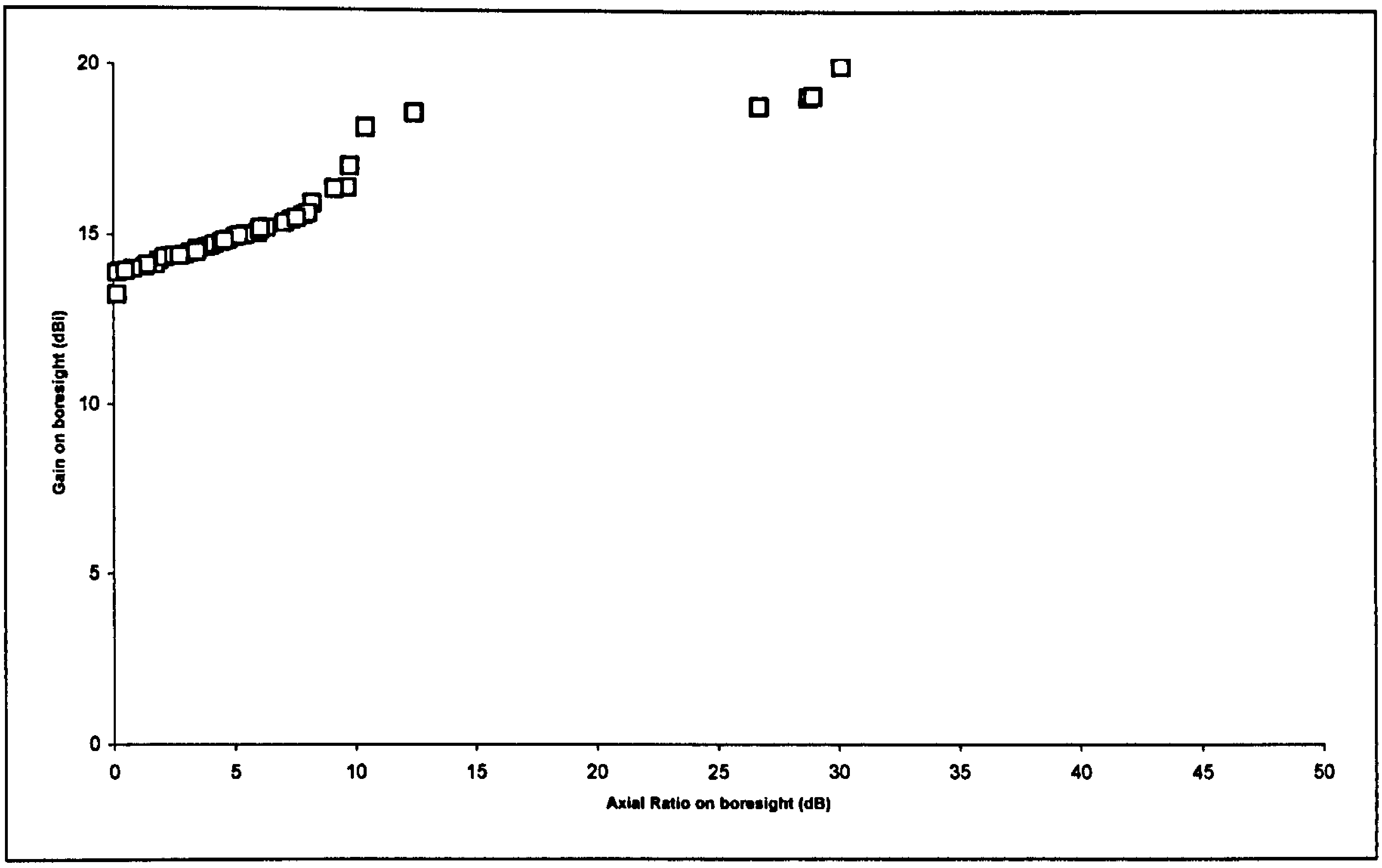

Figure 5.4 – Solution space of final generation

Table 5.3 shows the parameters and characteristics of the best antennas found by the GA. N gives the number of turns, and R is the radius (in cm) of the SHA. The frequency was fixed at 2GHz. `END_POINT` is the parameter given to the SHA-MoM code which describe the proportion of the curved length of the helical arm covering the upper hemisphere and `END_POINT2` works in the same manner for the arm in the lower hemisphere.

It is interesting to note that all the best antennas found by the GA have 3 turns. Fifteen of the antennas in the final generation produce CP in the boresight direction, and these have gains of 13dB or more. This is higher that the 9-10dB reported for the SHA previously [7] but it should be noted that this gain might be at the expense of a reduced half-power beamwidth. This issue will be addressed later by including the maximisation of HPBW in the optimisation.

N	R	END_POINT	END_POINT2	Axial ratio (dB)	Gain (dBi)
3	2.268	0.883	0.268	0.158	13.176
3	2.372	0.849	0.255	0.179	13.832
3	2.353	0.856	0.254	0.285	13.881
3	2.369	0.853	0.255	0.519	13.891
3	2.477	0.82	0.255	0.814	13.959
3	2.302	0.88	0.254	1.327	14.028
3	2.426	0.842	0.255	1.4	14.076
3	2.38	0.858	0.256	1.639	14.085
3	2.353	0.867	0.255	1.738	14.087
3	2.439	0.841	0.255	1.882	14.204
3	2.434	0.844	0.254	2.118	14.294
3	2.417	0.851	0.253	2.329	14.341
3	2.456	0.84	0.255	2.507	14.352
3	2.416	0.855	0.255	2.749	14.356
3	2.446	0.847	0.256	2.953	14.391
3	2.401	0.863	0.255	3.184	14.457
3	2.325	0.888	0.254	3.442	14.483
3	2.375	0.873	0.253	3.462	14.576
3	2.394	0.87	0.254	3.831	14.619
3	2.447	0.854	0.256	4.015	14.651
3	2.393	0.872	0.254	4.167	14.714
3	2.442	0.859	0.255	4.477	14.781
3	2.417	0.868	0.254	4.611	14.824
3	2.396	0.876	0.254	4.744	14.846
3	2.443	0.863	0.255	5.071	14.939
3	2.45	0.862	0.255	5.198	14.973
3	2.447	0.865	0.256	5.406	14.99
3	2.45	0.864	0.256	5.475	15.011
3	2.48	0.858	0.258	5.976	15.058

Table 5.3 – Best solutions for dual-objective optimisation

5.4 Dual-objective optimisation (non-integer N)

The second run of the GA presented here was again dual-objective but allowed the parameters to be varied over greater ranges. Table 5.1 shows the four parameters and their respective ranges. Table 5.2 shows the objectives for the GA which are the same as for the previous run.

Variable	**Minimum**	**Maximum**
Number of turns	1.0	10.0
Upper hemisphere truncation	0%	80%
Lower hemisphere truncation	0%	80%
Circumference of sphere	0.2λ	2.5λ

Table 5.4 – Parameter ranges for dual-objective optimisation

Objective	**Target**
Axial ratio on boresight	Minimise
Gain on boresight	Maximise

Table 5.5 – Objectives for dual-objective optimisation

A population size of 50 was chosen, with a mutation probability of 5%. The GA ran for 58 hours, modelling 50 generations, and calling the SHA-MoM code a total of 2550 times. Table 5.6 on the next page shows the best 25 solutions obtained after 50 generations of the genetic algorithm. These solutions have been sorted into ascending order of axial ratio. The remaining 25 solutions had higher axial ratios and have not been shown.

Solution No.	N	C/λ	END_POINT	END_POINT2	Axial ratio (dB)	Gain (dBi)
1	4.61	0.92	0.931	0.739	0.04	4.82
2	**2.87**	**1.40**	**0.791**	**0.247**	**0.08**	**11.22**
3	**6.88**	**1.78**	**0.948**	**0.210**	**0.19**	**15.99**
4	**6.88**	**1.79**	**0.955**	**0.210**	**0.37**	**16.08**
5	**6.88**	**1.80**	**0.962**	**0.210**	**0.74**	**16.13**
6	**6.88**	**1.76**	**0.976**	**0.210**	**0.98**	**16.43**
7	**1.44**	**1.53**	**0.99**	**0.213**	**2.18**	**19.66**
8	**1.42**	**1.53**	**0.991**	**0.213**	**2.21**	**19.93**
9	**1.33**	**1.59**	**0.991**	**0.206**	**2.55**	**20.33**
10	**1.31**	**1.60**	**0.989**	**0.204**	**2.68**	**20.53**
11	1.31	1.58	0.990	0.212	3.14	20.64
12	1.24	1.64	0.990	0.202	3.16	20.88
13	1.24	1.63	0.991	0.206	3.50	21.08
14	1.31	1.56	0.991	0.206	3.85	21.38
15	1.28	1.58	0.989	0.204	4.14	21.61
16	1.26	1.59	0.980	0.204	4.86	21.95
17	1.16	1.64	0.990	0.210	5.34	22.17
18	1.21	1.59	0.983	0.205	5.61	22.36
19	1.14	1.62	0.993	0.217	6.25	22.41
20	1.13	1.64	0.980	0.206	6.66	22.94
21	1.10	1.64	0.986	0.206	6.92	23.12
22	1.03	1.79	0.945	0.200	7.56	23.39
23	1.00	1.78	0.952	0.200	7.87	23.65
24	1.03	1.70	0.975	0.204	7.98	23.72
25	1.03	1.61	0.988	0.209	8.80	23.76

Table 5.6 – Best 25 solutions for dual-objective optimisation

The nine solutions which have been highlighted have axial ratios values which are less than 3dB, and gains of more than 10dBi. They are therefore worth considering further.

Although this GA only searched for minimum AR and maximum gain values on boresight, it is interesting to consider what the half-power and 3dB axial ratio beamwidths of these antennas are. These have been calculated and are shown in Table 5.7. Both values for beamwidth have been averaged over 16-cuts as described in section 5.2. The 'Useable Beamwidth' column is the lower of the two beamwidth values, and gives a measure of the beamwidth over which the antenna satisfies both gain and AR criteria.

Solution No.	Axial ratio (dB)	Gain (dBi)	Mean HPBW (°)	Mean 3dB AR Beamwidth (°)	Useable Beamwidth (°)
2	0.08	11.22	88.9	118.5	88.9
3	0.19	15.99	80.0	138.0	80.0
4	0.37	16.08	79.5	138.7	79.5
5	0.74	16.13	78.5	140.0	78.5
6	0.98	16.43	79.6	132.6	79.6
7	2.18	19.66	122.4	84.9	84.9
8	2.21	19.93	123.9	83.2	83.2
9	2.55	20.33	117.8	75.6	75.6
10	2.68	20.53	117.8	72.0	72.0

Table 5.7 – Beamwidths of solutions 2 through 10 of Table 5.6

5.5 Quad-objective optimisation

The third optimisation presented here was designed to find an antenna which produced CP over as much of the radiation hemisphere as possible. Such an antenna would be capable of receiving signals from as many directions as possible. The criteria are:- a flat gain response with reasonable gain on boresight, and an axial ratio less than 3dB. Two additional goals will be used:- to maximise the mean 3dB AR beamwidth, and to maximise the half-power beamwidth. The two objectives used in the previous runs will also be used, as these will steer the GA when solutions are found with axial ratios greater than 3dB. Such solutions will not have a mean AR beamwidth so need to be differentiated by other measures. Table 5.8 and Table 5.9 summarise the goals and parameter ranges used.

Objective	**Target**
Axial ratio on boresight	Minimise
Gain on boresight	Maximise
Mean 3dB AR beamwidth	Maximise
Mean Half-power beamwidth	Maximise

Table 5.8 – Objectives for quad-objective optimisation

Variable	**Minimum**	**Maximum**
Number of turns	2.0	10.0
Upper hemisphere truncation	0%	80%
Lower hemisphere truncation	0%	80%
Circumference of sphere	0.5λ	2λ

Table 5.9 – Parameter ranges for quad-objective optimisation

A population size of 80 was chosen. This was increased from the previous run to accommodate the larger non-dominated set which will result from the increase in optimisation objectives.

The GA was allowed to run for 12 generations. The simulations took on average 9 minutes, mainly due to the time taken to calculate 16 radiation cuts. A total of 1040 antennas were simulated and the GA ran for just under a week.

During the optimisation only 39 solutions had axial ratio less than 3dB. These are shown in Table 5.10, sorted by mean axial ratio beamwidth. Numbers are shown rounded in the table. The GA antenna number given in the first column is a unique number given to each test antenna created by the GA and serves as a useful method for referring to individual antennas.

Solutions shown in bold are non-dominated in terms of AR- and half-power beamwidths; that is there were no other antennas which performed better against both of the criteria simultaneously. See Appendix C for a description of non-dominated members of a population.

The three columns on the right of Table 5.10 indicate the bandwidth of the antenna, which were calculated retrospectively, after the GA had finished. Various bandwidths have been calculated for the various criteria required, namely axial ratio of boresight less than 3dB, gain greater than 3dB of the maximum, and impedance bandwidth calculated for a VSWR less than 2:1. The smallest of these three values will determine the actual bandwidth of the antenna, and has been shown in bold in the table.

GA Antenna No.	N	C/λ	end_point	end_point2	Gain on boresight (dBi)	AR on boresight (dB)	Mean HPBW (°)	Mean 3dB AR BW (°)	Bandwidth (%)		
									AR	Gain	Impedance
197	**5.07**	**1.26**	**0.71**	**0.25**	**12.3**	**1.94**	**95.8**	**116.1**	22.1	32.7	**7.9**
969	**4.64**	**1.25**	**0.75**	**0.29**	**11.5**	**1.04**	**98.0**	**112.2**	13.6	33.3	**8.1**
340	6.74	1.58	0.38	0.39	5.4	0.25	83.8	110.5	7.5	49.1	**5.0**
44	5.73	1.26	0.38	0.41	4.4	1.52	94.7	106.8	12.7	46.5	**3.3**
800	**2.25**	**1.20**	**0.91**	**0.68**	**7.4**	**0.77**	**105.2**	**105.0**	6.2	46.0	**0.4**
100	2.99	1.65	0.95	0.51	8.5	1.76	84.1	104.9	7.4	37.4	**3.7**
574	6.02	1.46	0.42	0.30	7.1	0.77	87.1	102.8	11.4	44.3	**4.0**
1026	2.48	1.50	0.87	0.70	6.5	1.31	87.8	101.0	6.9	49.6	**2.9**
41	4.42	1.44	0.22	0.42	5.0	1.13	88.2	96.0	4.8	27.2	**3.0**
575	2.43	1.41	0.85	0.30	11.4	2.29	92.3	94.2	6.7	37.9	**1.8**
479	9.49	1.01	0.62	0.89	3.3	0.72	83.3	94.1	3.0	32.7	**1.8**
309	3.23	1.35	0.69	0.68	4.7	2.35	94.6	93.8	10.4	49.0	**3.8**
534	8.37	0.92	0.41	0.72	3.6	1.81	90.0	93.7	3.0	25.6	**0.3**
854	2.84	0.89	0.99	0.24	15.0	0.36	96.5	92.7	5.5	36.7	**0.7**
108	8.48	1.04	0.79	0.57	3.9	0.53	84.7	90.4	6.1	11.5	**1.0**
423	4.15	1.25	0.44	0.89	2.9	2.45	93.3	85.9	**5.5**	47.8	10.5
1014	6.22	1.36	0.78	0.22	11.8	2.60	100.4	85.1	11.7	37.2	**5.6**
867	5.22	1.30	0.69	0.30	9.8	2.75	100.1	84.6	11.8	37.5	**10.4**
623	5.05	1.28	0.74	0.31	10.4	2.93	97.0	82.9	12.0	38.0	**7.0**
572	4.59	1.46	0.52	0.41	6.8	2.44	88.3	81.7	7.0	47.9	**4.8**
223	3.06	1.14	0.72	0.51	7.5	2.13	103.8	81.6	6.1	41.9	**0.6**
807	**4.71**	**1.18**	**0.21**	**0.24**	**2.8**	**1.92**	**109.2**	**80.7**	4.3	13.9	**1.0**
547	4.12	1.43	0.62	0.93	3.7	2.59	83.8	78.6	**6.4**	28.2	8.7
178	8.24	0.80	0.62	0.48	5.8	1.99	86.8	76.0	1.6	3.6	**0.2**
779	**2.51**	**1.28**	**0.76**	**0.61**	**7.1**	**2.24**	**111.2**	**75.6**	4.4	49.9	**0.7**
813	5.28	1.15	0.64	0.45	4.5	2.76	86.5	73.2	1.7	3.4	**0.9**
318	4.46	1.19	0.73	0.53	5.8	2.51	90.5	70.8	26.1	24.7	**1.9**
560	6.92	0.70	0.60	0.57	2.1	1.48	93.6	69.8	0.7	23.5	**0.1**
551	3.01	1.08	0.78	0.42	9.5	2.68	100.2	61.6	4.6	30.6	**0.7**
208	5.15	1.47	0.82	0.54	7.1	2.56	82.6	60.4	**4.5**	35.3	5.1
296	2.10	1.52	0.50	0.84	4.8	2.78	90.5	58.2	5.5	37.4	**3.1**
175	6.78	1.46	0.54	0.50	3.8	2.43	89.1	56.4	**4.5**	33.9	5.1
219	2.00	1.92	0.97	0.31	10.2	2.41	95.8	56.1	**0.7**	6.2	5.2
150	2.47	1.35	0.77	0.39	10.3	2.84	101.1	49.8	6.1	36.8	**2.0**
708	5.25	1.14	0.68	0.56	5.6	2.93	94.0	41.4	**8.1**	30.0	15.9
339	5.58	1.78	0.40	0.28	7.3	2.99	90.5	41.0	**0.0**	35.6	3.0
99	2.43	1.59	0.33	0.26	7.2	2.47	93.5	32.7	3.4	10.1	**2.0**
899	4.65	1.04	0.42	0.23	2.2	2.13	92.5	32.3	3.2	8.6	**0.5**
691	3.18	1.28	0.42	0.26	5.8	2.99	92.7	17.8	2.9	10.8	**1.1**

Table 5.10 – Solutions from quad-objective GA with less than 3dB axial ratio on boresight (Solutions shown in bold are non-dominated in terms of AR- and Gain- beamwidths)

Figure 5.5 present the 39 antennas diagrammatically to show the relationship between their attained mean HPBW and mean axial ratio beamwidth.

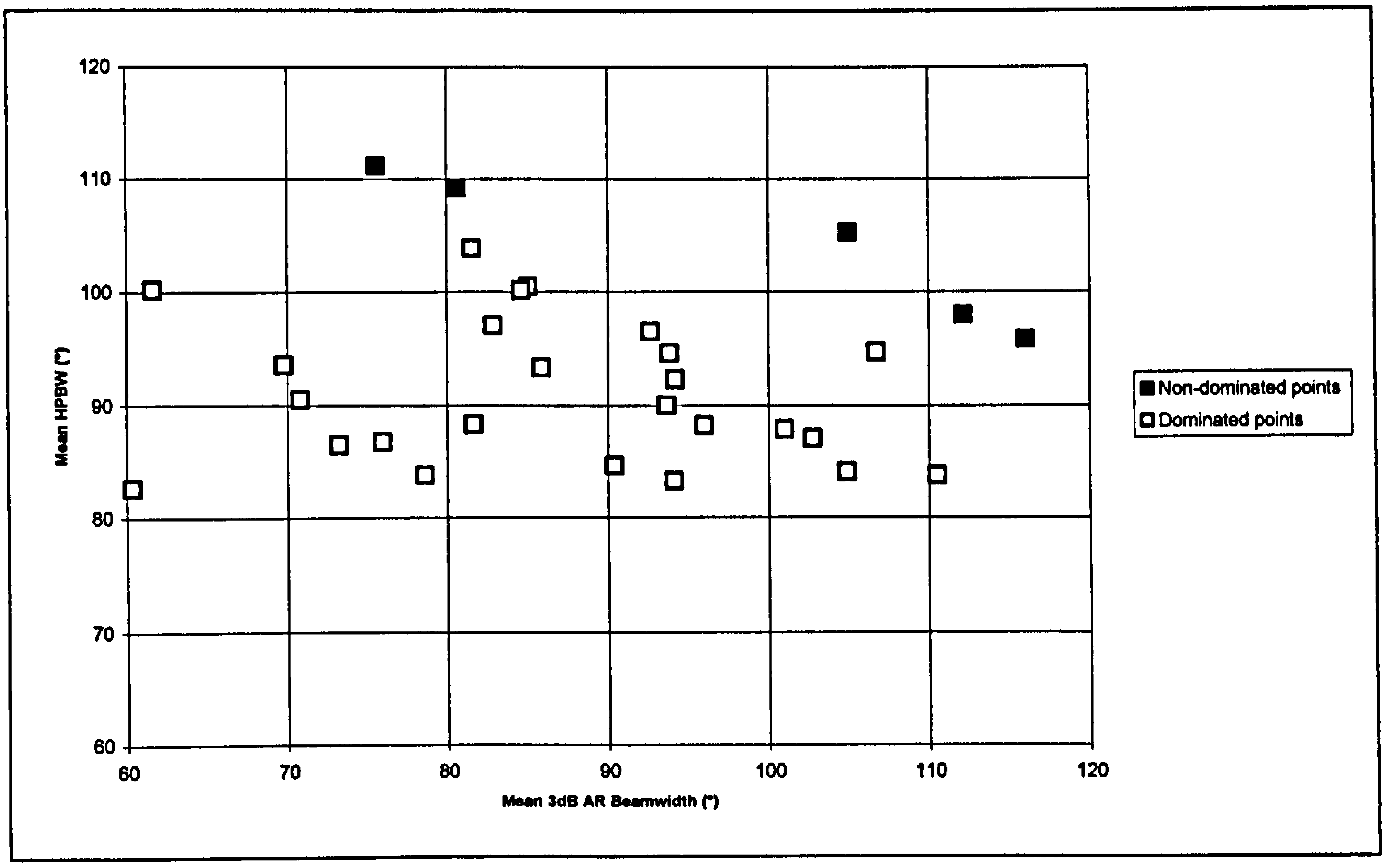

Figure 5.5 – Half-power beamwidth vs. mean AR beamwidth for best antennas

It was the goal of the optimisation to maximise both the HPBW and the axial ratio beamwidth. In practical terms it is the minimum of these two values which will limit the performance of the antenna.

Referring back to Table 5.10 the antenna whose minimum value of HPBW and axial ratio beamwidth, is the greatest, is antenna No. 800. This antenna has a mean AR beamwidth of 105.0° and a HPBW of 105.2°. Its AR on boresight is 0.77dB and its gain is 7.4dB. The parameters which define the antenna are given in Table 5.11.

N	C/λ	`end_point`	`end_point2`
2.25	1.20	0.91	0.68

Table 5.11 – Parameters for antenna No. 800

Figure 5.6 shows the radiation hemisphere for this antenna. The 3dB AR region is seen to be skewed to one side and takes on an irregular shape.

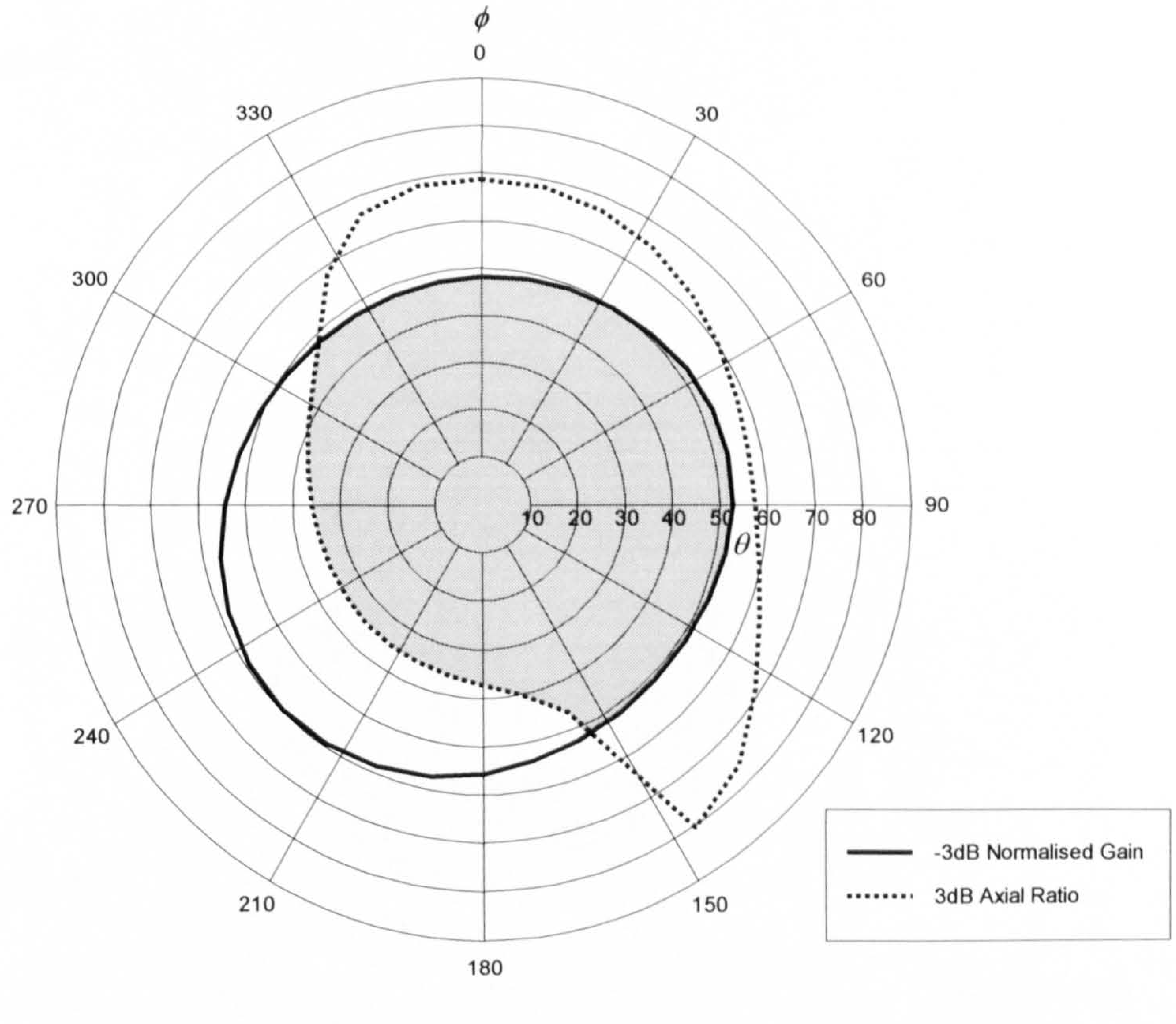

Figure 5.6 – Radiation hemisphere for antenna No. 800

Also of interest from Table 5.10 is the antenna with the highest value of AR beamwidth. This is antenna No. 197 which has a mean AR beamwidth of 116.1° and a HPBW of 95.8°. Its gain on boresight is 12.3dB and its axial ratio is 1.94. The parameters which define the antenna are given in Table 5.12

N	C/λ	`end_point`	`end_point2`
5.07	1.26	0.71	0.25

Table 5.12 – Parameters for antenna No. 197

The radiation hemisphere for antenna No. 197 is shown in Figure 5.7. Although the region where the gain is within 3dB of its maximum is smaller than the region for which CP is produced, the simulation data showed that the gain is within 6dB of its maximum over the CP region.

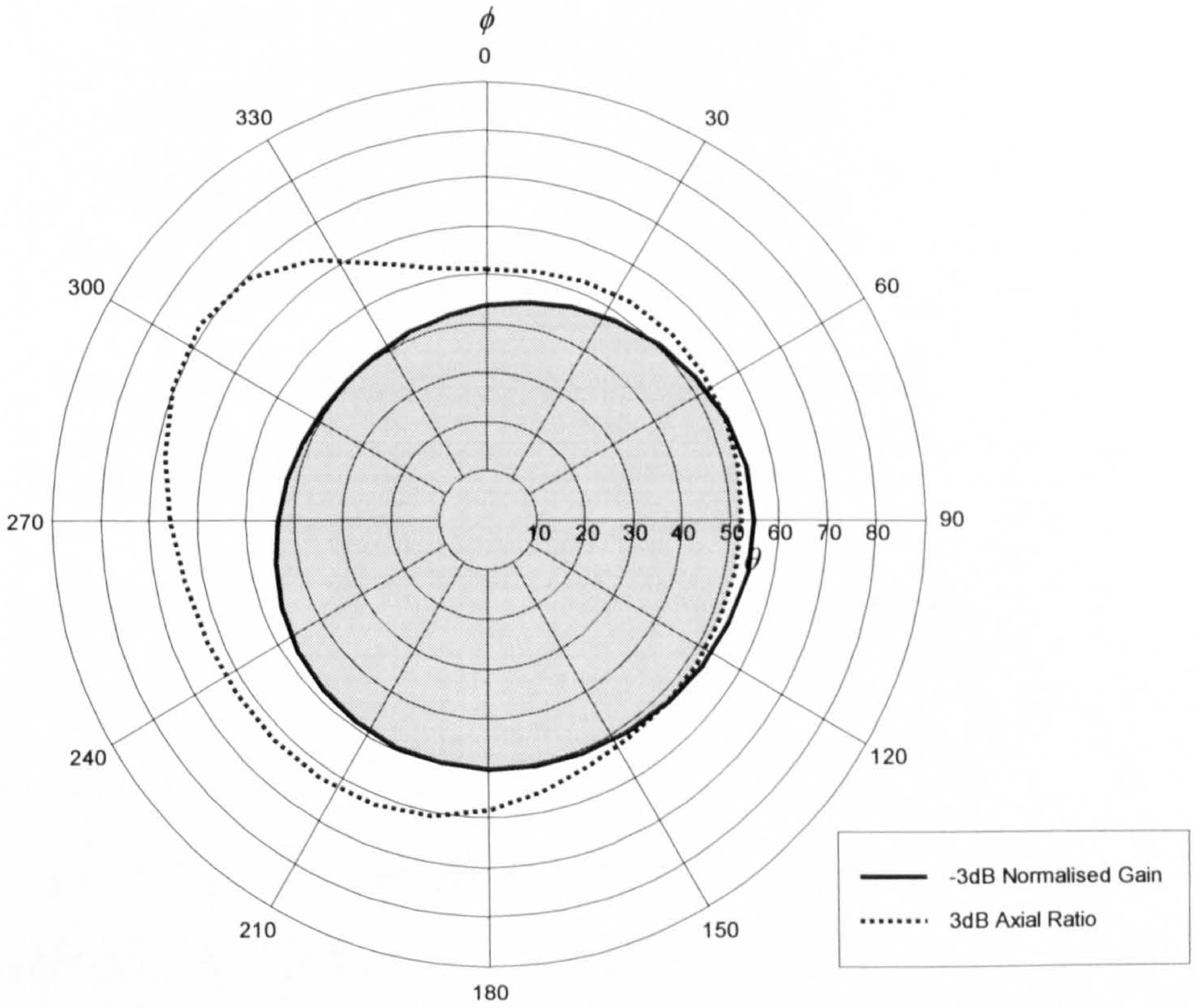

Figure 5.7 – Radiation hemisphere for antenna No. 197

5.6 Combined-objective optimisation

The previous GA, which aimed to separately maximise the axial ratio beamwidth and HPBW, was prone to finding solutions where both these values were high but where the combined region, where both of the criteria were met, was much smaller. A typical example of this was seen in Figure 5.6. The GA in this section overcomes this problem by attempting to maximise the combined beamwidth. The combined beamwidth is the beamwidth over which both the gain and AR criteria are met simultaneously, namely where the gain is greater than half its maximum and the axial ratio is less than 3dB. This combined beamwidth is calculated over a number of different cuts, and then the mean value returned. Table 5.13 and Table 5.14 summarise the goals and parameter ranges used.

Objective	**Target**
Axial ratio on boresight	Minimise
Gain on boresight	Maximise
Mean combined beamwidth	Maximise

Table 5.13 – Objectives for combined-objective optimisation

Variable	**Minimum**	**Maximum**
Number of turns	2.0	10.0
Upper hemisphere truncation	0%	80%
Lower hemisphere truncation	0%	80%
Circumference of sphere	0.5λ	2λ

Table 5.14 – Parameter ranges for combined-objective optimisation

As with the quad-objective GA previously, a population size of 80 was chosen and the GA was allowed to run for nearly a fortnight producing 27 generations and simulating a total of 2240 antennas. The 25 antennas with the highest combined beamwidth are given in Table 5.15.

GA Antenna No.	N	C/λ	end_point	end_point2	AR on boresight (dB)	Gain on boresight (dBi)	Combined beamwidth (°)	Bandwidth (%)		
								AR	Gain	Impedance
2656	3.44	1.25	0.99	0.47	1.8	10.1	97.7	8.2	29.0	**2.0**
2960	3.42	1.35	0.93	0.35	1.7	11.9	96.8	10.1	30.8	**5.7**
3549	3.47	1.38	0.91	0.31	1.8	12.7	96.0	10.1	28.7	**7.3**
2707	4.00	1.31	0.84	0.28	2.1	12.9	96.0	10.9	29.1	**7.5**
3673	3.35	1.37	0.93	0.36	1.3	11.6	95.9	9.8	32.7	**6.4**
3942	3.49	1.38	0.90	0.31	1.6	12.6	95.9	10.3	28.8	**7.7**
3941	3.49	1.38	0.90	0.31	1.5	12.6	95.9	10.3	28.9	**7.9**
3921	3.48	1.38	0.90	0.31	1.3	12.6	95.9	10.2	29.0	**8.4**
3507	3.49	1.38	0.89	0.31	1.0	12.5	95.6	10.2	29.3	**9.3**
3265	3.66	1.37	0.88	0.28	2.1	13.1	95.3	9.7	27.8	**8.1**
3242	3.42	1.38	0.93	0.33	2.4	12.4	94.8	9.7	29.9	**6.1**
3974	3.65	1.37	0.89	0.66	2.1	6.3	93.7	37.2	39.8	**6.5**
3241	3.42	1.32	0.96	0.44	2.2	10.3	93.5	9.3	33.6	**4.1**
2298	8.09	1.15	0.48	0.24	0.9	8.8	93.3	12.7	49.6	**9.3**
3306	3.08	1.11	0.76	0.20	1.7	16.0	93.3	6.1	48.6	**0.5**
4212	4.97	1.25	0.71	0.23	2.2	13.0	92.6	21.3	28.8	**12.8**
3664	3.50	1.42	0.85	0.25	0.9	13.5	92.1	**8.8**	26.3	10.4
3106	3.15	1.48	0.92	0.61	0.8	7.3	91.9	11.8	36.9	**7.6**
2913	4.20	1.36	0.75	0.23	0.5	13.3	91.3	**9.3**	28.1	10.1
2308	5.17	1.34	0.69	0.46	1.2	6.7	91.0	20.1	34.4	**7.5**
4211	4.66	1.32	0.70	0.21	1.1	13.3	90.7	**9.8**	27.8	9.9
4121	3.49	1.43	0.85	0.25	0.6	13.4	90.6	**8.4**	28.6	9.5
3420	3.37	1.50	0.92	0.54	1.7	7.8	89.5	10.6	44.3	**5.3**
3310	3.05	1.48	0.94	0.61	1.5	7.6	89.2	10.5	49.2	**8.0**
3170	4.64	1.41	0.96	0.23	1.9	13.6	89.0	13.3	33.1	**8.7**

Table 5.15 – Best 25 solutions in terms of combined beamwidth from combined-objective GA

For reference each antenna simulated was given a unique number starting from 2000 (to avoid confusion with those from the previous GA. This unique number is shown in the first column of Table 5.15. At the right of the table bandwidth results have again been retrospectively calculated.

The antenna with the highest combined beamwidth is antenna No. 2656 which achieved a 97.7° beamwidth over which both the axial ratio and half-power criteria were met. The antenna has approximately 3.5 turns but is truncated to approximately 2.5 turns by taking off the uppermost turn. The exact parameters are given in Table 5.16.

N	C/λ	`end_point`	`end_point2`
3.44	1.25	0.99	0.47

Table 5.16 – Parameters for antenna No. 2656

Figure 5.8 shows the radiation hemisphere for this antenna. The CP region is seen to coincide with the half-power region over much of the hemisphere. There is an exception to this near $\phi = 300°$ where the CP region greatly exceeds the half-power region. It is almost exclusively the half-power region which defines the combined beamwidth of this antenna, except for a narrow region near $\phi = 0°$ where the CP region dips slightly below it, and so becomes the limiting factor.

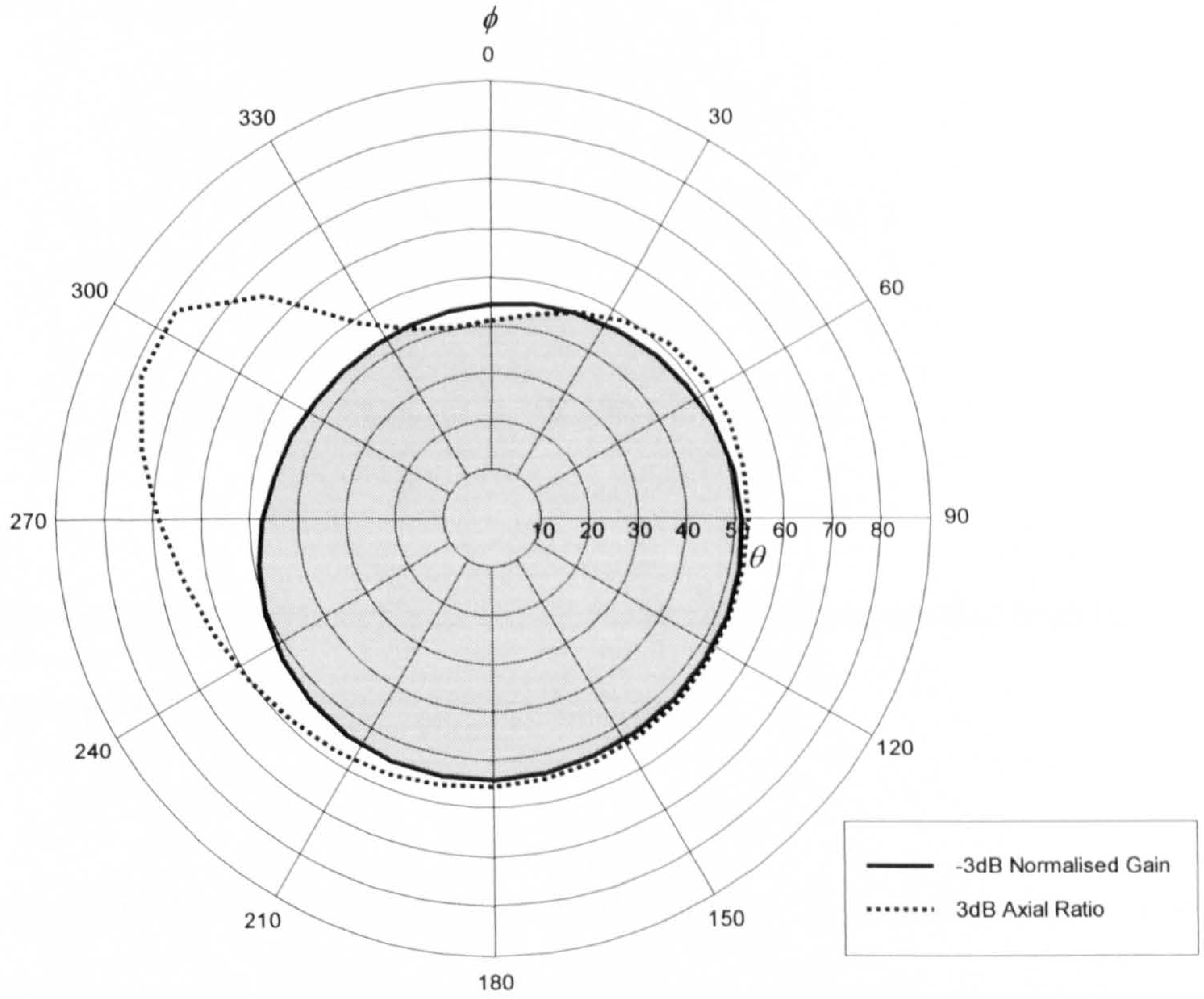

Figure 5.8 – Radiation hemisphere for antenna No. 2656

The combined region, shown shaded in Figure 5.8, is marginally greater than that of antenna No. 197 from the previous GA (Figure 5.7). The combined beamwidth of that antenna was just under 95° compared with 97.7° for this new antenna.

The disappointing feature of antenna No. 2656 is its low bandwidth. While its axial ratio and gain bandwidths are 8.2% and 29% respectively, its impedance bandwidth is just 2% and thus the limiting factor. Referring back to Table 5.15 it is possible to look for an antenna with better bandwidth performance at the expense of a slightly reduced beamwidth. Antenna No. 3507 is one such example. This antenna has an impedance bandwidth of 9.3%, which is a clear improvement, and a combined beamwidth of 95.6° which is only 2.1° lower than that of antenna No. 2656. The parameters of this antenna are given in Table 5.17.

N	C/λ	`end_point`	`end_point2`
3.49	1.38	0.89	0.31

Table 5.17 – Parameters for antenna No. 3507

Figure 5.9 shows the radiation hemisphere for this antenna, and shows that both the region of half-power and the region of CP vary with ϕ.

Figure 5.10 shows how the beamwidths vary with frequency. The combined beamwidth reaches 96° and maintains a value of at least 90° over a 6% bandwidth.

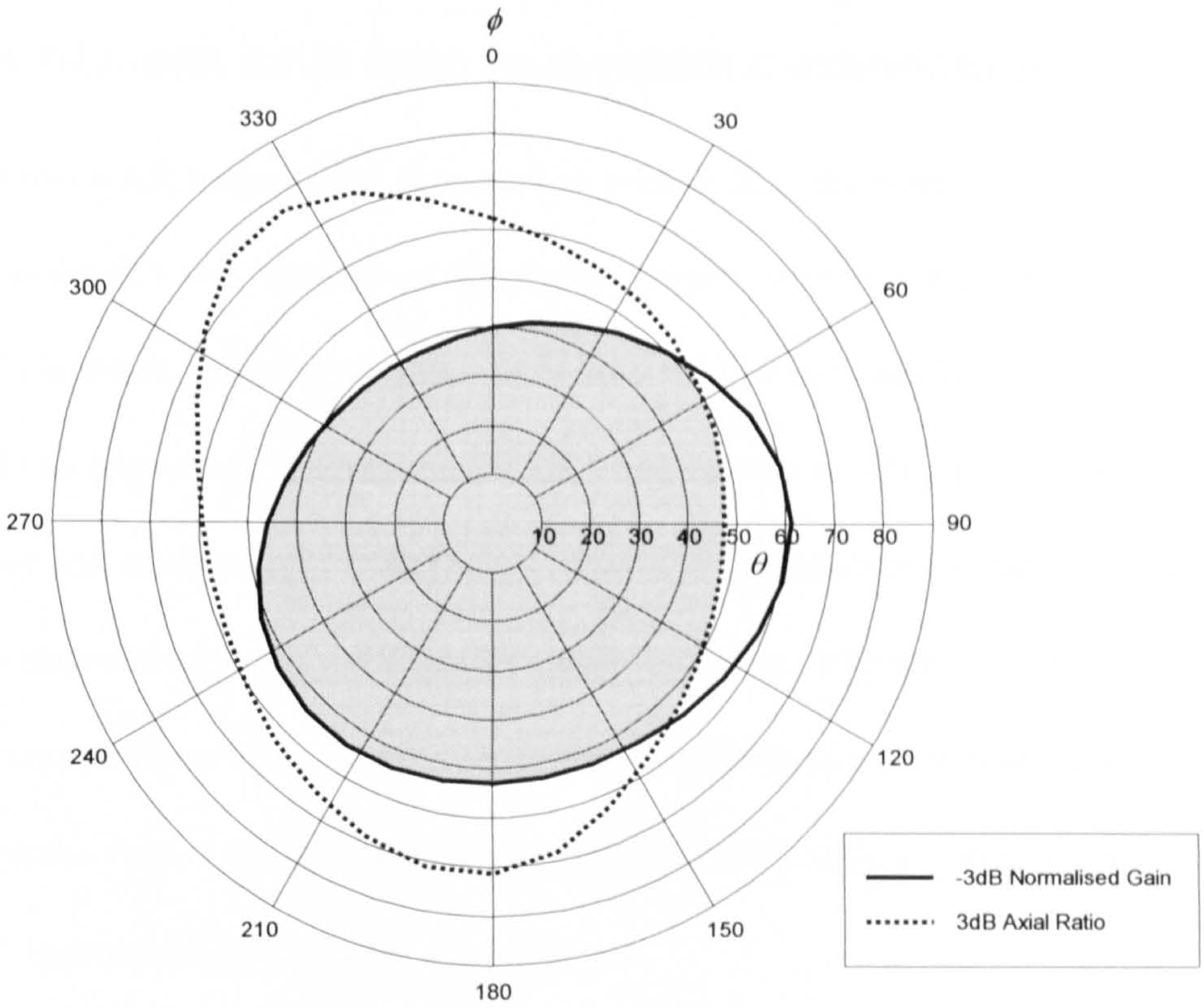

Figure 5.9 – Radiation hemisphere for antenna No. 3507, C=1.38λ

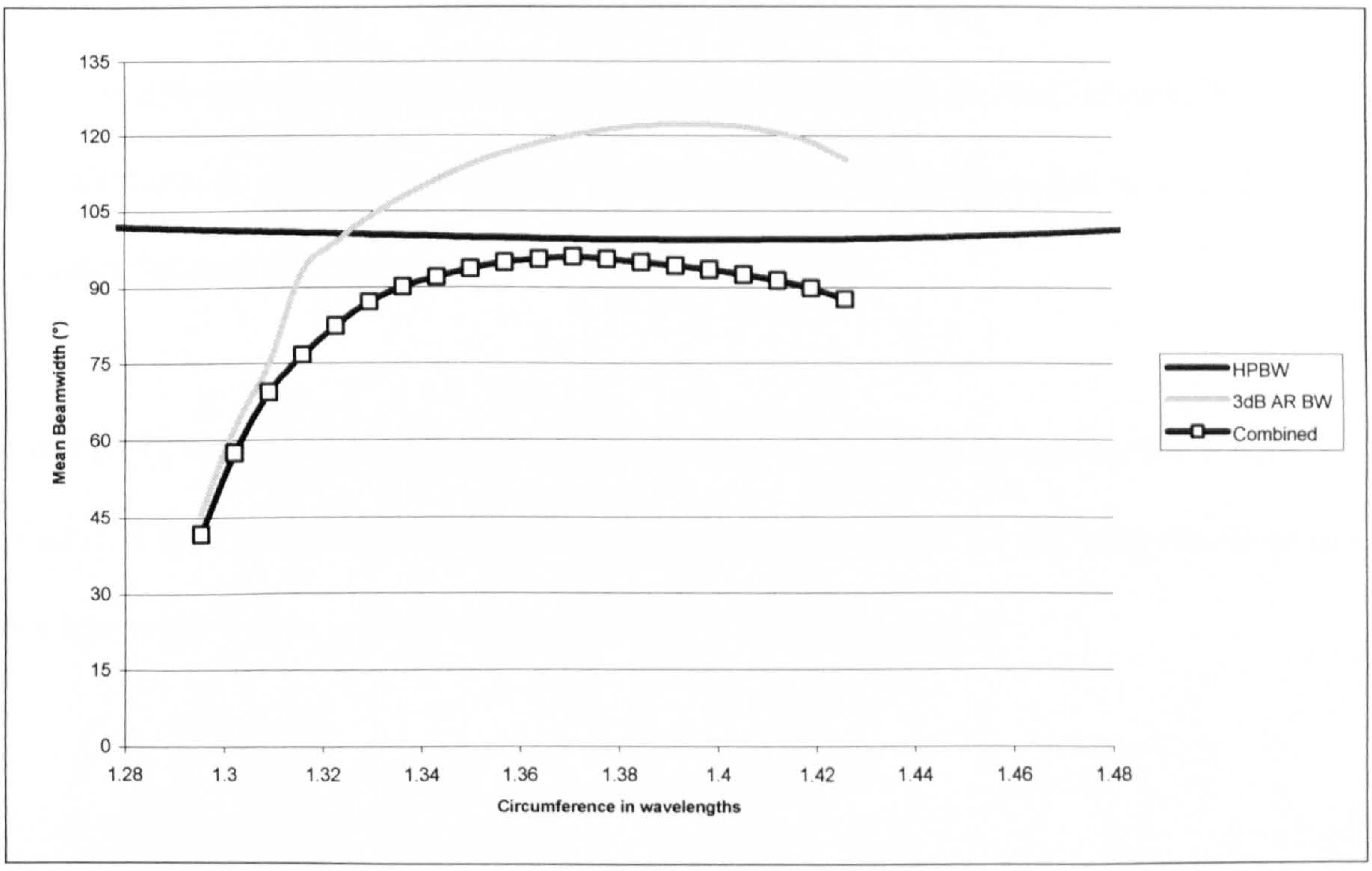

Figure 5.10 – Beamwidth variation with frequency for antenna No. 3507

5.7 Review of mean axial ratio beamwidth methodology

The concept of mean AR beamwidth, proposed in section 5.2, has been incorporated successfully into the GA as a measure of the angular region over which the antenna produces CP. It is worth considering quantitatively what this measure has achieved and whether it could be improved. Taking the 39 SHA geometries which produced an axial ratio of less than 3dB on boresight from the previous GA optimisation as sample data, it is possible to retrospectively apply alternative mean functions. Figures 5.11-5.14 over the page show comparisons between the values obtained for the mean AR beamwidth over 16 cuts and the values which would have been obtained for 8-, 4-, and 2- cuts and for a single AR beamwidth taken in the $\phi = 0$ plane.

It can be seen that the comparison between 16-cuts and 8-cuts, and between 16-cuts and 4-cuts show relatively little difference, particularly for the larger beamwidths which the GA was trying to find. The SHA-MoM code took around 30 seconds to calculate each radiation cut, so reducing the number from 16 to 4 would have saved approximately six minutes for each simulation.

Looking however at the comparisons in Figures 5.13 and 5.14, a large scatter is seen. If an averaging of at least 4 cuts had not been used, the values for AR beamwidth would not have been representative of the beamwidths for all the cuts.

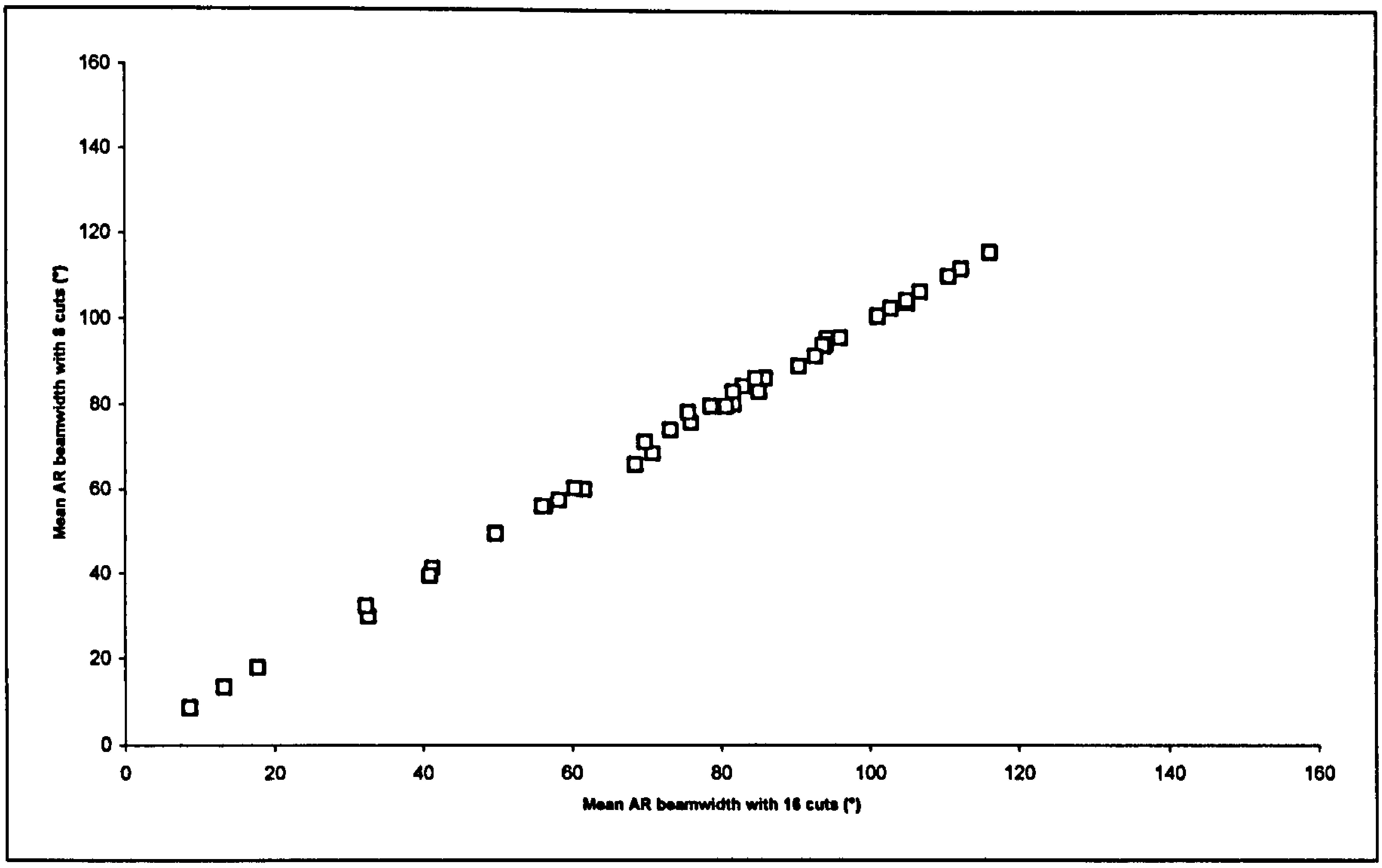

Figure 5.11 – Comparison between 16-cuts and 8-cut mean AR beamwith values

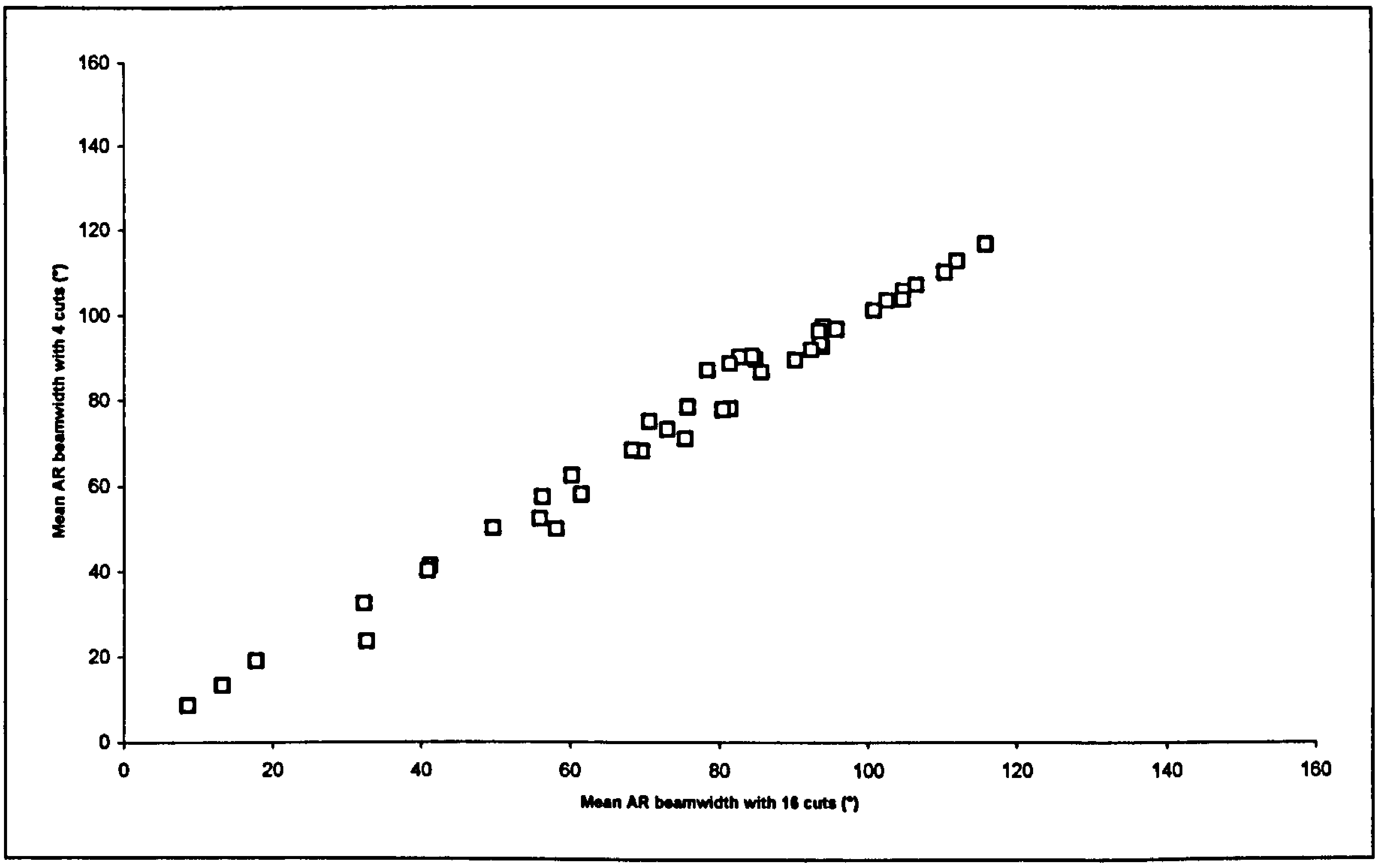

Figure 5.12 – Comparison between 16-cuts and 4-cut mean AR beamwidth values

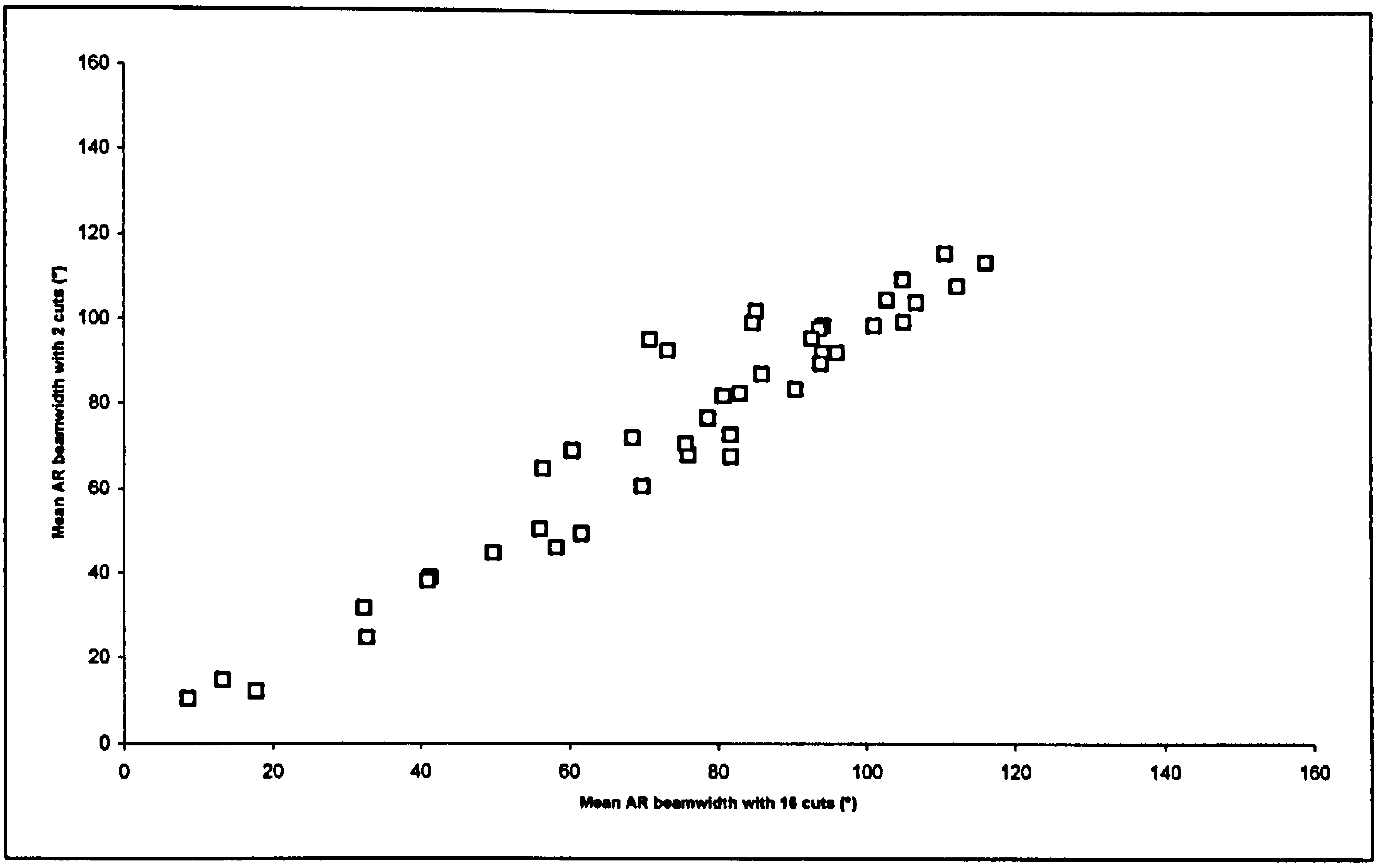

Figure 5.13 – Comparison between 16-cuts and 2-cut mean AR beamwidth values

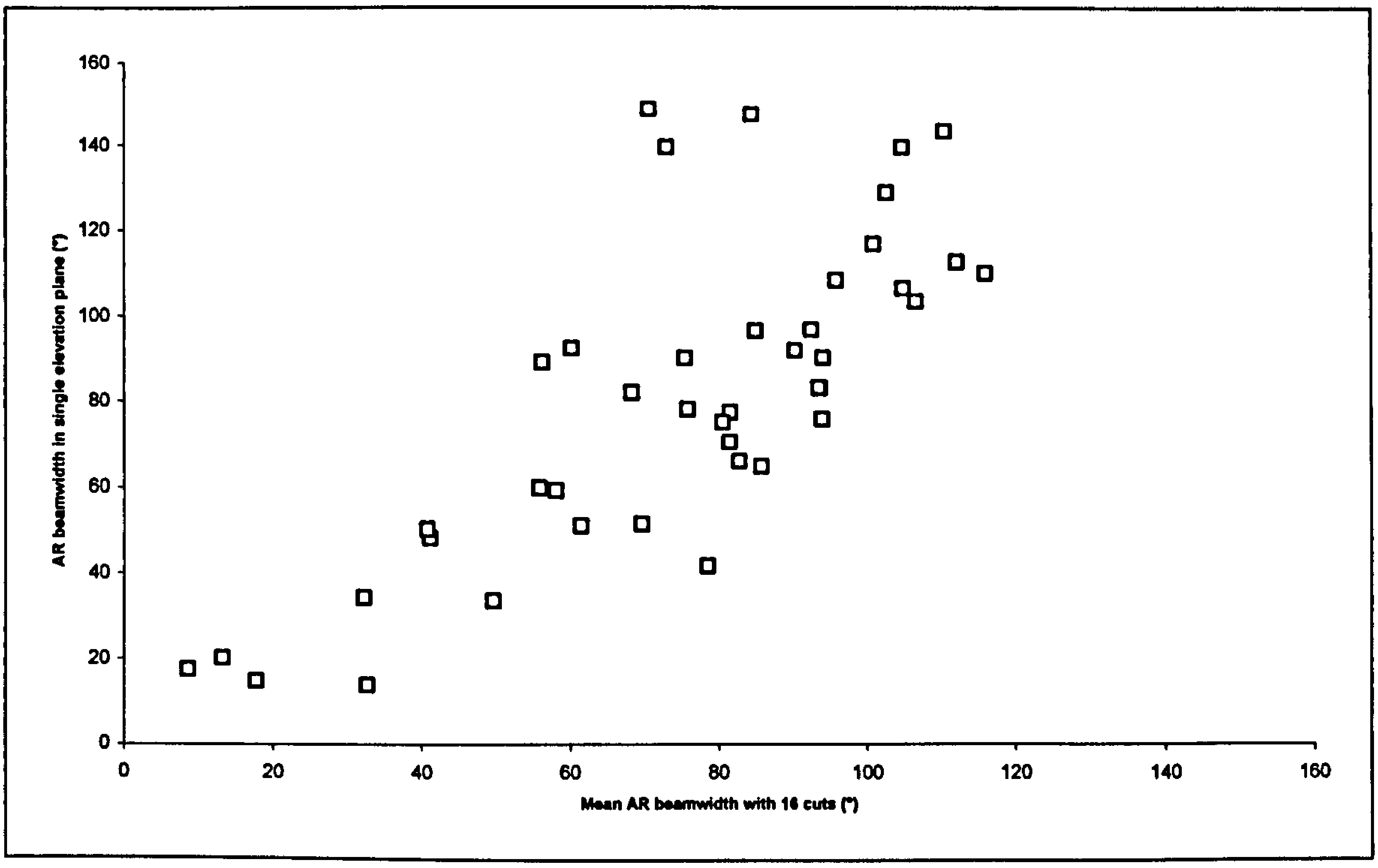

Figure 5.14 – Comparison between 16-cut mean AR beamwidth and AR beamwidth in one plane

5.8 Discussion

This chapter has presented results obtained from running a genetic algorithm a number of times. The GA's goals have been refined in order to address the optimisation problem in the best manner possible. These refinements have culminated in the definition of mean combined-beamwidth, which is the beamwidth where both the axial ratio and half-power criteria are satisfied, averaged over a number of cuts. This definition was needed to overcome the non-symmetric nature of the radiation patterns produced by the SHA, where both axial ratio beamwidth and HPBW vary with ϕ, and where neither of these separate beamwidths is the limiting factor for all values of ϕ.

The optimisations presented were non-specific, aiming for the "best" antenna rather than one which met certain criteria. If this was the case then the mean combined beamwidth might better be replaced with another measure, such as the minimum beamwidth. The criteria used to define the beamwidths, namely 3dB axial ratio and a normalised gain of -3dB, may also not be suitable for every application.

In addition to the beamwidth of the SHA, which has been the main focus of this research, the bandwidth of the antenna is also crucially important. A wide beamwidth is of no use unless the antenna can maintain this over a reasonable bandwidth. The antenna's other parameters, such as maximum gain and impedance, must also stay within their limits over the given bandwidth.

Although bandwidth was not incorporated into the GA, values for the various bandwidths have been retrospectively calculated for each of the solutions to the GAs.

Ideally the GA should calculate bandwidth at the time it models each antenna. In this way the GA could search for solutions with large bandwidths at the same time as searching for those with large beamwidths. The difficulty in incorporating bandwidth into the GA is the running time; calculating the bandwidth requires the antenna to be simulated at a range of frequencies instead of just one. This would have increased the running time of the GA, using the current version of SHA-MoM, from a matter of a couple of weeks, to several months. This problem could be rectified either by optimising the SHA-MoM code for faster simulations, possibly using interpolation techniques [11], or by running the GA on a supercomputing cluster. Unfortunately, neither of these solutions were possible within the timeframe of this research.

It is difficult to compare the antennas found by the GA to those obtained by other authors. Cardoso and Safaai-Jazi [3] reported a 3dB AR beamwidth of 90° but this was only given in one plane, and AR beamwidths in other planes may have been considerably higher or lower. The HPBW may also have been less than 90°. Antenna No. 3507 gave a maximum mean AR beamwidth of 122°. More importantly its combined beamwidth reached 96° and maintained a value greater than 90° over a 6% bandwidth.

References

1 J. Horn, N. Nafpliotis, and D. E. Goldberg, "A niched Pareto genetic algorithm for multiobjective optimization", Proceedings of the First IEEE Conference on Evolutionary Computation, 1994.

2 K. Deb, S. Agrawal, A. Pratap, and T. Meyarivan, "A Fast Elitist Non-dominated Sorting Genetic Algorithm for Multi-objective Optimization: NSGA-II", Proceedings of the 6th International Conference on Parallel Problem Solving from Nature (PPSN VI), pp. 849-858, Sep. 2000.

3 J. C. Cardoso and A. Safaai-Jazi, "Spherical helical antenna with circular polarisation over a broad beam", IEE Electronics Letters, vol. 29 (4), pp. 325-326, Feb. 1993.

4 A. Safaai-Jazi and J. C. Cardoso, "Radiation characteristics of a spherical helical antenna", IEE Proc-Microw. Antennas Propag, vol. 143, pp. 7-12, Feb. 1996.

5 H. T. Hui, K. Y. Chan, E. K. N. Yung, and X. Q. Shing, "Coaxial-feed axial mode hemispherical helical antenna", IEE Electronics Letters, vol. 35 (23), pp. 1982-1983, Nov. 1999.

6 E. Weeratumanoon and A. Safaai-Jazi, "Truncated spherical helical antennas", IEE Electronics Letters, vol. 36 (7), pp. 607-609, Mar. 2000.

7 H. T. Hui, K. Y. Chan, and E. K. N. Yung, "The input impedance and the antenna gain of the spherical helical antenna", IEEE Trans. Antennas Propagat., vol. 49 (8), pp. 1235-1237, Aug. 2001.

8 H. T. Hui, K. Y. Chan, and E. K. N. Yung, "The low-profile hemispherical helical antenna with circular polarization radiation over a wide angular range", IEEE Trans. Antennas Propagat., vol. 51 (6), pp. 1415-1418, Jun. 2003.

9 Y. Ding, J.-H. Qiu, and W.-Y. Qin, "A New Spherical Helical Antenna", IEEE APS Int. Symp., 2005, vol. 2A, pp. 292 - 295, Jul. 2005.

10 U. R. Kraft and G. Monich, "Main-beam polarization properties of modified helical antennas", IEEE Trans. Antennas Propagat., vol. 38 (5), pp. 589-597, May 1990.

11 K. L. Virga, Y. Rahmat-Samii, "Efficient wide-band evaluation of mobile communications antennas using [Z] or [Y] matrix interpolation with the method of moments", IEEE Trans. Antennas Propagat., vol. 47 (1), pp. 65-76, Jan. 1999.

6 Measurements

6.1 Introduction

In order to further validate the computer model and also to assess the feasibility of constructing Spherical Helical Antennas, a number of prototype antennas were manufactured. This chapter describes the steps taken to produce the prototypes, and presents results of the measurements performed.

6.2 Construction

Creating a spherical helical geometry to a defined mathematical curve poses an interesting challenge, both in terms of reproducing the exact curved shape, and for supporting the wire both during and after construction. Various solutions were considered and explored including wrapping a wire around a spherical object which could later be removed without deforming the wire, for example a balloon which could be burst, or wax which could be melted away. The use of a material with a low dielectric constant, such as expanded polystyrene, was also considered. The shape of the twin-armed SHA however lends itself to being constructed as two separate parts and then joined so the emphasis is on recreating exactly the mathematical curve. This was achieved through the construction of two hemispherical "moulds" which had grooves etched into them using a CNC milling machine. The two moulds were identical except that one was the mirror image of the other; this gave two curves which were identical except for being of the opposite sense.

6.3 Non-optimal prototype

The first prototype built was a 2-turn twin-arm SHA with a radius of 1.95cm. The antenna was constructed by wrapping 18SWG (1.25mm) tinned copper wire around the moulds following the grooves, then carefully prising it away to leave the desired curve. Semi-rigid coax was then used to connect the feed point of the antenna to an SMA connector. Figure 6.1 and Figure 6.2 show one of the moulds and the completed antenna.

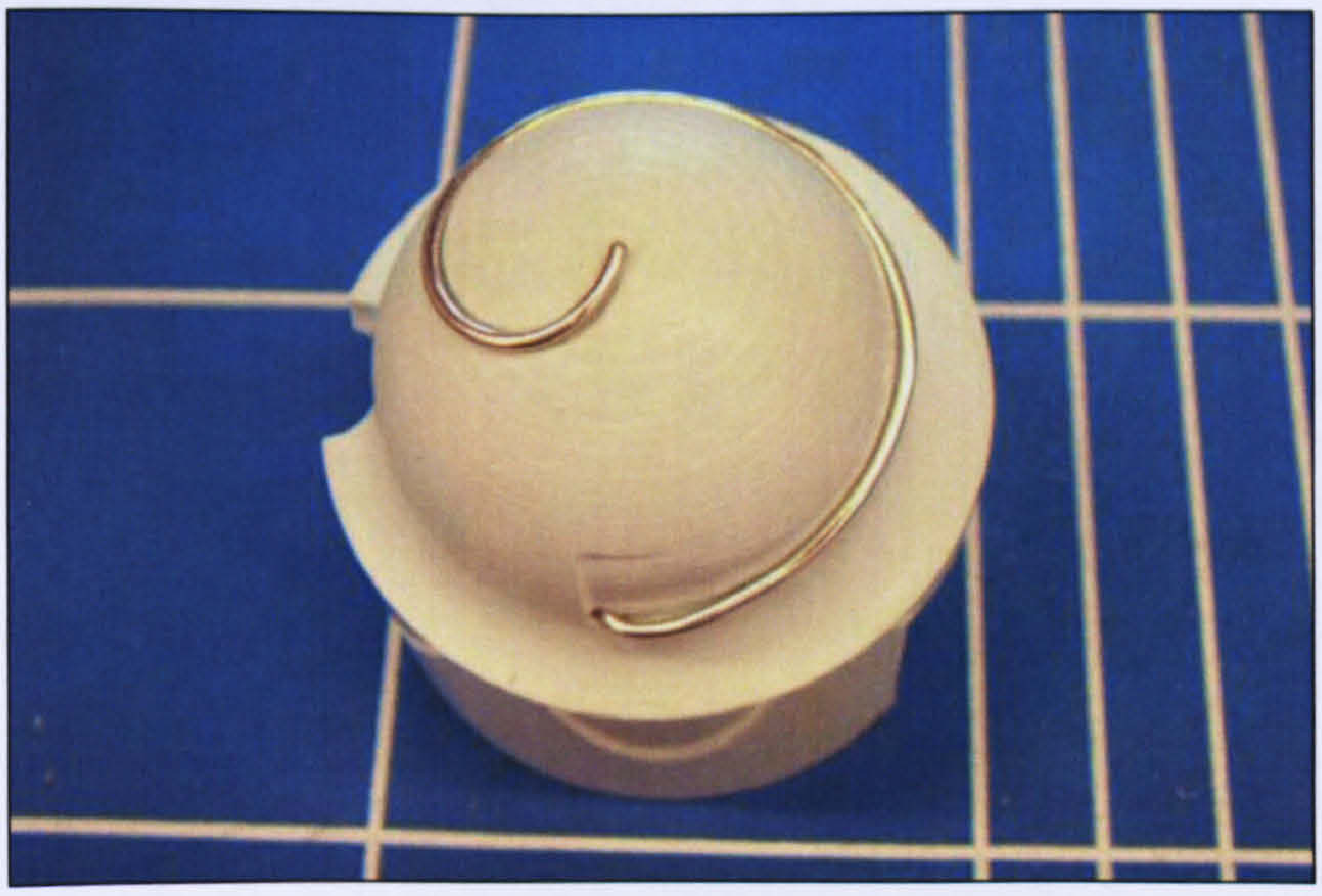

Figure 6.1 – Photograph of one of the two moulds

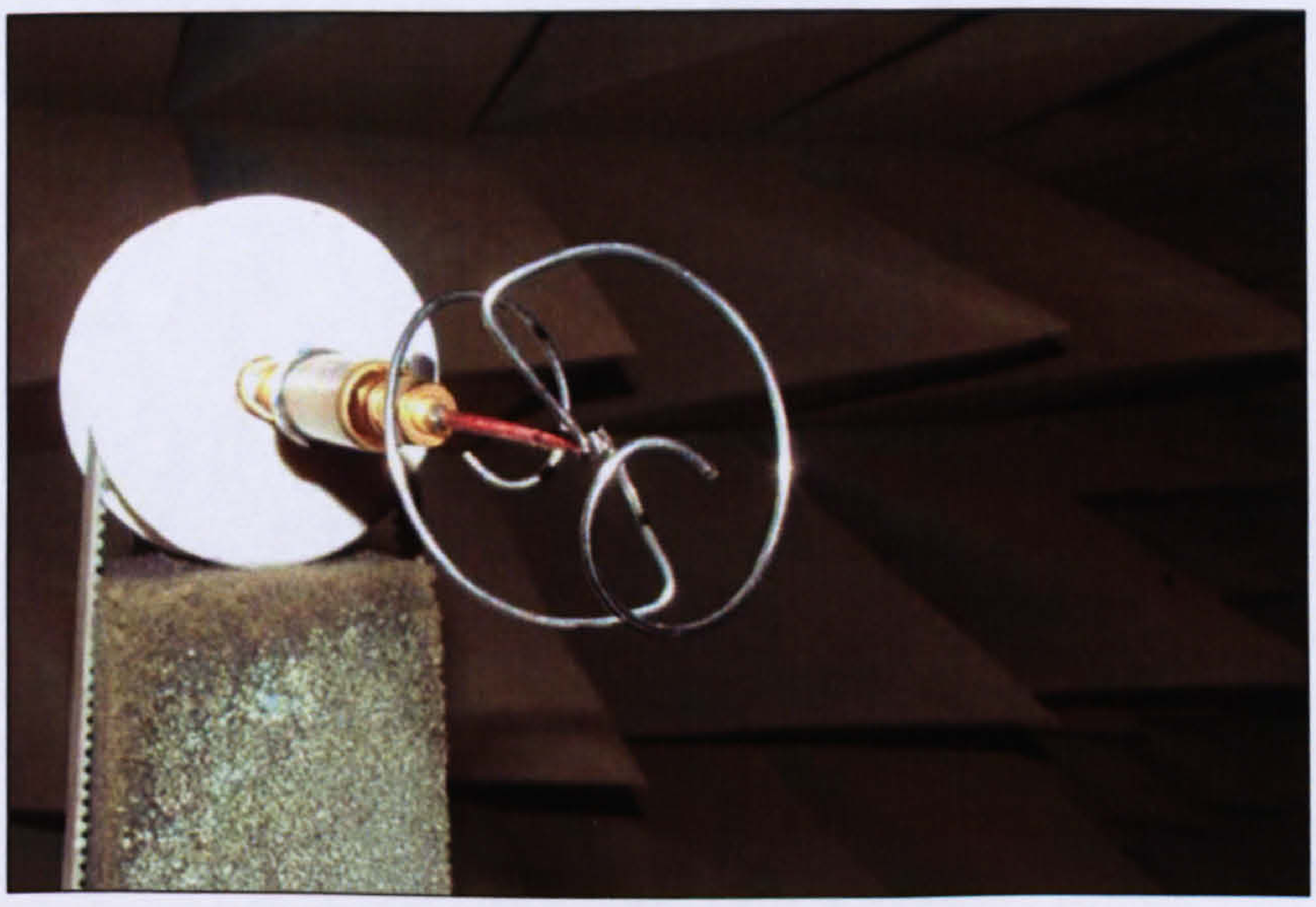

Figure 6.2 – Photograph of prototype SHA in anechoic chamber

To connect the balanced antenna to an unbalanced coaxial cable, a balun was required; for simplicity a sleeve balun was used. Far-field measurements were then taken in the anechoic chamber. Unfortunately these measurements showed significant coupling between the antenna and the positioner used to rotate the antenna, and this coupling prevented satisfactory results from being taken. In order to overcome this, it was decided to mount the antenna against a ground plane

6.4 Addition of ground plane

A printed balun was designed using Sonnet Lite and is shown in Figure 6.3. The balun consists of a tapered T-junction to split the power equally along two tracks. The lengths of these feed lines differ by half a wavelength resulting in a phase shift of 180° for one of the paths. As a result of this, the balun is inherently narrowband so two separate baluns, each with a different centre frequency, were printed onto the board. Selection between these two frequencies could then be performed simply in the lab by swapping the SHA between the two. The balun was printed onto an FR4 substrate.

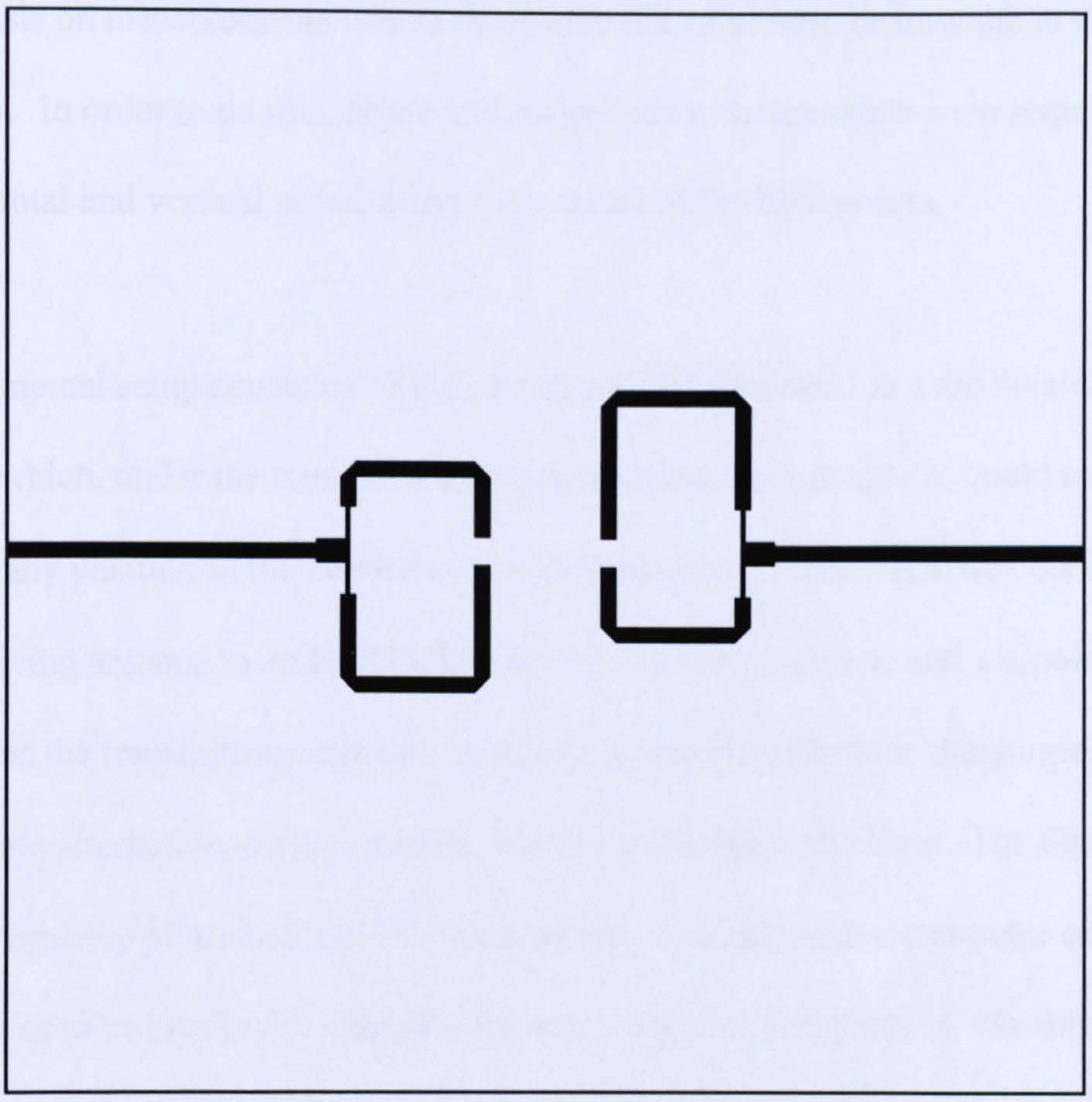

Figure 6.3 – Layout of printed balun

Figure 6.4 shows a photograph of the completed prototype.

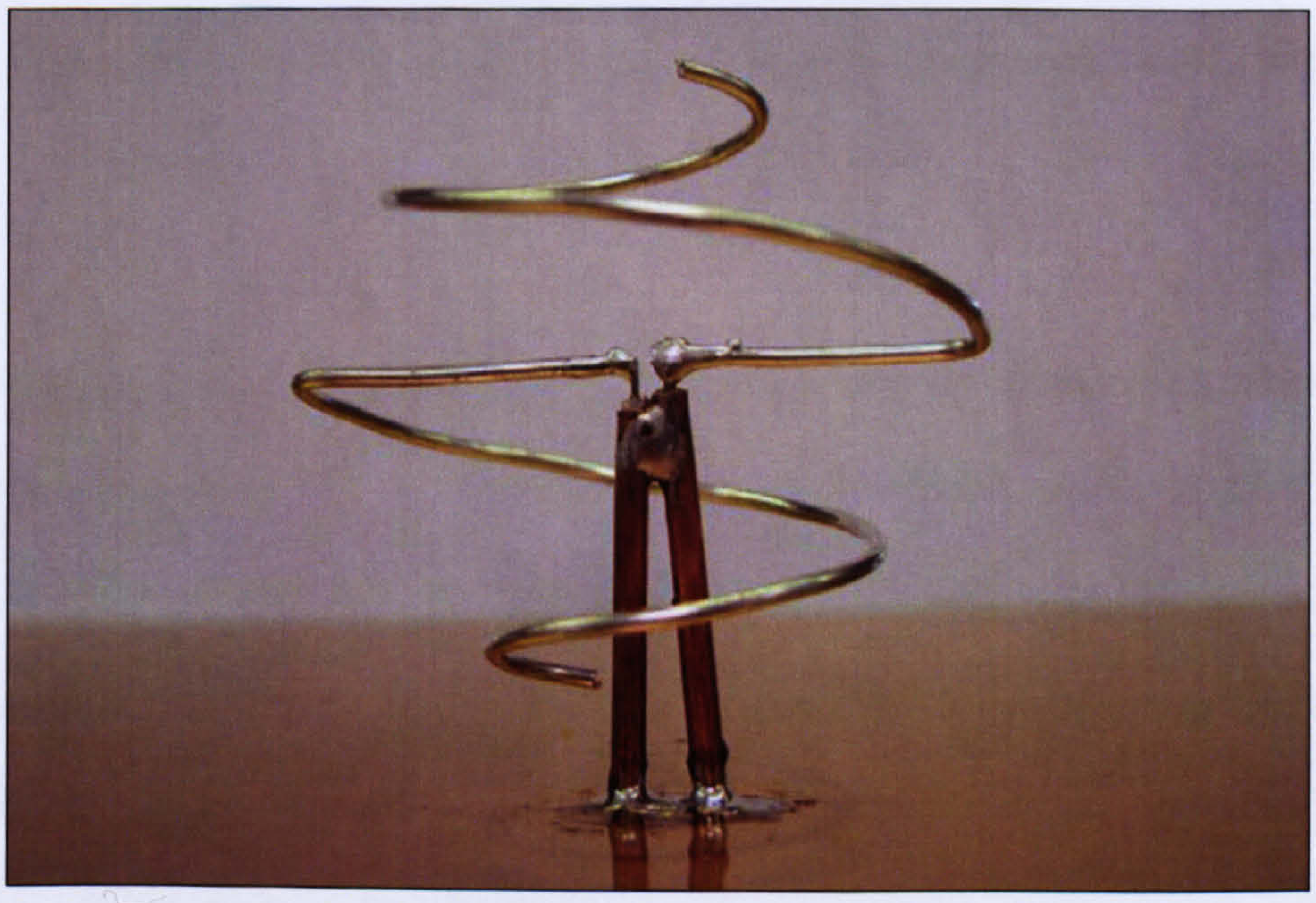

Figure 6.4 – Photograph of prototype SHA mounted 5mm above a ground plane

The emphasis on measurements was to determine the axial ratio beamwidth at different frequencies. In order to do this, phase and magnitude measurements were required for both horizontal and vertical polarisation for a series of far-field points.

The experimental setup consisted of the prototype SHA mounted to a mechanical positioner which, under the control of a proprietary computer program, could rotate the antenna to any position in the azimuth and elevation planes. The SHA was connected as the receiving antenna to an HP8753D Vector Network Analyser, and a dipole was connected as the transmitting antenna. A dipole is less than ideal for this purpose but a more suitable alternative, such as a horn, was not available at the time. The dipole had a resonant frequency of around 2.2GHz and was also rotatable under computer control in such a way as to transmit with either horizontal or vertical polarisation. By rotating the two antennas accordingly, the software then took magnitude and phase measurements at 15°/15° intervals over the complete spherical far-field, for the two orthogonal polarisations. The frequency range over which measurements could be taken was limited by the printed balun and the transmitting dipole, and was chosen to be 2.75 GHz – 3 GHz. Two sets of measurements were taken to verify the reproducibility of the results.

Figure 6.5 shows the axial ratio on boresight over the range of frequencies. There is some variation between the two sets of results and the predicted values, which shows the difficulty of calculating axial ratio values from experimental data. However, both sets of results show that the axial ratio remained below 3dB at all the frequencies tested, which indicates that reasonable CP was being produced.

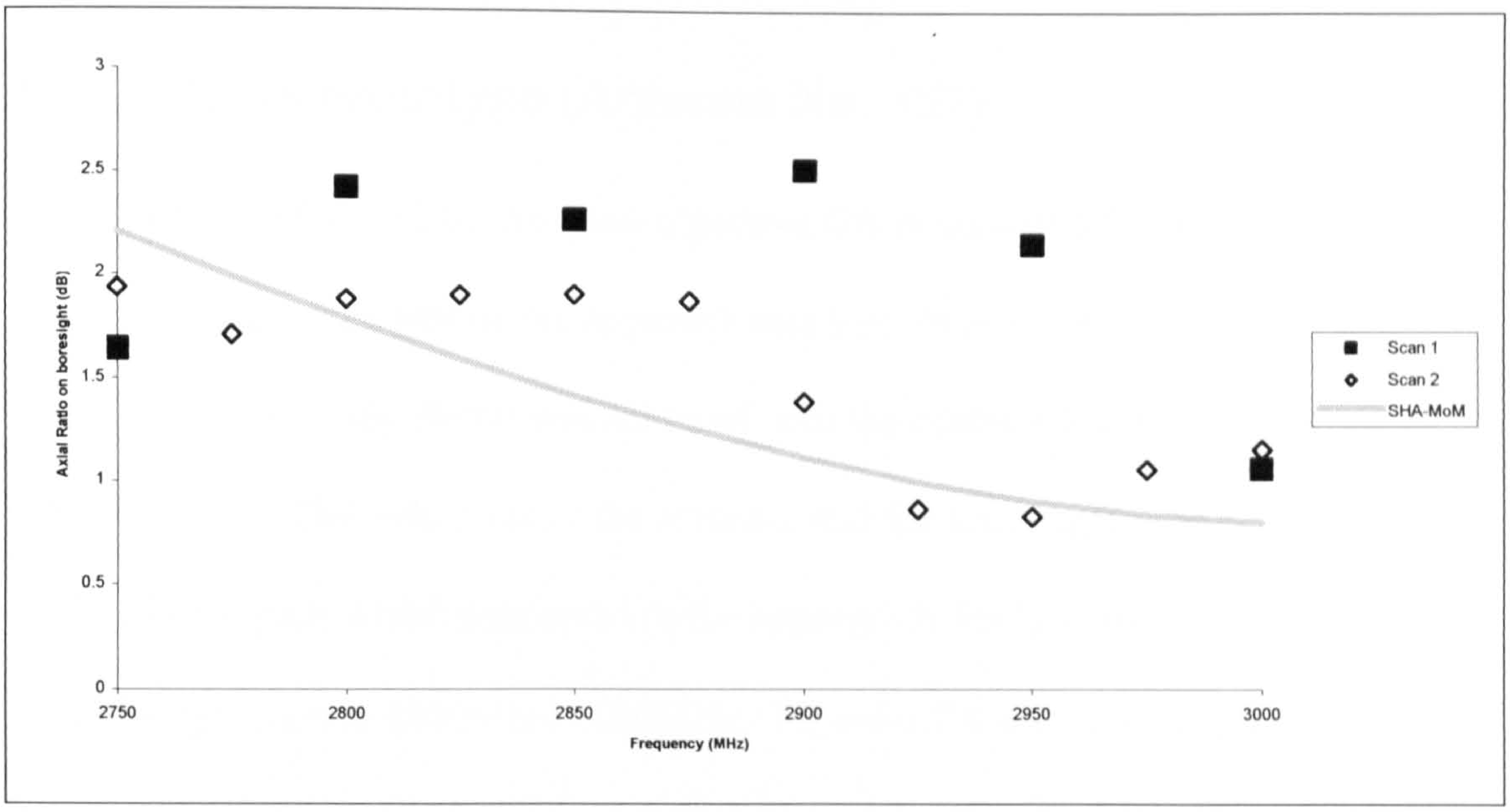

Figure 6.5 – Axial ratio on boresight over a range of frequencies

The anticipated properties of the SHA are that it can produce good CP over a wide beamwidth. Figure 6.6 shows the measured beamwidth for which the axial ratio stayed below 3dB. Beamwidths were determined for each of the 12 elevation planes measured, and the graph shows an average of these values. With the exception of one frequency point, a much better agreement is seen between the two sets of data, though this varies slightly from the modelled values.

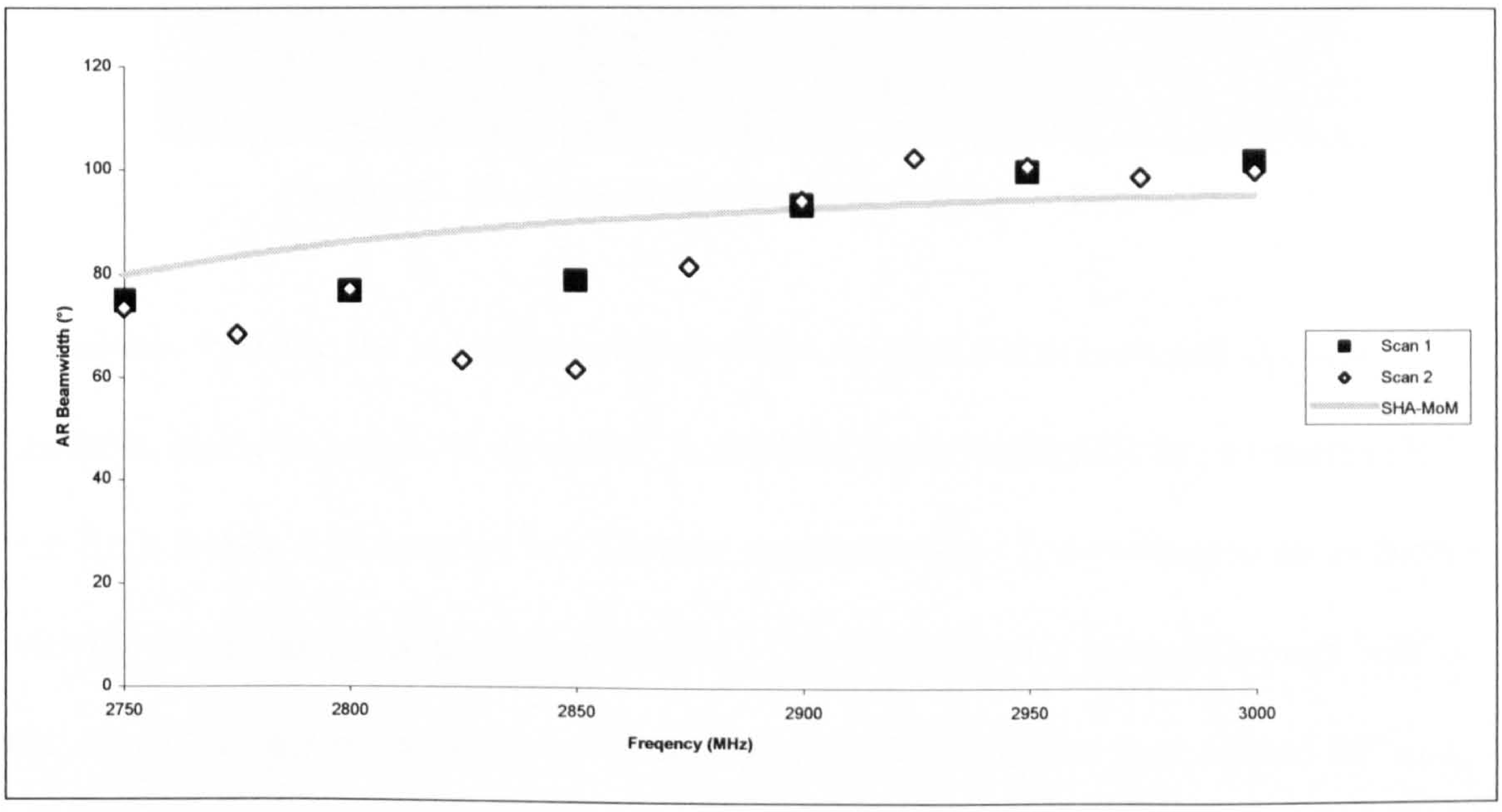

Figure 6.6 – 3dB Axial ratio Beamwidth over a range of frequencies

6.5 Optimal prototype (Antenna No. 197)

Antenna No. 197, found by the quad-objective GA in section 5.5, was also constructed as a prototype, but an alternative approach was used to provide a balun. For this antenna a Murata Chip Balun was soldered onto the centre a small PCB approximately 2.5cm by 2cm. The twin arms of the antenna, and the semi-rigid coax feed were then soldered onto pads which connected to the appropriate leads of the chip. The balun is rated for operation at 1800MHz ±100MHz. Figure 6.7 shows a photograph of the antenna.

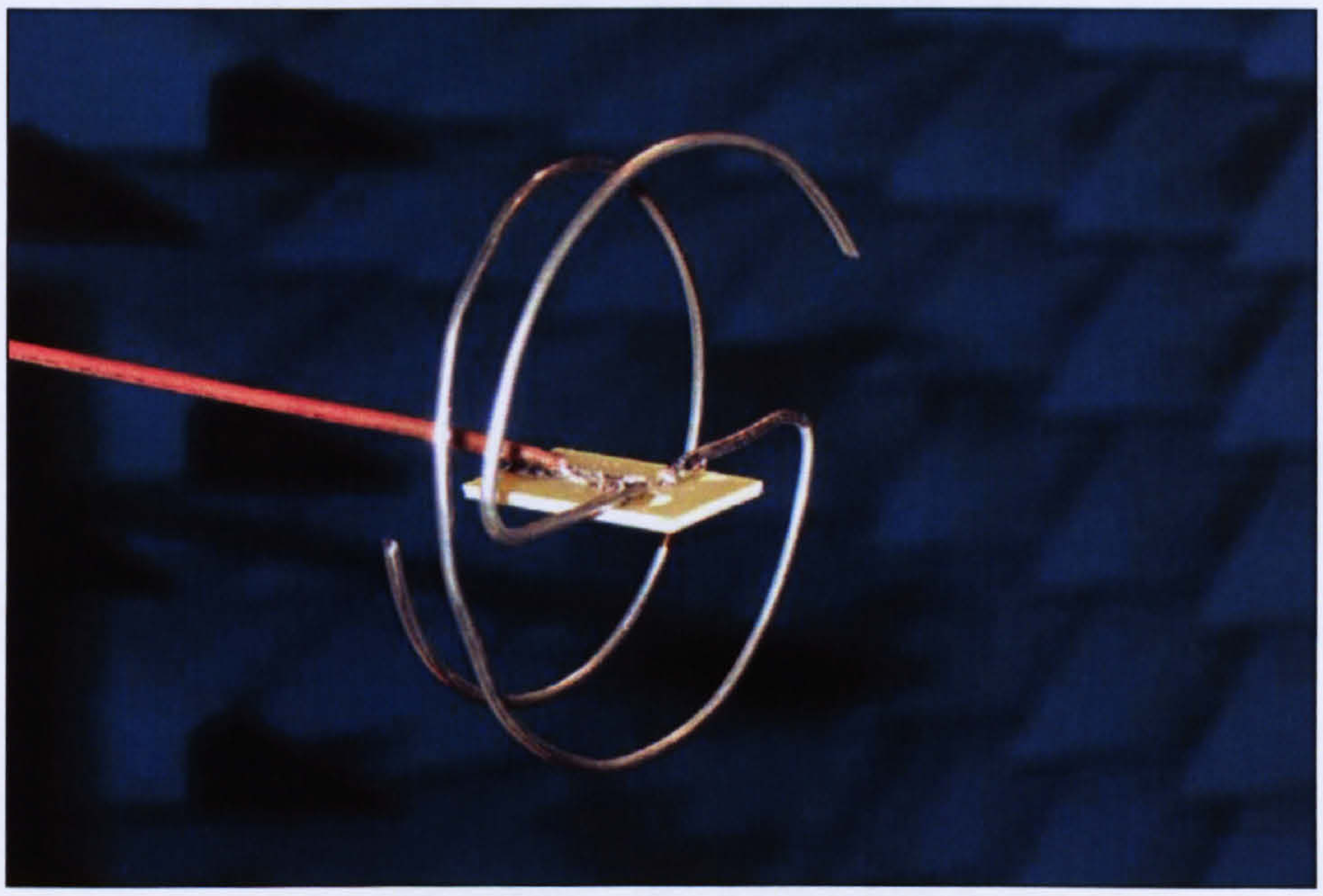

Figure 6.7 – Prototype of Antenna No. 197 in anechoic chamber

In order to measure the radiation patterns of the antenna it was mounted above a turntable inside an anechoic chamber. A double-ridged waveguide horn antenna (HF-906 from Rohde & Schwartz) was situated approximately 15 wavelengths away from it, with the two antennas connected to a VNA. The turntable was rotated through 360° with the S_{12} values being recorded for each angle. The horn was then rotated 90° and the measurements repeated; this allowed both E_θ and E_ϕ values to be obtained. Phase readings were recorded alongside amplitude measurements so that axial ratio calculations could later be performed. Figures 6.8 – 6.9 show the predicted and measured radiation patterns for the antenna at 1.8GHz.

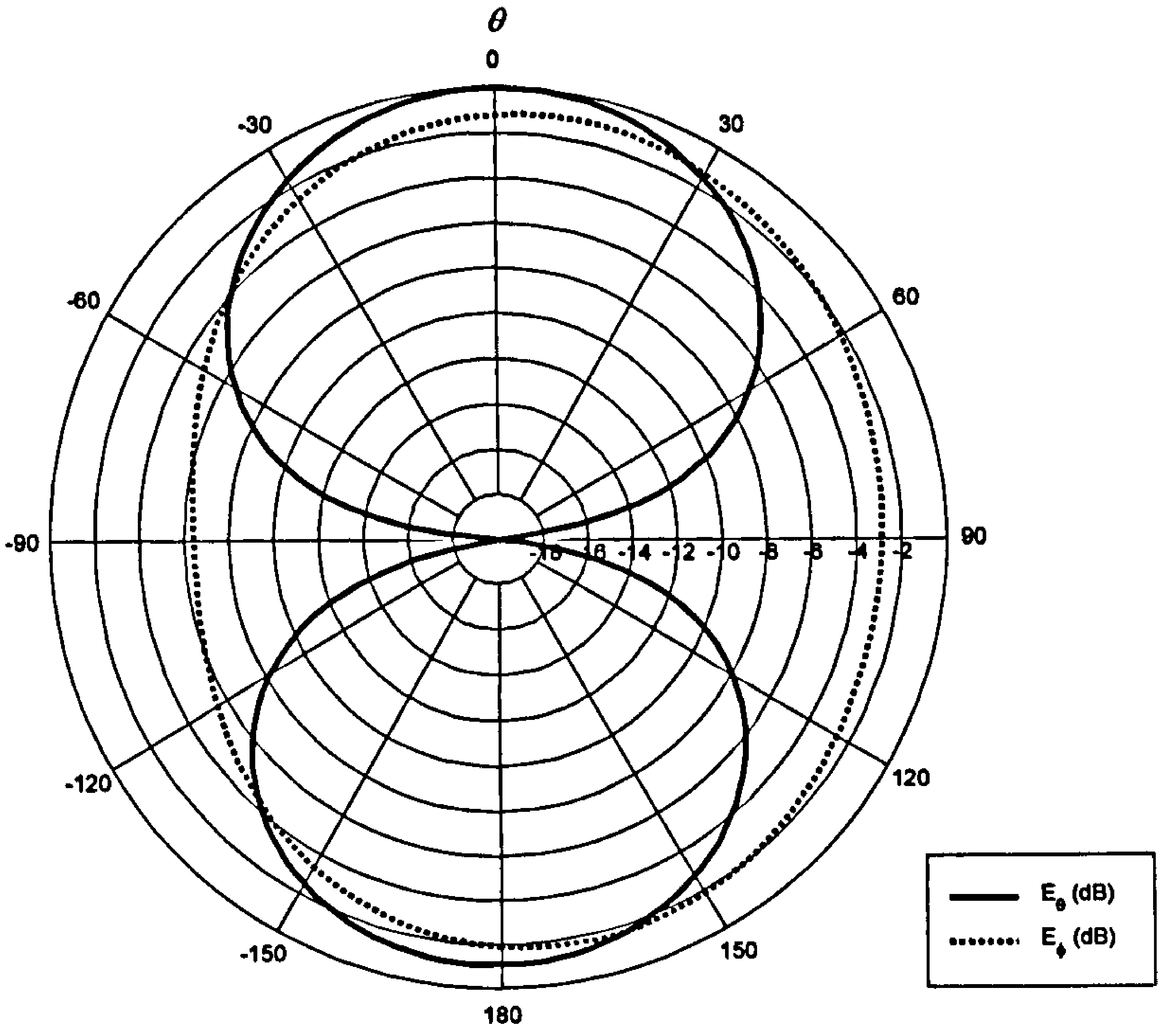

Figure 6.8 – Radiation pattern of Antenna No. 197 modelled with SHA-MoM (1.8GHz, *φ = 0°*)

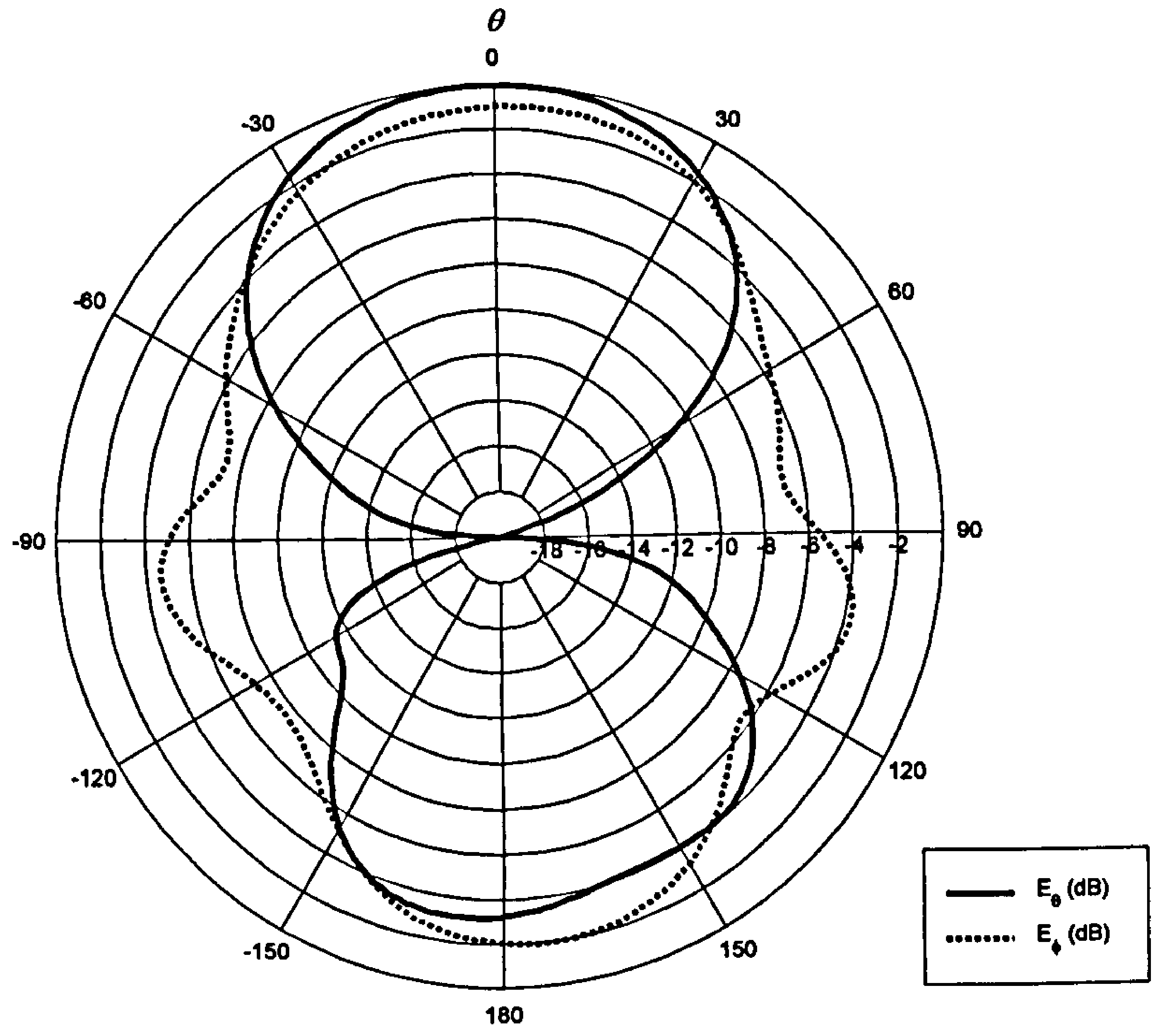

Figure 6.9 – Measured radiation pattern of Antenna No. 197 prototype (1.8GHz, *φ = 0°*)

The radiation patterns in Figures 6.8 – 6.9 show strong correlation, particularly in the region of interest ($-60° < \theta < 60°$). The measured results near the back of the antenna ($\theta \approx 180°$) have been distorted slightly due to the turntable obstructing the path between the two antennas. The slight ripples in the E_ϕ values around $\theta = \pm 90°$ are thought to be due to the presence of the PCB and chip balun at the centre of the antenna. Close to $\theta = \pm 90°$, where the antenna is side-on to the horn, the PCB obstructs the radiation from the furthest side of the antenna.

Figure 6.10 shows the computed and measured axial ratio characteristics of the antenna. According to the SHA-MoM simulation, the 3dB AR beamwidth in the $\phi = 0°$ plane should be 117°. This compares favourably with the measured value of 112°.

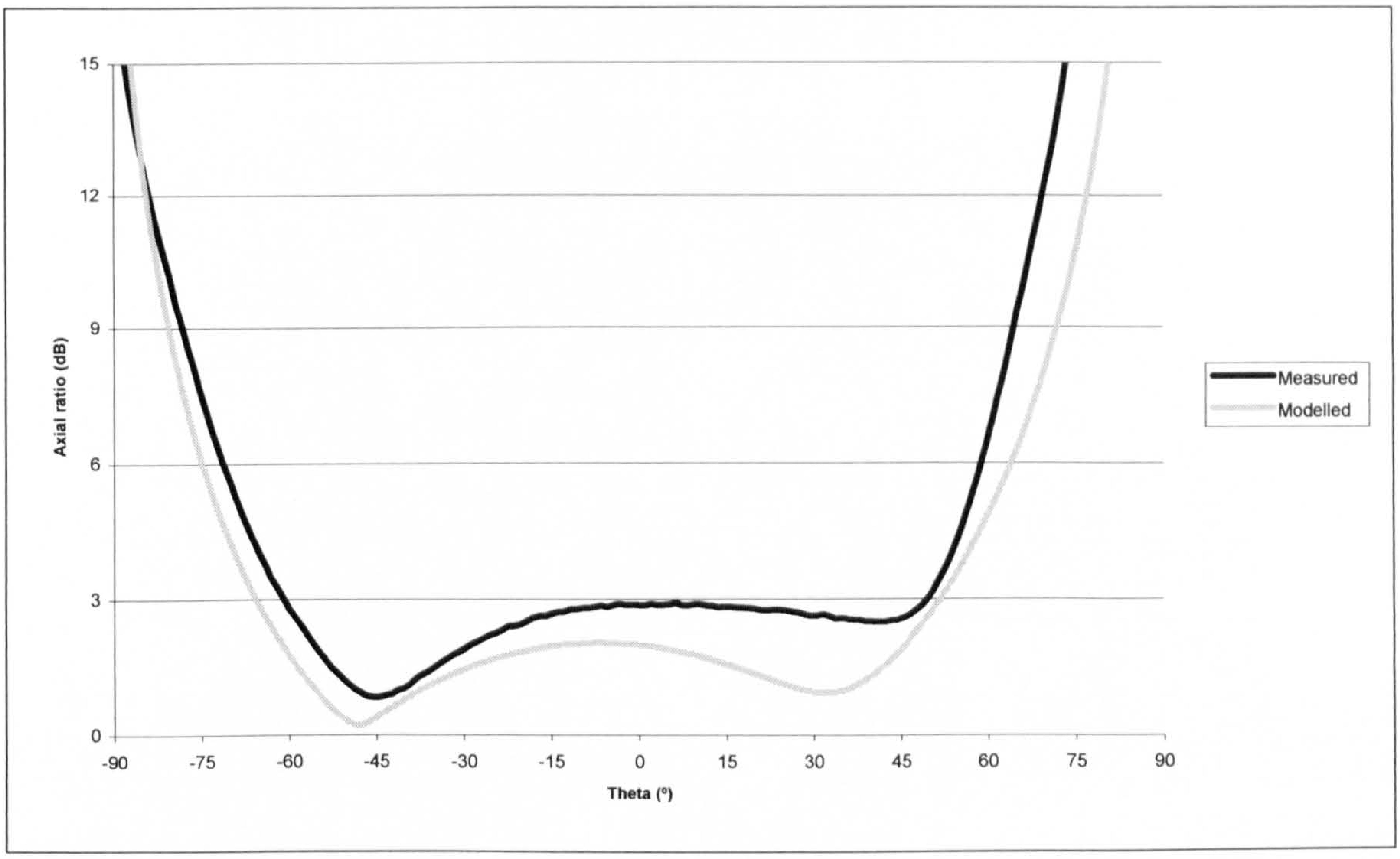

Figure 6.10 – Comparison of measured and modelled axial ratio characteristics of Antenna No. 197 (1.8GHz, $\phi = 0°$)

6.6 Discussion

This chapter has given details of how prototype SHAs were built and has presented the results of the measurements taken on the prototypes. The results have shown that the antenna is capable of producing acceptable circular polarisation over a wide beamwidth. Furthermore the measurements have provided additional validation for the modelled results given in the previous chapter.

The construction of a prototype highlighted the inevitable fact that the antenna is mechanically very fragile; although satisfactory for careful handling in the lab, it would need to be made stronger and more robust for any real-world application. This could be done by wrapping the wire around a dielectric former which is then left in place.

7 Conclusions

7.1 Introduction

In this chapter the research which has been conducted will be reviewed and critically discussed. Key aspects of the work, and in particular the novel contributions, will be highlighted. Finally, ideas for further work will be presented.

7.2 Summary of research

The research described in this thesis has centred on the spherical helical antenna. This antenna, which has received little attention in the scientific journals, is capable of providing circular polarisation over both a wide bandwidth and, more unusually, a wide beamwidth. This is a useful property for many applications, particularly those where signal must pass between Earth and space, for example satellite communications and space telemetry. The nature of these applications often requires an antenna with large angular coverage such that signals can be transmitted or received over the entire radiation hemisphere. Signals which pass through the ionosphere undergo Faraday rotation and so circular polarisation is essential to minimise path losses. Cylindrical helix antennas and spiral antennas, although producing circular polarisation in the boresight direction do not maintain this in off-axis directions. In this thesis, several novel modifications to the SHA have been proposed and these have been shown to improve its performance.

In Chapter 2 an equation was developed which calculates the mutual impedance between two arbitrarily curved segments. The equation is unusual in that it avoids having to differentiate the Green's function. Instead, it requires only two expressions – the angle between the tangents at any two specified points, and the distance between them. The equation is therefore applicable to any free-space geometry whether it consists of linear wires, curved wires, or a mixture of the two.

This equation for the impedance between two curved segments was then used in the custom FORTRAN code, SHA-MoM, which has been written as part of this research. SHA-MoM applies the Method of Moments to the spherical helical geometry and calculates current distributions, far field patterns, and impedance characteristics. Of particular importance is the calculation of axial ratio values which give a measure of the quality of circular polarisation. The code was rigorously validated in Chapter 3 against both published material and NEC. Good agreement was shown.

The SHA-MoM code uses curved segments, which have been shown to reduce the number of segments needed for a particular geometry, thus reducing computational requirements, whilst maintaining accuracy. Curved segments have not been widely used in the literature and can be considered novel. To the best of this author's knowledge, when the SHA-MoM code was written, curved segments had not been applied to a non-planar geometry by other authors. The efficiency afforded by the curved segment technique, without any loss of accuracy was of utmost importance when the code was used as part of an optimisation algorithm, and thus executed hundreds or thousand of times.

Various antenna geometries based on the spherical helix have been investigated using the SHA-MoM code, and the results have been presented in Chapter 4. These geometries have modified the SHA from the forms seen previously in the literature, and many of the modifications have led to improved performance, particular in terms of the axial ratio, the bandwidth, the half-power beamwidth, and the axial ratio beamwidth.

A novel scheme for specifying the separation between turns has been proposed. This new spacing technique, referred to as constant circumferential spacing (CCS), gives rise to a spherical helix which appears more uniformly spaced irrespective of the angle from which the antenna is viewed. Previously, only a constant vertical separation (CVS) geometry had been considered in the literature. The CCS scheme was shown to give lower values of axial ratio and wider AR beamwidths when compared to the CVS geometry. To illustrate this improvement a 7-turn SHA with the proposed CCS spacing was compared to a similar antenna with CVS spacing. The CCS geometry improved the minimum axial ratio from 2.6dB to 0.4dB whilst increasing the 3dB AR beamwidth at these frequencies from 58° to 107°. A further improvement was seen in the input characteristics of the antenna. The CCS scheme gave a smoother frequency response with fewer oscillations. This would enable the antenna to be matched over a wider bandwidth.

Spherical helical antennas with non-integer numbers of turns have also been considered. It was shown that the unnecessary restriction of allowing only an integer number of turns could potentially discard an antenna with useful properties. An example was given for a SHA with CVS spacing and a normalised circumference of 1.125λ. Here the axial ratio on boresight for 2- and 3- turns was above 2dB but this improved to below 1dB if 2.4 turns were used. It is particularly important when using an optimisation algorithm that the parameter space is a large as possible in order to maximise the chance of success.

A further enhancement to the original SHA was the proposal of a balanced twin-arm geometry in Chapter 4. This geometry, which is unique to this research, can be used without a ground plane thus decreasing the directivity of the antenna, and increasing its half-power beamwidth. An antenna which radiates CP over a wide beamwidth is of little use if the magnitude of the radiation at the edges of the AR beamwidth is not sufficiently high. An increase in the half-power beamwidth is therefore greatly beneficially to the pursuit of an antenna with large CP coverage.

In Chapter 5 a genetic algorithm was used to seek truncated twin-arm geometries with optimal performance. This is the first time a spherical helical antenna has been optimised using a search algorithm. Various algorithms were investigated and the one with the fastest convergence was selected. Various schemes were presented including dual-objective and quad-objective algorithms to search for the best axial ratio beamwidth with highest gain. Due to the significant variations in axial ratio over the radiation hemisphere, the use of a single axial ratio beamwidth was deemed unsuitable. An alternative measure of CP coverage was proposed: the mean axial ratio beamwidth. This average value of axial ratio beamwidth was calculated using the data from 16 separate radiation cuts. The choice of 16 was somewhat arbitrary and was subsequently reviewed using data obtained during the optimisation process. The comparison of the mean values obtained from 16 cuts was compared with the values that would have been calculated if the number of cuts was reduced. It was shown that 4 cuts was the best choice when considering both accuracy and computational complexity.

By applying the GA to the SHA, a truncated twin-arm antenna was found which produces circular polarisation over a beamwidth of 116°. This is substantially greater than those reported previously for the conventional SHA which at best gave an AR beamwidth of 90°.

Finally in Chapter 7, methods of constructing SHA antennas were considered and measurements from prototype twin-arm SHAs were given. The manufacturing of a spherical helical geometry to a defined mathematical curve poses an interesting challenge, both in terms of reproducing the exact curved shape, and for supporting the wire both during and after construction. A solution to this difficulty was presented in the form of a hemispherical "mould" which had been milled using a CNC lathe to cut a defined groove. A wire could then be wrapped around this mould, following the groove, to take on the intended curve before removing the mould. The design of a suitable feed network for the twin-arm geometry was also discussed. Radiation measurements from the prototype showed that even a non-optimal twin-arm SHA is capable of providing circular polarisation over a wide beamwidth.

7.3 Further work

The prototype antenna was fragile. In practice the antenna would have to be left on a dielectric former or have a radome cover (or both) for support. This would of course change the characteristics of the antenna. The Method of Moment analysis presented in this thesis is valid only for antennas in free-space, but could be extended to include dielectric substrates and superstrates in the model.

A further modification to the SHA would be that of non-uniform scaling, such that the antenna could be scaled by different amounts in each of its three axes. The resulting antenna would then be an ellipsoidal helical antenna.

The characteristic single lobe with no side lobes and low back radiation coupled with a relatively high axial gain makes the SHA and its variations suitable as an array element. This could be investigated further.

In the review of relevant literature at the beginning of this thesis, reference was made to the use of a GA not simply to optimise the parameters of an antenna, but to design a new type of antenna from scratch. The curved segment code used in this thesis is already capable of modelling arbitrarily curved segments. It would be interesting therefore to give a GA the complete freedom to design an antenna from curved segments. For mechanical stability it would be useful to constrain the curved segments to be conformal to some surface, though the shape of this surface could also be controlled by the GA.

Appendix A

Expressions defining the SHA geometries

A.1 Introduction

This appendix shows the development of various equations necessary to allow the Method of Moments to be applied to the Spherical Helical Antennas described in this thesis. Equations are presented for both the CVS and CCS spacing schemes. For a given point on the helix it is necessary to calculate its position vector and the tangent to the wire at that point. Between a given pair of points (source and observation), their straight-line separation distance and the vector dot product of their tangents are required. Finally an expression which gives the curved length of the antenna between any two points is also needed.

The coordinate system used throughout this thesis is as shown below:-

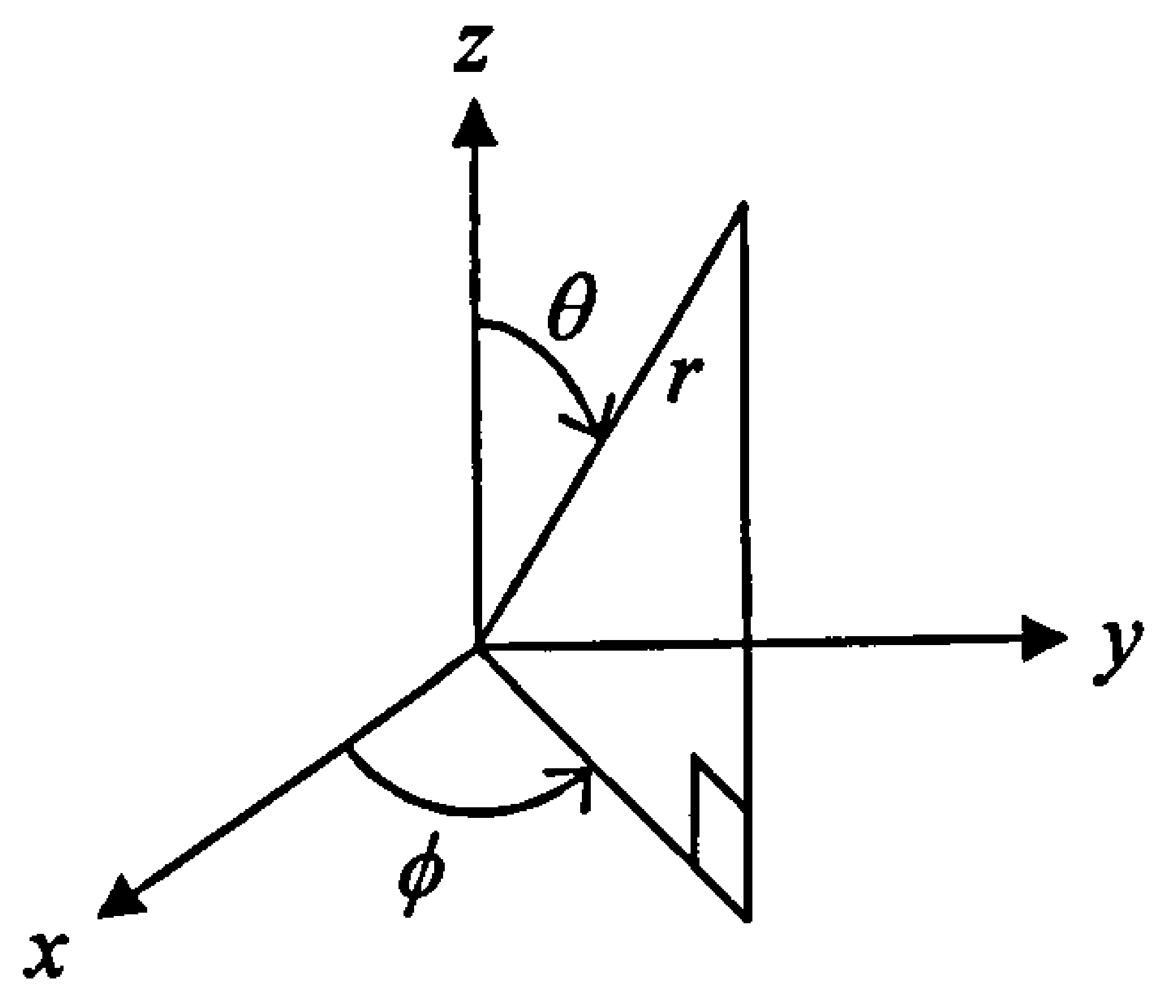

A.2 Constant Vertical Separation (CVS)

The geometry is defined using spherical coordinates as:-

$$-\pi N \le \phi \le \pi N$$

$$\theta = \cos^{-1}\left(\frac{\phi}{\pi N}\right)$$

$$r = a$$

where:-

N is the number of turns

a is the radius of the sphere

Conversion to Cartesian coordinates can be achieved using:-

$$x = r\sin(\theta)\cos(\phi)$$

$$y = r\sin(\theta)\sin(\phi)$$

$$z = r\cos(\theta)$$

thus:-

$$x = a\sin\left(\cos^{-1}\left(\frac{\phi}{\pi N}\right)\right)\cos(\phi)$$

$$y = a\sin\left(\cos^{-1}\left(\frac{\phi}{\pi N}\right)\right)\sin(\phi)$$

$$z = a\left(\frac{\phi}{\pi N}\right)$$

Introducing the substitution $\psi = \left(\frac{\phi}{\pi N}\right)$ and simplifying leaves:-

$$x = a\sqrt{1-\psi^2}\cos(\phi)$$

$$y = a\sqrt{1-\psi^2}\sin(\phi)$$

$$z = a\psi$$

The tangent vector $\hat{\ell}$ can be obtained from:-

$$\hat{\ell} = \left(\hat{\ell}_x, \hat{\ell}_y, \hat{\ell}_z\right) = \frac{\left(\dfrac{dx}{d\phi}, \dfrac{dy}{d\phi}, \dfrac{dz}{d\phi}\right)}{\left|\dfrac{d\rho}{d\phi}\right|}$$

where ρ is the position vector given by $\rho = (x, y, z)$

thus:-

$$\left|\frac{\mathrm{d}\rho}{\mathrm{d}\phi}\right| = \sqrt{\left(\frac{\mathrm{dx}}{\mathrm{d}\phi}\right)^2 + \left(\frac{\mathrm{dy}}{\mathrm{d}\phi}\right)^2 + \left(\frac{\mathrm{dz}}{\mathrm{d}\phi}\right)^2}$$

which gives:-

$$\left|\frac{\mathrm{d}\rho}{\mathrm{d}\phi}\right| = \mathrm{a}\sqrt{\left(1-\psi^2\right) + \frac{1}{(\pi\mathrm{N})^2\left(1-\psi^2\right)}}$$

and:-

$$l_x = -\left[\frac{\left[\pi N\left(1-\psi^2\right)\sin\phi + \psi\cos\phi\right]}{\sqrt{(\pi N)^2\left(1-\psi^2\right)^2 + 1}}\right]$$

$$l_y = \left[\frac{\left[\pi N\left(1-\psi^2\right)\cos\phi - \psi\sin\phi\right]}{\sqrt{(\pi N)^2\left(1-\psi^2\right)^2 + 1}}\right]$$

$$l_z = \left[\frac{\sqrt{1-\psi^2}}{\sqrt{(\pi N)^2\left(1-\psi^2\right)^2 + 1}}\right]$$

The curved length of a section of the antenna can be obtained by integrating $\left|\frac{d\rho}{d\phi}\right|$.

Thus the total curved length of an SHA with CVS spacing between turns is:-

$$\text{Curved length} = a\int_{-\pi N}^{\pi N}\sqrt{\left(1-\psi^2\right)+\frac{1}{(\pi N)^2\left(1-\psi^2\right)}}\,d\phi$$

The vector dot-product between the tangents at any two points ϕ and ϕ' (with associated ψ and ψ') is given by:-

$$\left(\hat{\ell}\cdot\hat{\ell}'\right)=\frac{\begin{pmatrix}\left[(\pi N)^2\left(1-\psi^2\right)\left(1-\psi'^2\right)+\psi\psi'\right]\cos(\phi-\phi')\\ +\pi N\left[\left(1-\psi^2\right)\psi'-\left(1-\psi'^2\right)\psi\right]\sin(\phi-\phi')\\ +\sqrt{1-\psi^2}\sqrt{1-\psi'^2}\end{pmatrix}}{\sqrt{1+(\pi N)^2\left(1-\psi^2\right)^2}\sqrt{1+(\pi N)^2\left(1-\psi'^2\right)^2}}$$

and the straight-line separation distance between them is:-

$$R=a\sqrt{2-2\psi\psi'-2\sqrt{1-\psi^2}\sqrt{1-\psi'^2}\cos(\phi-\phi')}$$

If a ground plane is present a distance h below the bottom of the sphere, a reflected source point appears. The equations associated with this reflection are:-

$$\left(\hat{\ell}\cdot\hat{\ell}'\right)=\frac{\begin{pmatrix}-\left[(\pi N)^2\left(1-\psi^2\right)\left(1-\psi'^2\right)+\psi\psi'\right]\cos(\phi-\phi')\\ -\pi N\left[\left(1-\psi^2\right)\psi'-\left(1-\psi'^2\right)\psi\right]\sin(\phi-\phi')\\ +\sqrt{1-\psi^2}\,\sqrt{1-\psi'^2}\end{pmatrix}}{\sqrt{1+(\pi N)^2\left(1-\psi^2\right)^2}\,\sqrt{1+(\pi N)^2\left(1-\psi'^2\right)^2}}$$

and:-

$$\mathrm{R}=\mathrm{a}\sqrt{\begin{matrix}2+2\psi\psi'+4\mathrm{h}^2-4\mathrm{h}\psi-4\mathrm{h}\psi'\\ -2\sqrt{1-\psi^2}\,\sqrt{1-\psi'^2}\cos(\phi-\phi')\end{matrix}}$$

A.3 Constant Circumferential Separation (CCS)

The geometry is defined using spherical coordinates as:-

$$-\pi N \le \phi \le \pi N$$

$$\theta = \frac{\pi}{2} - \frac{\phi}{2N}$$

$$r = a$$

Introducing the substitution $\psi = \frac{\pi}{2} - \frac{\phi}{2N}$ and converting to Cartesian coordinates gives:-

$$x = a\sin(\psi)\cos(\phi)$$

$$y = a\sin(\psi)\sin(\phi)$$

$$z = -a\cos(\psi)$$

Differentiating the position vector with respect to ϕ gives:-

$$\left|\frac{\mathrm{d}\rho}{\mathrm{d}\phi}\right| = \sqrt{\left(\frac{\mathrm{dx}}{\mathrm{d}\phi}\right)^2 + \left(\frac{\mathrm{dy}}{\mathrm{d}\phi}\right)^2 + \left(\frac{\mathrm{dz}}{\mathrm{d}\phi}\right)^2}$$

where

$$\frac{dx}{d\phi} = a\left[\frac{1}{2N}\left(\cos(\psi)\cos(\phi)\right) - \sin(\psi)\sin(\phi)\right]$$

$$\frac{dy}{d\phi} = a\left[\frac{1}{2N}\left(\cos(\psi)\sin(\phi)\right) + \sin(\psi)\cos(\phi)\right]$$

$$\frac{dz}{d\phi} = a\left[\frac{1}{2N}\left(\sin(\psi)\right)\right]$$

Thus:-

$$\left|\frac{\mathrm{d}\rho}{\mathrm{d}\phi}\right| = \mathrm{a}\sqrt{\frac{1}{4\mathrm{N}^2} + \sin^2(\psi)}$$

And:-

$$\ell_x = \frac{\dfrac{dx}{d\phi}}{\left|\dfrac{d\rho}{d\phi}\right|},\ \ell_y = \frac{\dfrac{dy}{d\phi}}{\left|\dfrac{d\rho}{d\phi}\right|},\ \ell_z = \frac{\dfrac{dz}{d\phi}}{\left|\dfrac{d\rho}{d\phi}\right|}$$

$$\ell_x = \frac{\left(\cos(\psi)\cos(\phi)\right) - 2N\left(\sin(\psi)\sin(\phi)\right)}{\sqrt{1 + 4N^2\sin^2(\psi)}}$$

$$\ell_y = \frac{\left(\cos(\psi)\sin(\phi)\right) + 2N\left(\sin(\psi)\cos(\phi)\right)}{\sqrt{1 + 4N^2\sin^2(\psi)}}$$

$$\ell_z = \frac{\sin(\psi)}{\sqrt{1 + 4N^2\sin^2(\psi)}}$$

The total curved length is:-

$$= a\int_{-\pi N}^{\pi N} \sqrt{\frac{1}{4N^2} + \sin^2(\psi)}$$

The vector dot-product between the tangents at any two points ϕ and ϕ' (with associated ψ and ψ') is given by:-

$$\left(\hat{\ell}\cdot\hat{\ell}'\right)=\frac{\begin{array}{l}\left[\left(\cos(\psi)\cos(\phi)\right)-2N\left(\sin(\psi)\sin(\phi)\right)\right]\\ \times\left[\left(\cos(\psi')\cos(\phi')\right)-2N\left(\sin(\psi')\sin(\phi')\right)\right]\\ +\left[\left(\cos(\psi)\sin(\phi)\right)+2N\left(\sin(\psi)\cos(\phi)\right)\right]\\ \times\left[\left(\cos(\psi')\sin(\phi')\right)+2N\left(\sin(\psi')\cos(\phi')\right)\right]\\ +\sin(\psi)\times\sin(\psi')\end{array}}{\sqrt{1+4N^2\sin^2(\psi)}\sqrt{1+4N^2\sin^2(\psi')}}$$

and the straight-line separation distance between them is:-

$$R=a\sqrt{\begin{array}{l}\left(\sin(\psi)\cos(\phi)-\sin(\psi')\cos(\phi')\right)^2\\ +\left(\sin(\psi)\sin(\phi)-\sin(\psi')\sin(\phi')\right)^2\\ +\left(\cos(\psi)-\cos(\psi')\right)^2\end{array}}$$

Appendix B

Expressions for far-field patterns

B.1 Introduction

This appendix gives the equations for the calculation of the far field radiation pattern and axial ratio, as used in the SHA-MoM code.

The coordinate system used throughout this thesis is as shown below:-

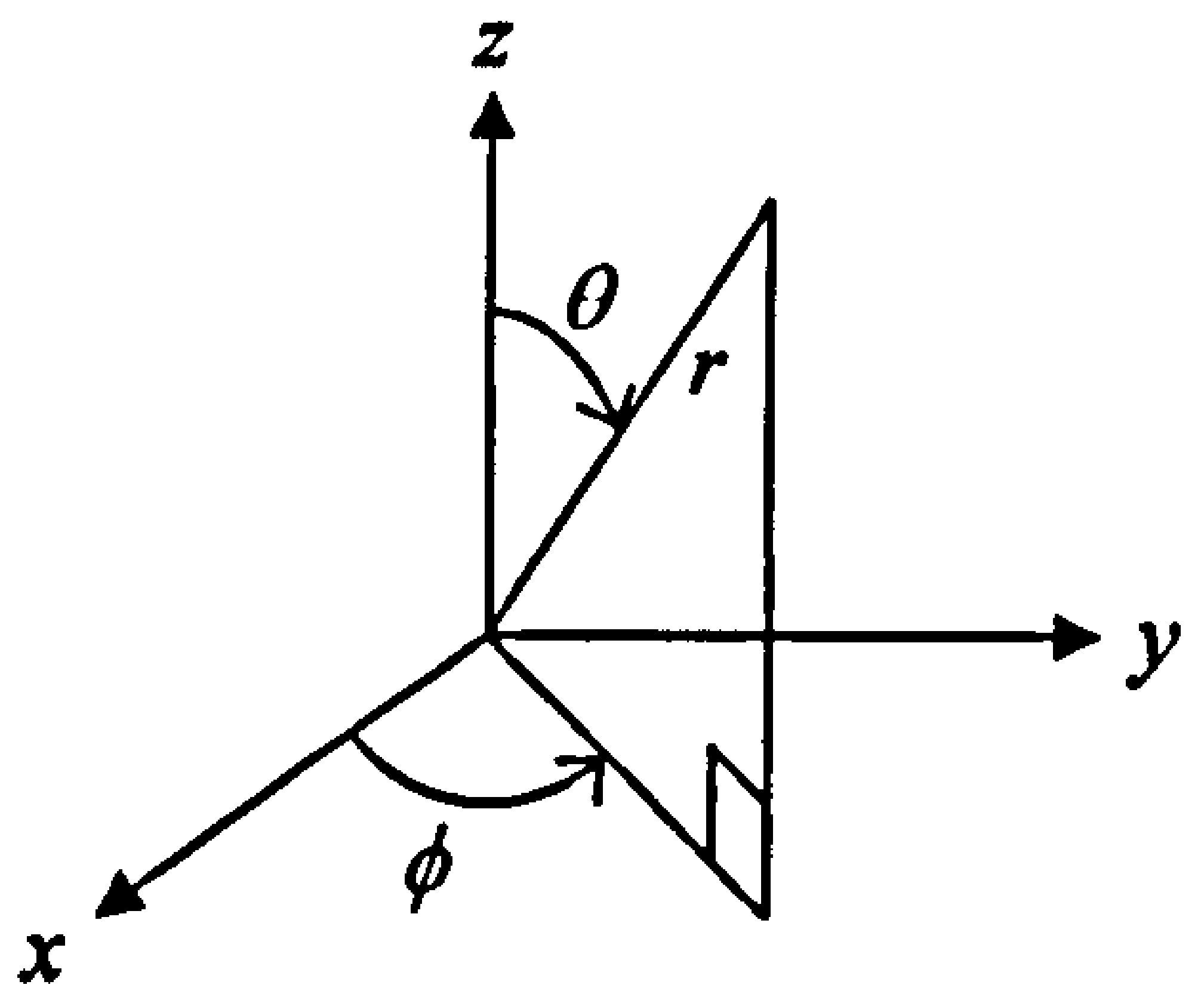

B.2 Far Field

Using the spherical coordinates (r,θ,ϕ) where r is the distance from the origin, ϕ is the azimuthal angle in the xy-plane, and θ is the polar angle, the equation relating $\mathbf{E}^S$ to $\mathbf{A}$ is:-

$$\mathbf{E}^S = \frac{1}{j\omega\varepsilon_0}\left[\beta^2 \mathrm{A} + \nabla(\nabla \cdot \mathrm{A})\right]$$

In the far-field, this can be approximated to [1]:-

$$E^{s}{}_{\theta} = \frac{1}{j\omega\varepsilon_0}\left[\beta^2 A_\theta\right]$$

$$E^{s}{}_{\phi} = \frac{1}{j\omega\varepsilon_0}\left[\beta^2 A_\phi\right]$$

$$E^{s}{}_{r} = 0$$

The following equation must be computed for both $\hat{\ell} = \hat{\theta}$ and $\hat{\ell} = \hat{\phi}$

$$\hat{\ell}\cdot E^{s} = \frac{1}{j\omega\varepsilon_0}\left[\beta^2 \int_{\ell'} I(\ell')\left(\hat{\ell}\cdot\hat{\ell}'\right)G(R)d\ell'\right]$$

where...

$$\hat{\ell} = \hat{\theta} = \begin{bmatrix}\cos\phi\cos\theta \\ \sin\phi\cos\theta \\ -\sin\theta\end{bmatrix} \text{ or } \hat{\ell} = \hat{\phi} = \begin{bmatrix}-\sin\phi \\ \cos\phi \\ 0\end{bmatrix}$$

and...

$$R = \left|\mathbf{r} - \mathbf{r}'\right| \text{ where } \mathbf{r} = (r\sin\theta\cos\phi)\hat{x} + (r\sin\theta\sin\phi)\hat{y} + (r\cos\theta)\hat{z}$$

$I(\ell')$ can be decomposed and the current matrix value taken out of the integral (if the E-field from all pulses are summed separately.)

The result will be a product of 1/r. Therefore multiplying by r (in cm) will normalise it.

B.3 Gain

Power radiated will be:-

$$P_r = \frac{1}{2}|I|^2 R_r$$

where P_r is an rms value (in W), and I is a peak value (in A)

Power (dBi)...

$$= 10\log_{10}\left(\frac{r^2}{2\eta}\left[|E_\theta|^2 + |E_\phi|^2\right] \times \frac{4\pi}{P_r}\right) \text{ where } \eta = \sqrt{\frac{\mu_0}{\varepsilon_0}}$$

B.4 Axial ratio

Axial ratio is defined as the ratio of the maximum to minimum magnitudes of E-field as it rotates with time. Expressions for calculating axial ratio are [2]:-

$$\text{Axial Ratio} = \pm\frac{\text{major axis}}{\text{minor axis}}$$

where:-

$$\text{major axis} = \sqrt{\frac{|E_\theta|^2 + |E_\phi|^2 + \sqrt{|E_\theta|^4 + |E_\phi|^4 + 2|E_\theta|^2|E_\phi|^2\cos(2\Delta\psi)}}{2}}$$

$$\text{minor axis} = \sqrt{\frac{|E_\theta|^2 + |E_\phi|^2 - \sqrt{|E_\theta|^4 + |E_\phi|^4 + 2|E_\theta|^2|E_\phi|^2\cos(2\Delta\psi)}}{2}}$$

and:-

$$|E_\theta| = \sqrt{(E_{\theta,\mathrm{real}})^2 + (E_{\theta,\mathrm{imag}})^2}$$

$$|E_\phi| = \sqrt{(E_{\phi,\mathrm{real}})^2 + (E_{\phi,\mathrm{imag}})^2}$$

$$\psi_\phi = \tan^{-1}\left(\frac{E_{\phi,\mathrm{imag}}}{E_{\phi,\mathrm{real}}}\right)$$

$$\Delta\psi = \psi_\theta - \psi_\phi$$

The sign of AR (if given) is determined by the sense of the circular polarisation where:-

+ve values indicate counter-clockwise or left-hand CP, and

-ve values indicate clockwise or right-hand CP, and

Thus:-

$1 \le |\mathrm{AR}| \le \infty$

$|\mathrm{AR}| = 1$ indicates circular polarisation

$|\mathrm{AR}| = \infty$ indicates linear polarisation

Any other value indicated elliptical polarisation

Expressed in dB, the axial ratio is defined as:-

$$AR_{dB} = 20\log_{10} AR$$

References

1 C. A. Balanis, "Antenna Theory : Analysis and Design", New York : Wiley, 2nd Ed., 1997.

2 C. A. Balanis, "Advanced Engineering Electromagnetics", New York : Wiley, 1989.

Appendix C

The NSGA-II genetic algorithm

C.1 Introduction

NSGA-II is an elitist non-dominated sorting genetic algorithm proposed by Deb [1]. This appendix provides a brief description of its operation.

C.2 Non-dominated fronts

A non-dominated member of the population is one for which there are no other members which perform better against each of the optimisation objectives simultaneously. The first non-dominated front in a population is the subset of the population which are non-dominated. If these members are then temporarily discarded, the second non-dominated front is the subset of the remaining population which are now non-dominated. The process of removing the current non-dominated front and finding the next continues until all members of the population have been assigned a non-dominated front number.

C.3 Crowding distance

To help select between different members of the same non-dominated front, a crowding distance metric is defined. This is a measure of how close the member is to other members with similar fitness. When members are removed from the population, and the choice of which member(s) to remove cannot be made based on the non-dominate front number, the crowding distance metric is used such that members which are similar to others are more likely to be removed.

C.4 Operation of NSGA-II

The initial population of N members is generated at random. Values for each of the genes are chosen at random keeping to the ranges specified. The fitness of each of these members is then evaluated. This is done by running the SHA-MoM code.

The next steps are iterative and will be repeated until the GA is stopped or a given number of generations have been computed.

Firstly, some members are copied to the mating pool. The choice of which members to copy is based on their non-dominated front number, and to a lesser extent their crowding distance metric. The exact method is described in section C.4.1.

Members in the mating pool are now paired, and each pair produces two new offspring using the arithmetic crossover operator. The offspring are created such that they inherit similar genes to their parents. Mutation is also applied to a percentage of genes. When a gene is mutated it is given a random value. Mutation helps to prevent stagnation, and helps to search an entire parameter space.

In total, N new offspring are created and these are then evaluated for fitness. Once this is done the parent and offspring population are merged forming a population of 2N.

This merged population is ranked according to non-dominated front number and within the front by the crowding distance metric. The bottom N members are then discarded and the process repeats.

C.4.1 Filling the mating pool

First the mating pool is filled with N members by holding N tournaments between pairs of solutions with the winning solution being placed into the mating pool. Pairs are chosen in such a way that each member of the population is entered into exactly two tournaments. The tournament is decided based primarily on the front number of each of the solutions, with the solution with the better front number going into the mating pool. If the two solutions are in the same non-dominated front, then the tournament is decided based on the crowding distance of each of the solutions.

At this point, the mating pool will consists of N members. The better members of the old population may appear twice (having won both the tournaments they played) and poorer members may not make it into the mating pool at all.

References

1 K. Deb, S. Agrawal, A. Pratap, and T. Meyarivan, “A Fast Elitist Non-dominated Sorting Genetic Algorithm for Multi-objective Optimization: NSGA-II”, Proceedings of the 6th International Conference on Parallel Problem Solving from Nature (PPSN VI), pp. 849-858, Sep. 2000.